Åbo Akademi University

Johanna Grönqvist

Strong Coulomb Coupling in Graphene

Microscopic theory of a many-body ground state and its excitations

Åbo Akademi University Press
Tavastgatan 13, FI-20500 Åbo, Finland
Tel. +358 (02) 215 3478
E-mail: forlaget@abo.fi

Sales and distribution:
Åbo Akademi University Library
Domkyrkogatan 2–4, FI-20500 Åbo, Finland
Tel. +358 (0)2 215 4190
E-mail: publikationer@abo.fi

Strong Coulomb Coupling in Graphene

Microscopic theory of
a many-body ground state
and its excitations

Johanna Grönqvist

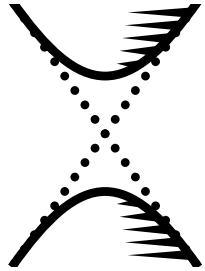

Physics
Faculty of Science and Engineering
Åbo Akademi University
Åbo 2018

Supervisor

Professor Markus Lindberg
Åbo Akademi University

Pre-examiners

Professor Ermin Malic
Chalmers University of Technology

Professor Jukka Tulkki
Aalto University

Opponent for the public defense

Professor Mikael Fogelström
Chalmers University of Technology

Painosalama – Åbo, Finland 2018

Acknowledgments

This work has been done in collaboration with the Physics departments at Åbo Akademi University, Technische Universität Berlin and Philipps-Universität Marburg. I am very grateful for the opportunity to spend time in these groups and for the opportunity to participate in this exciting new field.

To all my friends, colleagues and advisors, in Germany, Finland and the Netherlands, thank you for sharing your knowledge and for all the help and feedback you've given me at different stages of the work. I've enjoyed our many dicussions and discoveries of the aspects and phenomena of this fascinating material. Thanks also to everyone who helped me with the text and provided support and encouragement along the way. Your interest in the science and sometimes also your lack of specific technical knowledge has been especially helpful, as it has given me motivation to communicate more broadly and attempt to write an accessible description of our work.

— at Technische Universität Berlin, Matthias Hirtschulz, Frank Milde, Ermin Malic and Andreas Knorr; at Philipps-Universität Marburg, Johannes Steiner, Johannes Schurer, Gunnar Berghäuser, Stephan W. Koch and Tineke Stroucken; at Åbo Akademi University, Markus Lindberg, Fredrik Jansson and Joakim Slotte; and Andrea Klettke, Eva Deutekom, Victor Boteanu, Amir Masoud Abdol and Veronika Jansson.

Contents

List of included publications

This thesis is based on the following six publications. The publications are reprinted here with permission from the publishers.

PAPER I. **Spatiotemporal dynamics of optically generated electron–hole excitations in single-walled carbon nanotubes** *117*

J. H. Grönqvist, M. Hirtschulz, A. Knorr, and M. Lindberg
Phys. Rev. B **81**, 035414 (2010)

The author developed the analytical model by deriving equations, developed the software for the numerical studies, ran the simulations and created the figures, and wrote the text together with the co-authors.

PAPER II. **Wannier excitons signalling strong Coulomb coupling in graphene** *125*

J. H. Grönqvist, T. Stroucken, M. Lindberg, and S. W. Koch
Eur. Phys. J. B **85**, 395 (2012)

The author ran the simulations, analysed the data and created the figures, and wrote the text together with the co-authors.

PAPER III. **Optical response and ground state of graphene** *133*

T. Stroucken, J. H. Grönqvist, and S. W. Koch
Phys. Rev. B **84**, 205445 (2011)

PAPER IV. **Excitonic resonances as fingerprint of strong Coulomb coupling in graphene** *149*

T. Stroucken, J. H. Grönqvist, and S. W. Koch
J. Opt. Soc. Am. B **29**, A86 (2012)

For Papers III–VI, the author participated in deriving the analytical framework, developed and tested the software, ran the simulations and analysed the data, created the figures, as well as participated in writing the text together with the co-authors.

Introduction

Graphene is a single layer of graphite, one atom thick. This sheet of carbon atoms is completely flat, i.e. it is two-dimensional. Graphene was the first of these two-dimensional crystals to be isolated and characterized, in a famous study in 2004 [1, 2] leading to a Nobel prize in Physics in 2010. Graphene has many properties that make it interesting for technological applications, such as being extraordinarily strong and flexible, and having a high conductivity.

Since the discovery of graphene, many other two-dimensional crystals have been manufactured and studied [3]. This new group of materials is interesting due to a range of intrinsic characteristics, different from those of ordinary three-dimensional materials. Also, the two-dimensional crystals themselves are often very pure and well-defined; having only two dimensions leaves less space for crystal defects and impurities which are the main source of losses in three-dimensional crystals.

For applications, graphene and other two-dimensional crystals can be used as building blocks, by stacking sheets with different properties, adding up to any kind of features one wishes to have. In this way, building with two-dimensional materials offers precise, near atomic level control of the structure. Using two-dimensional crystals in applications also provides the possibility to control the environment of essentially every atom in the material. This can be achieved by placing the crystal sheet e.g. next to another material or in an electric field. By contrast, working with standard three-dimensional materials, the different environments for atoms at the surface and in the bulk of the material have to be taken into account.

For using graphene in electronic applications, a solid understanding of the electrons of graphene is crucial. From a theoretical point of view, the behavior of electrons in graphene is also interesting in itself. The electrons being confined to move in a two-dimensional plane makes the system fundamentally different from electron behavior in three-dimensional materials. The confinement to the plane causes strong interactions between the electrons, and a provides the possibility

to study a range of effects commonly unavailable. The system having only two degrees of freedom instead of three also makes larger systems more feasible for numerical simulations.

In this thesis, the electrons in graphene are studied using theoretical and numerical methods. The studies are done mainly through investigations related to the so-called band structure of the material; meaning, how the energy of an electron in the material depends on its momentum.

Typically, an electron in free space or in a semiconductor has an energy proportional to the square of its momentum. This is how a particle behaves when it has a mass. For graphene, it has been shown that the energy is a linear function of the momentum — this is a consequence of the hexagonal structure of the lattice. A linear energy is also characteristic of a massless particle moving at the speed of light. In effect, in graphene we have electrons moving as if they have no mass — a fascinating concept for physicists. Because of this linear energy relation, the electrons absorb light evenly at a whole range of frequencies; it is as easy to add energy to the electron at low momentum as at high momentum. The "masslessness" of the electrons in the material is also why graphene conducts electricity so well.

The usefulness of semiconductors in technology, for example as transistors, is based on the gap in energy between the valence band and the conduction band. This band gap is the minimum energy needed to make a dormant electron free to conduct electricity, and this effect is the functionality of a transistor, a laser, a solar cell, and any other technology based on semiconducting materials. The linear energy in graphene, while good for the conductivity, also comes with a problem — there is no gap between the bands. This makes graphene less than ideal as a replacement for silicon as the standard material for electronic technology.

In this thesis and the papers it is based on, we investigate the possibility of interactions between the electrons themselves, under given circumstances, causing a gap to open in the band structure of graphene. I discuss the work done to apply an electronic many-body approach to graphene. The techniques presented here are based on time dynamics of quantum mechanical expectation values, defining the system of interacting electrons in the graphene sheet.

This approach is well known from the theory of electrons in three-dimensional crystalline semiconductors, and has successfully been applied to numerous calculations of transport and optical properties of such systems [4]. In the studies presented in this work, we modify the methods to account for the two-dimensional nature and the massless electrons of graphene.

Typical band structure calculations neglect the interaction between electrons, accounting only for how a single electron interacts with the lattice of ions that make up the static part of the material. The assumption is that the band structure of the material is not influenced by interaction among the electrons. In theoretical calculations, it is possible to break this assumption, by artificially cranking up the strength of the interaction between the electrons.

Once the electron–electron interaction is made strong enough, there will be a spontaneous symmetry breaking in the electronic system. This comes with corresponding distortion of the band structure, similar to the formation of Cooper pairs in a superconductor. The transition happens when the binding energy of an electron–hole pair exceeds the band gap [5]. For an insulator or a semiconductor, it would require an unrealistically large Coulomb interaction for this to happen. For an ungapped system such as graphene, however, the possibility of a strong enough coupling is a relevant issue.

Before going into the issues related to the strong Coulomb coupling regime in graphene, I present the standard building blocks for creating an electronic many-body model in chapter 1. In chapters 2 and 3, the building blocks are used to construct a model many-body Hamiltonian for electrons in graphene, interacting with each other and with external light fields.

In chapters 4 and 5, the many-body model is used for constructing equations describing the dynamics of the electronic system. In chapter 5 and Paper I, the equations are used for studying the dynamics of electrons and their interaction with light in a semiconducting graphene-like system; a carbon nanotube. In this system, a band gap is created by the geometrical restriction imposed on the graphene lattice by rolling it into a tube.

In chapter 6 and Paper II we investigate the possibility for a strong-coupling regime, where the interaction between electrons is strong enough to alter the ground state. Parts of the many-body theory are used to study an electron–hole pair in graphene, and its binding energy. Since the bands have no energy gap, any pair with a nonzero binding energy is a mark of the onset of the strong-coupling phase. What is needed to treat the electron dynamics in the strong-coupling phase correctly are the techniques discussed in chapter 7 and Paper III, where the many-body theory is used to set up equations for the true strong-coupling ground state. Once the many-body ground state is known, the theory is used in a more traditional way in chapter 8 and Paper IV; for studying the simplest excitations of the gapped strong-coupling ground state.

In chapter 9 and Paper V essentially the same steps are shown, shortly, for bilayer graphene; setting up the many-body model in terms of band structure

and electron–electron interaction, as well as equations governing the strong-coupling regime. Finally, in chapter 10 and Paper V, we present how to self-consistently solve the interconnected effects of electronic screening and strong-coupling ground state. We use a treatment of the electron–electron interaction which self-limits the strength of the interaction and its influence on the band structure reconfiguration, and apply this technique to single layer and bilayer graphene.

Chapter 1

Background — carbon atoms in a plane

Our goal is to establish equations that describe the system of electrons in graphene and how it develops over time. In crystalline solids, the active electrons are delocalized over the atomic lattice and the electronic state is constructed by means of a wavefunction. This wavefunction contains contributions from electrons at each atomic lattice site; adding up these single-electron pieces gives us our many-body model.

The time development of the electronic state, and hence the system, is governed by an operator called the Hamiltonian. The Hamiltonian measures the system energy, essentially by counting how many electrons are in each possible state and how much each state contributes to the total energy.

How the electrons sit around their ions is described by a well-known theory, the so-called tight-binding approach. The tight-binding description is a single-particle theory, and provides a single-particle basis in which to express the many-body wavefunction. Using the tight-binding wavefunctions, one can derive an expression for the single-particle energy, as well as a Hamiltonian for the electronic system.

The basic theory of electrons in a graphite sheet was introduced by P. R. Wallace in 1947 [6] where he set up the tight-binding approach to graphene. Wallace calculated the basic consequences of the hexagonal geometry of the graphene lattice shown in figure 1.1, such as the appearance of a cone-like part of the energy structure. An overview of this general derivation is given, for example, in [7].

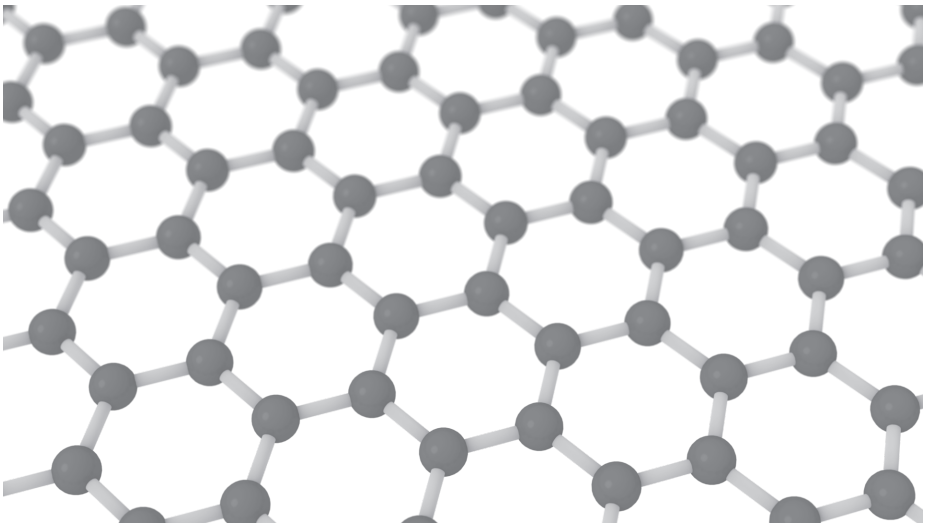

Figure 1.1 Carbon atoms in a hexagonal lattice.

1.1 The carbon atom in a lattice

The graphene sheet consists of carbon atoms, arranged in a two-dimensional hexagonal lattice. The hexagonal structure is a consequence of the electron orbitals in carbon.

A carbon atom has six electrons; the inner two form a filled shell and the outer four form a half-filled shell. In diamond (three-dimensional crystalline carbon) the outer electrons of each carbon atom form four identical bonds with the four neighboring carbon atoms, in a tetrahedral shape. In graphene (a two-dimensional carbon sheet) three of the four outer electrons form single bonds (strong and inactive) with the neighbors. The characteristic hexagons of the graphene lattice are formed by each atom having three neighbors, shown in figure 1.1.

The fourth outer electron is in a p_z orbital, out of the graphene plane. The electrons in the p_z orbitals are the ones responsible for the electrical and optical properties of graphite and graphene. Such an orbital can be written as

$$\phi(\boldsymbol{x}) = \frac{1}{\sqrt{2\pi d^3}} \frac{|\boldsymbol{x}|}{4d} e^{-|\boldsymbol{x}|/2d} \cos\varphi \tag{1.1}$$

with a length parameter d, which determines the spatial extension of the orbital. The $\cos\varphi$ part gives the orbital its shape and orientation, as shown in figure 1.2.

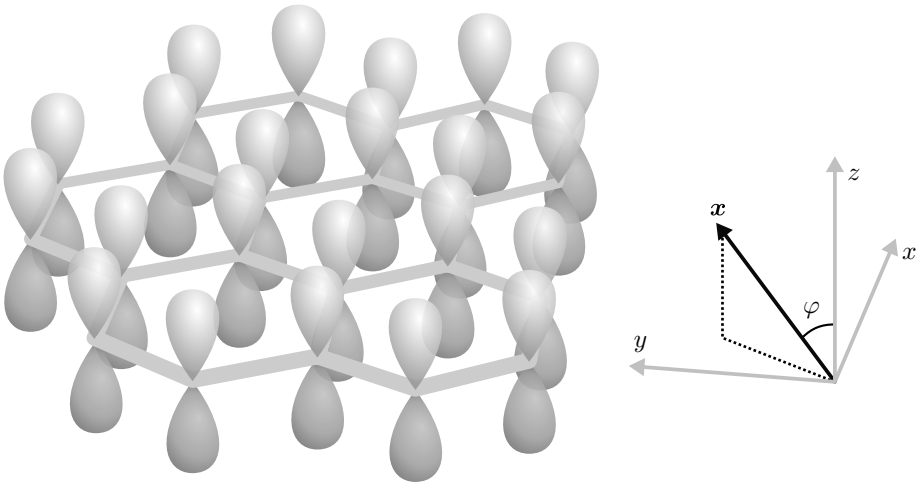

Figure 1.2 The graphene lattice with p_z orbitals (1.1) out of the plane at the atomic sites.

Comparing (1.1) with the same orbital in hydrogen, the parameter d takes the place of the Bohr radius divided by an effective charge.

The fact that the outer shell of the carbon atom is half-filled makes carbon a candidate for a semiconductor, since the Fermi level is right between the valence and the conduction band. Carbon is electronically similar to silicon, which is a semiconductor, and it is known that diamond also is a semiconductor. For graphene this is a different matter. It is generally held that graphene is a so-called semimetal, that is to say, the valence and conduction bands touch at a single point at the Fermi level, so that there is no band gap.

1.2 Geometry of the graphene lattice

To formulate a solid state theory for graphene, the first thing to note is that the hexagonal lattice contains two groups of carbon atoms (labeled A and B in figure 1.3) which each have different surroundings — there is an empty space to the right of the A atoms, and to the left of the B atoms. Consequently, the unit cell needs to contain two atoms, one each from the A and B sublattices. The unit cell can be chosen, for example, as a hexagon or a rhombus, as shown with dotted lines in figure 1.3. In this way, the hexagonal lattice is said to consist of an A and a B sublattice. These sublattices are in themselves complete Bravais lattices, which is the essential property for forming the reciprocal (i.e. momentum) space, in which all crystalline solid state calculations are performed.

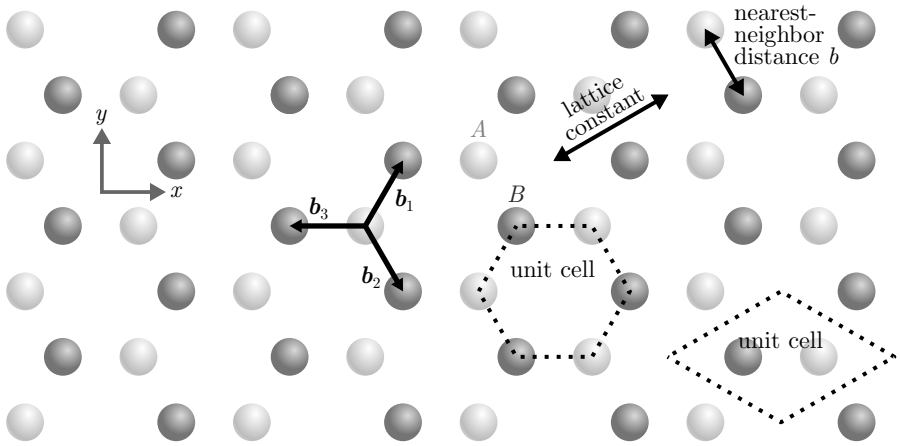

Figure 1.3 The carbon atoms in a sheet of graphene, forming hexagons. The carbon atoms in sublattice A are shown as lighter spheres, and the sublattice B as darker spheres.

Much of the gist of the calculations in the following are based on the division into an A and a B sublattice. I frequently refer to the vectors from an atom in sublattice A to its three nearest neighbors, which are in sublattice B.

$$\begin{aligned}
\boldsymbol{b}_1 &= b\big(\cos\frac{\pi}{3}\,\hat{\boldsymbol{e}}_x + \sin\frac{\pi}{3}\,\hat{\boldsymbol{e}}_y\big) = \frac{b}{2}\hat{\boldsymbol{e}}_x + \frac{\sqrt{3}b}{2}\hat{\boldsymbol{e}}_y \\
\boldsymbol{b}_2 &= b\big(\cos\frac{\pi}{3}\,\hat{\boldsymbol{e}}_x - \sin\frac{\pi}{3}\,\hat{\boldsymbol{e}}_y\big) = \frac{b}{2}\hat{\boldsymbol{e}}_x - \frac{\sqrt{3}b}{2}\hat{\boldsymbol{e}}_y \\
\boldsymbol{b}_3 &= -b\hat{\boldsymbol{e}}_x\,.
\end{aligned} \tag{1.2}$$

These are chosen as in [8]. The positions of the atoms are denoted by $\boldsymbol{R}^A$ and $\boldsymbol{R}^B$, and the positions of the B atoms around an A atom are given by $\boldsymbol{R}^B = \boldsymbol{R}^A + \boldsymbol{b}_i$ for $i = 1, 2, 3$.

1.3 The tight-binding approach to graphene

The tight-binding approach assumes that the relevant outer electrons are confined to the local potentials at each atomic site. Whether this is a valid assumption for a given material can be tested e.g. by density-functional calculations, which for the case of graphene give reasonable agreement. Using a tight-binding ansatz gives a simple analytical expression for the single-particle energy (i.e., the band structure) which still displays interesting physics.

When calculating the band structure in this manner, one leaves out the interaction between electrons. This is a valid approximation only when the Coulomb interaction is weak enough, in what we will refer to as the weak-coupling regime.

To calculate the system Hamiltonian, we need an expression for the so-called field operators. The field operator is here expanded in a momentum space basis,

$$\hat{\psi}(\boldsymbol{x}) = \sum_{\lambda \boldsymbol{k}} \Psi_{\lambda \boldsymbol{k}}(\boldsymbol{x})\, \hat{a}_{\lambda \boldsymbol{k}}$$

where the sum λ is over the conduction and valence bands, and the sum $\boldsymbol{k}$ is over momenta in the first Brillouin zone. The operator $\hat{a}_{\lambda \boldsymbol{k}}$ annihilates an electron in band λ with momentum $\hbar \boldsymbol{k}$.

When using a tight-binding ansatz, the unit-cell periodic parts of the wavefunction $\Psi_{\lambda \boldsymbol{k}}(\boldsymbol{x})$ are taken as the orbitals of the outer electrons, in this case the p_z orbitals $\phi(\boldsymbol{x})$ (1.1). Furthermore, to account for the two non-equivalent atomic sites in the unit cell, the wavefunction is set up as a linear combination of Bloch functions for each of the two sublattices. On sublattice A the wavefunction is

$$\frac{1}{\sqrt{N}} \sum_{\boldsymbol{R}^A} e^{i \boldsymbol{k} \boldsymbol{R}^A} \phi(\boldsymbol{x} - \boldsymbol{R}^A)$$

where N is the number of unit cells, and similarly for the B sublattice. The total wavefunction takes the form

$$\Psi_{\lambda \boldsymbol{k}}(\boldsymbol{x}) = \frac{C^A_{\lambda \boldsymbol{k}}}{\sqrt{N}} \sum_{\boldsymbol{R}^A} e^{i \boldsymbol{k} \boldsymbol{R}^A} \phi(\boldsymbol{x} - \boldsymbol{R}^A) \; + \; \frac{C^B_{\lambda \boldsymbol{k}}}{\sqrt{N}} \sum_{\boldsymbol{R}^B} e^{i \boldsymbol{k} \boldsymbol{R}^B} \phi(\boldsymbol{x} - \boldsymbol{R}^B) \tag{1.3}$$

where the functions $C^{A,B}_{\lambda \boldsymbol{k}}$ are the coefficients for the linear combination, which are to be determined in the following.

Demanding that the wavefunction $\Psi_{\lambda \boldsymbol{k}}(\boldsymbol{x})$ is an eigenfunction of the single-particle Hamiltonian (consisting of the kinetic energy of the electrons and the potential energy of the electrons in the periodic lattice of ions) gives expressions for the coefficients $C^{A,B}_{\lambda \boldsymbol{k}}$. This condition, which is a Schrödinger equation

$$\Big[\frac{-i\hbar^2 \nabla^2}{2m} + \sum_{\boldsymbol{R}} V_{\mathrm{ion}}(\boldsymbol{x} - \boldsymbol{R}) \Big] \Psi_{\lambda \boldsymbol{k}}(\boldsymbol{x}) = E_{\lambda \boldsymbol{k}} \Psi_{\lambda \boldsymbol{k}}(\boldsymbol{x}) \tag{1.4}$$

is then projected onto each of the sublattice wavefunctions $\sum_R e^{i \boldsymbol{k} \boldsymbol{R}} \phi(\boldsymbol{x} - \boldsymbol{R})$ respectively, yielding expressions that contain overlaps of the type

$$\int \mathrm{d}\boldsymbol{x}\ \phi(\boldsymbol{x}-\boldsymbol{R}_i)\Big[\frac{-i\hbar^2\nabla^2}{2m}+\sum_{\boldsymbol{R}} V_{\mathrm{ion}}(\boldsymbol{x}-\boldsymbol{R})\Big]\phi(\boldsymbol{x}-\boldsymbol{R}_j).$$

When the sites $\boldsymbol{R}_i$ and $\boldsymbol{R}_j$ are equal, this overlap gives a constant $\mathcal{E}$, the eigenenergy of the orbital $\phi(\boldsymbol{x})$. When the two sites are nearest neighbors, the overlap integral gives the constant

$$\gamma \equiv \int \mathrm{d}\boldsymbol{x}\ \phi(\boldsymbol{x})\Big[\frac{-i\hbar^2\nabla^2}{2m}+\sum_{\boldsymbol{R}} V_{\mathrm{ion}}(\boldsymbol{x}-\boldsymbol{R})\Big]\phi(\boldsymbol{x}-\boldsymbol{b}_i), \tag{1.5}$$

which is the hopping energy between sublattices A and B. The second orbital is shifted by any of the three neighbor vectors $\boldsymbol{b}_i$, and which one is used does not affect the value of γ. The contributions from overlaps with more distant orbital pairs are neglected in this work. The plane-wave parts of the wavefunctions in the sums of all sites in (1.4) reduce to a sum over the three nearest neighbors, giving a factor

$$g_{\boldsymbol{k}} \equiv \sum_{n=1}^{3} e^{i\boldsymbol{k}\boldsymbol{b}_n} \tag{1.6}$$

in the nearest-neighbor terms. This function will come to play an important role in the following.

1.4 The tight-binding band structure

The two projections of (1.4) gives a matrix equation that the coefficients $C^{A,B}_{\lambda\boldsymbol{k}}$ must fulfill,

$$\begin{pmatrix} \mathcal{E}-E_{\lambda\boldsymbol{k}} & \gamma g_{\boldsymbol{k}} \\ \gamma g^*_{\boldsymbol{k}} & \mathcal{E}-E_{\lambda\boldsymbol{k}} \end{pmatrix} \begin{pmatrix} C^A_{\lambda\boldsymbol{k}} \\ C^B_{\lambda\boldsymbol{k}} \end{pmatrix} = 0\,. \tag{1.7}$$

The matrix equation has nonzero solutions only when the determinant is zero; this condition gives us an expression for the band dispersions $E_{\lambda\boldsymbol{k}}$. Since the orbital eigenenergy $\mathcal{E}$ causes a shift of both the conduction and the valence band, it has no physical consequences, and can be put to zero. As a solution, we get the tight-binding energy dispersion in graphene,

$$E_{\lambda\boldsymbol{k}} = \pm\gamma|g_{\boldsymbol{k}}|, \tag{1.8}$$

where the + sign is for the conduction band and − for the valence band.

These bands are shown in figure 1.4, with a few symmetry points marked. At the Γ point the bands are furthest apart, and at the M point the dispersion has saddle points. At the K^+ and K^- points the conduction and the valence band touch; there is no band gap. This is what makes graphene a semimetal — the density of states at the Fermi energy vanishes, which makes it difficult for electrons to move to higher energies, in spite of there being no band gap.

Close to the K^+ and K^- points, the bands rise and fall linearly as functions of $\boldsymbol{k}$, forming a cone. This conical dispersion resembles the dispersion relation of a massless relativistic particle, which is why the $K^\pm$ points are often referred to as the Dirac points. The geometry of graphene in momentum space is for clarity shown separately in figure 1.5. It exhibits the same honeycomb structure as graphene in real space, rotated by ninety degrees. In the middle of the Brillouin zone is the Γ point, and in the corners are the $K^\pm$ points.

The solution of the matrix equation (1.7) is $C^A_{\lambda\boldsymbol{k}} = \pm C^B_{\lambda\boldsymbol{k}} g_{\boldsymbol{k}} / |g_{\boldsymbol{k}}|$, and a choice for the coefficients which satisfies the normalization conditions is

$$C^A_{\lambda\boldsymbol{k}} = \pm\frac{1}{\sqrt{2}} \qquad \text{and} \qquad C^B_{\lambda\boldsymbol{k}} = \frac{1}{\sqrt{2}}\frac{g^*_{\boldsymbol{k}}}{|g_{\boldsymbol{k}}|} \tag{1.9}$$

which specifies the tight-binding wavefunction (1.3) completely. The wavefunction will be useful later on, to construct the matrix elements of the light–matter and electron–electron Hamiltonians.

1.5 The sublattice basis

Apart from the band basis, another convenient choice is the sublattice basis, which is well-defined at the present level of approximation, where overlaps between neighboring orbitals are neglected. In the sublattice basis the field operator is expanded as

$$\hat{\psi}(\boldsymbol{x}) = \sum_{\boldsymbol{k}} \Psi^A_{\boldsymbol{k}}(\boldsymbol{x})\hat{A}_{\boldsymbol{k}} + \Psi^B_{\boldsymbol{k}}(\boldsymbol{x})\hat{B}_{\boldsymbol{k}} \tag{1.10}$$

where the operators $\hat{A}_{\boldsymbol{k}}$ and $\hat{B}_{\boldsymbol{k}}$ annihilate an electron with momentum $\boldsymbol{k}$ in sublattice A or B. The sublattice wavefunctions $\Psi^A_{\boldsymbol{k}}(\boldsymbol{x})$ are the ones used to form the linear combination in the band-basis wavefunction (1.3). The transformation between the two bases is given by the coefficients $C^{A,B}_{\lambda\boldsymbol{k}}$,

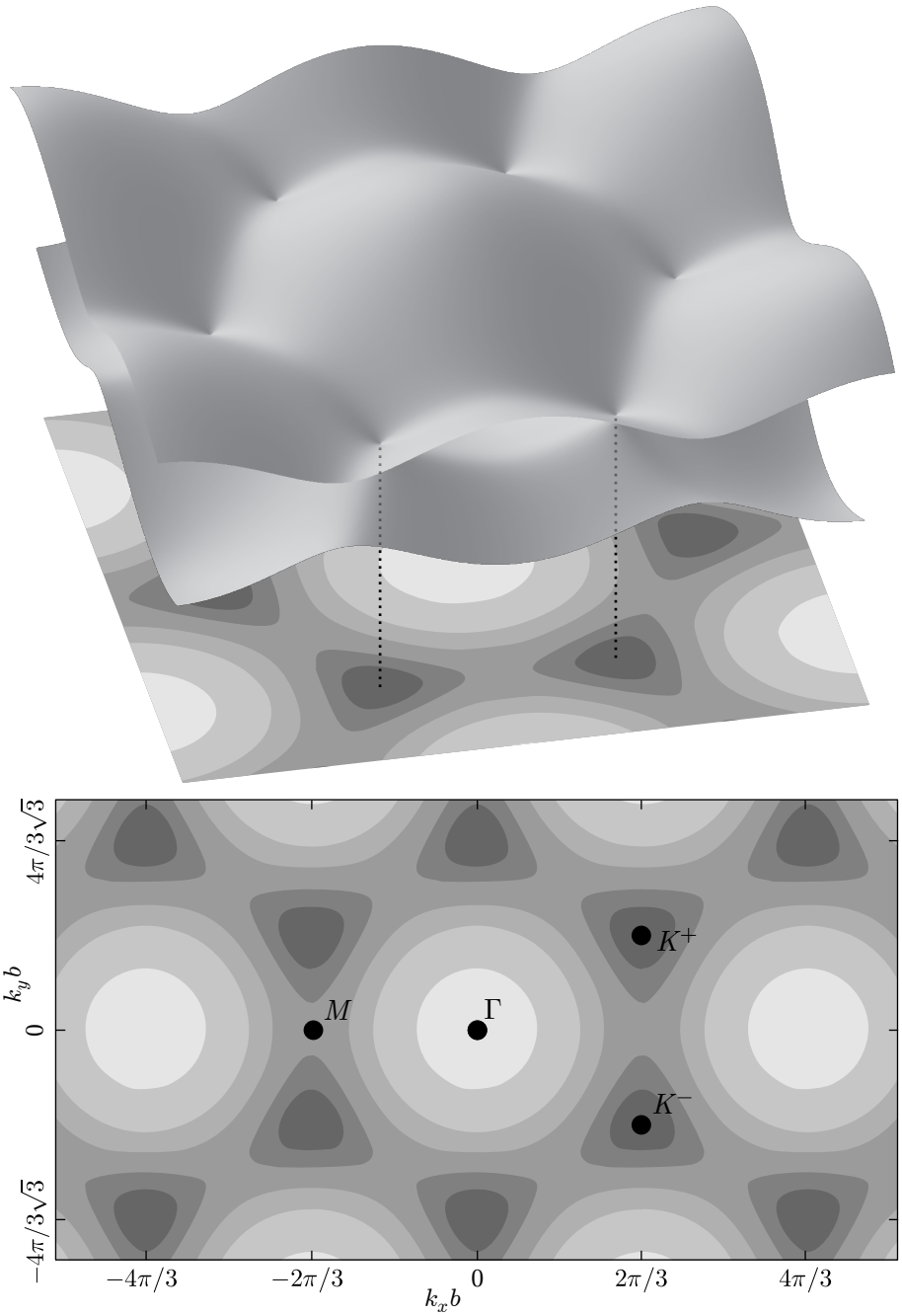

Figure 1.4 Above, the valence and conduction bands of graphene (1.8). Below, a planar representation of the energy difference between the bands. A large value is shown as a light color (around the Γ points) and a small value as a dark color, with the darkest areas around the Dirac points $K^{\pm}$.

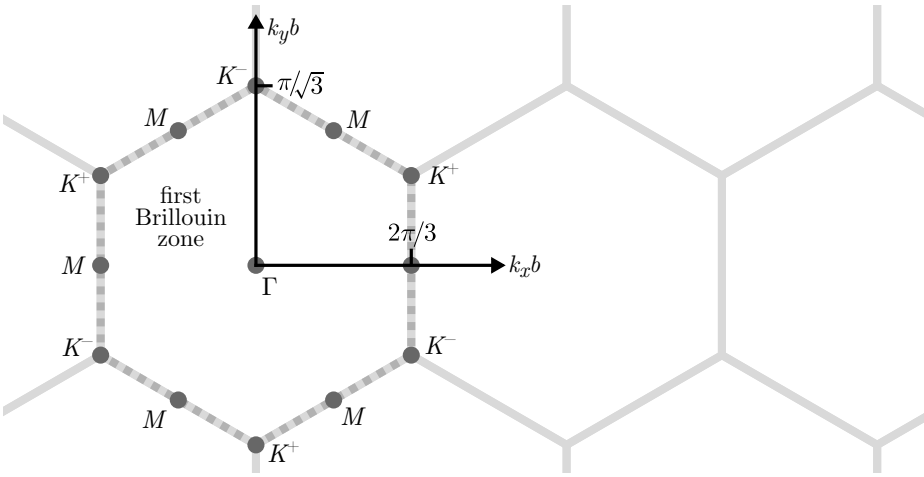

Figure 1.5 Momentum space of graphene, showing hexagonal Brillouin zones and positions of some of the symmetry points. The length scale is given in terms of the nearest-neighbor distance b.

$$\begin{pmatrix} \hat{A}_{\boldsymbol{k}} \\ \hat{B}_{\boldsymbol{k}} \end{pmatrix} = \frac{1}{\sqrt{2}} \begin{pmatrix} 1 & \frac{g_{\boldsymbol{k}}}{|g_{\boldsymbol{k}}|} \\ \frac{g_{\boldsymbol{k}}}{|g_{\boldsymbol{k}}|} & -1 \end{pmatrix} \begin{pmatrix} \hat{a}_{\mathrm{c}\boldsymbol{k}} \\ \hat{a}_{\mathrm{v}\boldsymbol{k}} \end{pmatrix}.$$

The single-particle Hamiltonian is expressed as

$$\begin{aligned} \hat{H}_0 = \hat{H}_{\mathrm{kin}} + \hat{H}_{\mathrm{e\text{–}ion}} &= \int \mathrm{d}\boldsymbol{x}\ \hat{\psi}(\boldsymbol{x})^\dagger \Big[\frac{-i\hbar^2\nabla^2}{2m} + \sum_{\boldsymbol{R}} V_{\mathrm{ion}}(\boldsymbol{x}\text{–}\boldsymbol{R}) \Big] \hat{\psi}(\boldsymbol{x}) \\ &= \sum_{\boldsymbol{k}} \gamma |g_{\boldsymbol{k}}| \Big(\hat{a}^\dagger_{\mathrm{c}\boldsymbol{k}} \hat{a}_{\mathrm{c}\boldsymbol{k}} - \hat{a}^\dagger_{\mathrm{v}\boldsymbol{k}} \hat{a}_{\mathrm{v}\boldsymbol{k}} \Big) \quad \text{in the band picture} \\ &= \sum_{\boldsymbol{k}} \Big(\gamma g_{\boldsymbol{k}} \hat{A}^\dagger_{\boldsymbol{k}} \hat{B}_{\boldsymbol{k}} + \gamma g^*_{\boldsymbol{k}} \hat{B}^\dagger_{\boldsymbol{k}} \hat{A}_{\boldsymbol{k}} \Big) \quad \text{in the sublattice picture.} \end{aligned} \tag{1.11}$$

1.6 The linear approximation close to the Dirac points

The function $g_{\boldsymbol{k}}$ (1.6) keeps appearing in the graphene tight-binding calculations; it is in the band basis expansion of the wavefunctions (1.3), in the single-particle energies (1.8), as well as in the matrix elements of the many-body Hamiltonian, which is discussed in the following two chapters.

The phase of $g_{\boldsymbol{k}}$ is plotted in figure 1.6. The complex phase is visualized as hue in the figure, with cyan as zero phase. Around the K^+ points, the phase increases in the positive (counter-clockwise) rotational direction and around the

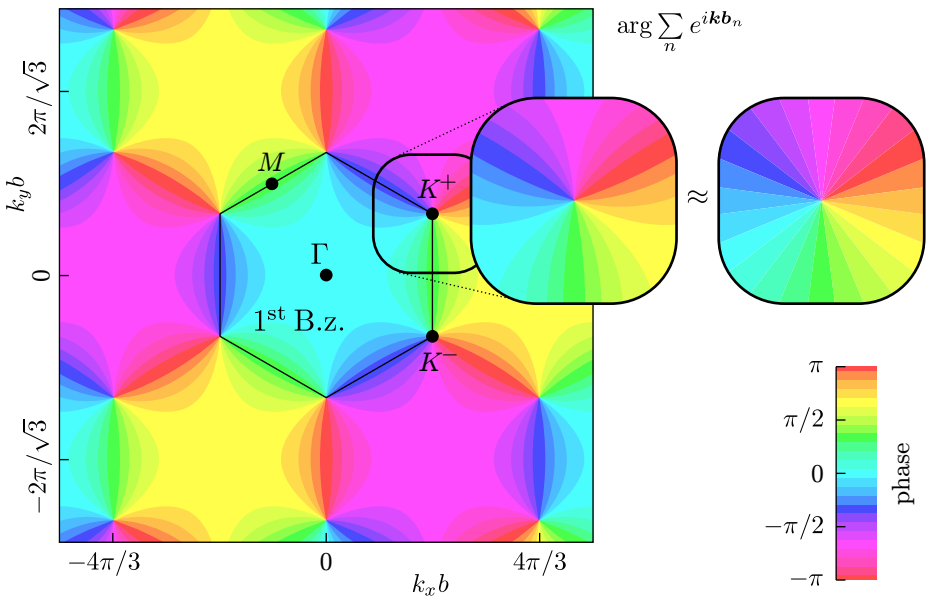

Figure 1.6 The complex phase of the neighbor vector sum $g_{\boldsymbol{k}}$ (1.6).

K^- points in the other direction. Interestingly, the phases in adjacent Brillouin zones differ by $\pm 2\pi/3$.

For many applications, only the low-energy band structure in the vicinity of the Dirac points is important. In this region, the neighbor vector sum $g_{\boldsymbol{k}}$ can be linearized, which leads to a simpler treatment of the theory, and clarifies the celebrated connection with massless relativistic particles. To this end, the function $g_{\boldsymbol{k}}$ is Taylor expanded around either Dirac point. Keeping only the first term, and calculating the gradient of $g_{\boldsymbol{k}}$ at the Dirac points, one can approximate

$$g_{\boldsymbol{k}} \approx (\boldsymbol{k}-\boldsymbol{K}^{\pm})\cdot\Big[\nabla_{\boldsymbol{k}} \sum_{n=1}^{3} e^{i\boldsymbol{k}\boldsymbol{b}_n}\Big]_{\boldsymbol{k}=\boldsymbol{K}^{\pm}} = \frac{3b}{2} e^{-i\pi/3}(\boldsymbol{k}-\boldsymbol{K}^{\pm})\cdot(\hat{\boldsymbol{e}}_x \pm i\hat{\boldsymbol{e}}_y)\,. \quad (1.12)$$

For the dispersion (1.8) we need only its absolute value,

$$E_{\boldsymbol{k}} = \gamma|g_{\boldsymbol{k}}| \approx \frac{3b\gamma}{2}|\boldsymbol{k}-\boldsymbol{K}^{\pm}|$$

where b is the distance between two neighboring carbon atoms. We see that the energy dispersions are indeed approximately linear in $\boldsymbol{k}$, as also shown in figure 1.7.

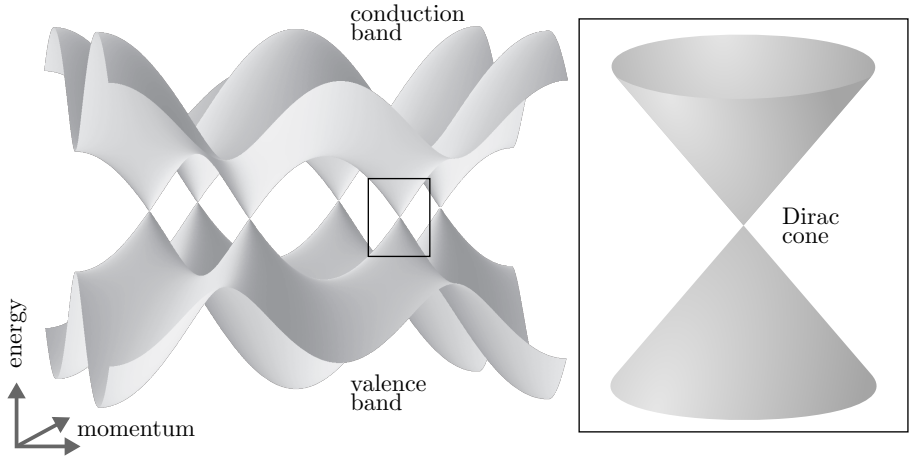

Figure 1.7 The band structure of graphene (1.8) with the valence and conduction bands. Where the two bands touch, the band structure forms a cone (1.13).

This Dirac cone is the single most interesting feature of graphene. For massless relativistic particles we have the relation $E(\boldsymbol{k}) = \hbar c|\boldsymbol{k}|$, c being the speed of light in vacuum. In graphene, the dispersion relation $E(\boldsymbol{k}) = 3b\gamma|\boldsymbol{k}|/2$ can be expressed as

$$E_{\boldsymbol{k}} = \hbar v_F |\boldsymbol{k}| \tag{1.13}$$

with a velocity constant $v_F = 3b\gamma/2\hbar$. This is the so-called Fermi velocity in graphene which is approximately 300 times smaller than the speed of light in vacuum.

Later on, when dealing with other electrons and light, the linear approximation will be needed also for the phase of $g_{\boldsymbol{k}}$. Close to the Dirac points, the phase can be approximated as the angle of the coordinate vector, as shown in the inset of figure 1.6.

$$\frac{g_{\boldsymbol{k}}}{|g_{\boldsymbol{k}}|} = \frac{\sum_{n=1}^{3} e^{i\boldsymbol{k}\boldsymbol{b}_n}}{\left|\sum_{n=1}^{3} e^{i\boldsymbol{k}\boldsymbol{b}_n}\right|} \approx e^{\pm i(\theta + \frac{5\pi}{6})} \quad \text{where } \theta = \arg(\boldsymbol{k} - \boldsymbol{K}^{\pm})$$

where $+$ and $-$ in the phase correspond to the two Dirac points $K^{\pm}$. The constant in the phase ($5\pi/6$ for these particular Dirac points) depends on which Dirac point one is looking at, but is in itself of no consequence for the actual calculations in the present work.

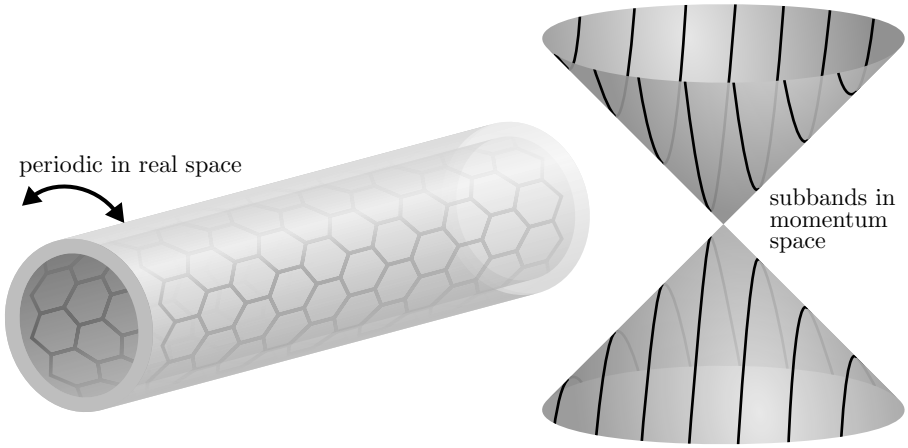

Figure 1.8 Subbands in a semiconducting carbon nanotube, formed as the real-space periodicity of the lattice confines allowed momentum values to discrete lines.

1.7 Tight-binding for graphene in lower dimensions — carbon nanotubes

In Paper I we look at electron dynamics in a special form of graphene — a carbon nanotube. A carbon nanotube is a rolled-up sheet of graphene in which the electrons move primarily along the tube axis. For us, this was a convenient test case for our graphene equations of motion. Due to their one-dimensional nature and the presence of a band gap in certain forms of carbon nanotubes, they are a natural first choice for applying the semiconductor-like many-body approach to a graphene-like system.

Rolling up the graphene sheet and connecting the edges makes the system periodic along the tube circumference. For the electrons, as a consequence, only certain discrete momentum values are allowed in that direction. The other component of the in-plane momentum, along the tube axis, is still unrestricted and can be taken as continuous for a long enough tube.

Thus, the allowed k states form discrete lines in momentum space. The energy dispersion is consequently restricted to slashes in the band structure, as shown in figure 1.8. These slashes are called subbands. The electron in a subband can easily be transferred between k states within a subband, whereas moving the electron between subbands requires a larger transfer of momentum. A one-dimensional system is easy to solve numerically, but the existence of the different subbands in carbon nanotubes gives some additional structure to the equations.

There are a number of different possibilities for rolling up the graphene sheet; the tube can have different diameters, and the sheet can be rolled at different angles. Depending on how the tube is rolled up, the subbands appear at different angles and periodicities in the dispersion. If a subband happens to cross the Dirac point, that subband will have a zero energy gap, and the nanotube will be metallic. If none of the slashes cross a Dirac point, as is the case in figure 1.8, the nanotube is a semiconductor. If the dynamics are restricted to one or a few subbands, the electronic system of the carbon nanotube will resemble that of a one-dimensional semiconductor. Such is the system of Paper I.

1.8 Parameters in the model

Name		Value	Relation
Nearest neighbor distance	b	$1.42{\cdot}10^{-10}$ m	(1.2)
Effective sheet thickness	d	$1.76{\cdot}10^{-11}$ m	(1.1), (2.6)
Intersite energy	γ	2.8 eV	overlap (1.5)
Fermi velocity	v_F	$9.07{\cdot}10^{5}$ m/s [9]	$\gamma = 2\hbar v_F/b$
Energy scale	E_0	33.8 eV	$\hbar v_F/d$
Coulomb strength	α	2.4	$e^2/4\pi\epsilon\epsilon_0\hbar v_F$ (2.10)
Bilayer graphene			
Distance between layers	L	$3.5{\cdot}10^{-10}$ m	(9.1)
Interlayer energy	γ'	400 meV	overlap (9.2)

The extension of the p_z orbital is determined by its overall scale, the parameter d in (1.1). In this way, the parameter d acts as an effective thickness of the graphene sheet, as discussed further in section 2.3. The parameter d sets a length scale, and determines the energy scale $\hbar v_F/d$, together with the Fermi velocity v_F. In the tight-binding calculations, d is a free parameter. With density functional calculations, it is possible to calculate the actual shape of the electron distribution. This has been done for graphene by John Sipe et al [10]. The distribution showed a reasonable p_z orbital character, with the length parameter $d \approx 1.76{\cdot}10^{-11}$ m.

It is worth noting that the nearest-neighbor distance b is not the same as the lattice constant of graphene ($\sqrt{3}b = 2.461{\cdot}10^{-10}$m, the distance between unit cells) which some authors use as their length scale in the literature.

Chapter 2

Modeling the electron–electron interaction

In the tight-binding calculations in the previous chapter, only the interaction between electrons and the atomic lattice was considered. To build a many-body theory, we need to account also for the interaction between electrons. This is especially the case when studying the strong-coupling phase in chapter 7, which as a phenomenon is based completely on this interaction. In this chapter, I discuss including the electron–electron interaction in the form of a new term in the Hamiltonian, expressed in the tight-binding basis from the previous chapter.

2.1 Deriving the tight-binding Coulomb Hamiltonian

The Coulomb energy of two electrons at positions $\boldsymbol{x}$ and $\boldsymbol{x}'$ is

$$V(|\boldsymbol{x}-\boldsymbol{x}'|) = \frac{1}{4\pi\epsilon\epsilon_0|\boldsymbol{x}-\boldsymbol{x}'|}.$$

Since the strength of the Coulomb interaction is going to be crucial for our calculations, it is worth noting the dielectric constant $\epsilon \geq 1$ in the denominator, making the Coulomb interaction weaker in the material than it would be in vacuum.

The Coulomb Hamiltonian, illustrated in figure 2.1, has the form

$$\hat{H}_{\text{coul}} = \frac{1}{2}\sum_{1234} V_{1234}\ \hat{a}_1^\dagger \hat{a}_2^\dagger \hat{a}_3 \hat{a}_4\,, \qquad 1 = \{\lambda_1\, \boldsymbol{k}_1\}\,, \tag{2.1}$$

where the general Coulomb matrix element V_{1234} is defined as

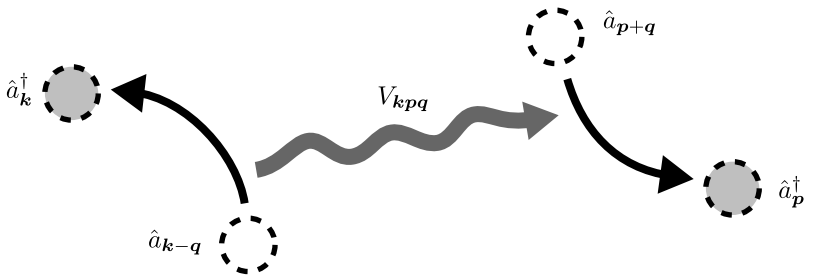

Figure 2.1 Two electrons interacting. The figure shows the processes in the Coulomb Hamiltonian (2.4) where the momentum $\hbar\boldsymbol{q}$ is transferred between two electrons, with a weight given by the Coulomb potential $V_{\boldsymbol{kpq}}$.

$$V_{1234} \equiv \int \mathrm{d}\boldsymbol{x} \int \mathrm{d}\boldsymbol{x}' \; \Psi_1^*(\boldsymbol{x})\Psi_2^*(\boldsymbol{x}')V(|\boldsymbol{x}-\boldsymbol{x}'|)\Psi_3(\boldsymbol{x}')\Psi_4(\boldsymbol{x}). \tag{2.2}$$

In order to calculate V_{1234}, we introduce the Fourier transform $V_{\boldsymbol{q}}^{\mathrm{3D}}$ of the Coulomb potential,

$$V(|\boldsymbol{x}-\boldsymbol{x}'|) = \sum_{\boldsymbol{q}} V_{\boldsymbol{q}}^{\mathrm{3D}} e^{i\boldsymbol{q}(\boldsymbol{x}-\boldsymbol{x}')}, \quad \text{where} \quad V_{\boldsymbol{q}}^{\mathrm{3D}} = \frac{e^2}{\epsilon\epsilon_0 \mathcal{L}\mathcal{A}|\boldsymbol{q}|^2}\,.$$

The constants $\mathcal{L}$ and $\mathcal{A}$ are the quantization length and area, which measure the real-space volume of the system. Using the Fourier transform $V_{\boldsymbol{q}}^{\mathrm{3D}}$, we can split the matrix element V_{1234} into two similar integrals:

$$V_{1234} = \sum_{\boldsymbol{q}} V_{\boldsymbol{q}}^{\mathrm{3D}} \underbrace{\int \mathrm{d}\boldsymbol{x} \; \Psi_1^*(\boldsymbol{x}) e^{i\boldsymbol{qx}} \Psi_4(\boldsymbol{x})}_{\equiv I^{\lambda_1\lambda_4}_{\boldsymbol{k}_1\boldsymbol{k}_4\boldsymbol{q}}} \underbrace{\int \mathrm{d}\boldsymbol{x}' \Psi_2^*(\boldsymbol{x}') e^{-i\boldsymbol{qx}'} \Psi_3(\boldsymbol{x}')}_{= I^{\lambda_2\lambda_3 *}_{\boldsymbol{k}_2\boldsymbol{k}_3\boldsymbol{q}}}\,. \tag{2.3}$$

To evaluate the integrals and obtain the tight-binding Coulomb matrix element, we insert the tight-binding expansion (1.3) for the wavefunctions $\Psi_{\lambda\boldsymbol{k}}(\boldsymbol{x})$. This gives double sums over carbon atom sites, containing the electron tight-binding orbitals $\phi(\boldsymbol{x})$ (1.1). In the sums, we discard all but same-site terms, due to the overlap between neighboring sites being significantly smaller. For the integrals, this gives a term each for the sublattices A and B, each containing a sum over all sites in the sublattice, giving momentum conservation in the plane.

$$I^{\lambda\lambda'}_{\boldsymbol{k}\boldsymbol{k}'\boldsymbol{q}} = (C^{A*}_{\lambda\boldsymbol{k}} C^{A}_{\lambda'\boldsymbol{k}'} + \; C^{B*}_{\lambda\boldsymbol{k}} C^{B}_{\lambda'\boldsymbol{k}'}) \underbrace{\frac{1}{N}\sum_{\boldsymbol{R}} e^{-i(\boldsymbol{k}-\boldsymbol{k}'-\boldsymbol{q})\boldsymbol{R}}}_{= \delta_{\boldsymbol{k}',\,\boldsymbol{k}-\boldsymbol{q}_\parallel}} \underbrace{\int \mathrm{d}\boldsymbol{x}\, \phi(\boldsymbol{x})^* e^{i\boldsymbol{qx}} \phi(\boldsymbol{x})}_{\equiv G(\boldsymbol{q})}$$

Both terms contain a Fourier transform of electron orbitals $\phi(\boldsymbol{x})$ (1.1) which we denote by $G(\boldsymbol{q})$. Using these results for the integrals $I^{\lambda\lambda'}_{\boldsymbol{k}\boldsymbol{k}'\boldsymbol{q}}$ and the expressions (1.9) for the functions $C^{A,B}_{\lambda\boldsymbol{k}}$, we obtain the Coulomb matrix element as

$$V_{1234} = \frac{1}{4}\sum_{\boldsymbol{q}_\parallel}\delta_{\boldsymbol{k}_4,\boldsymbol{k}_1-\boldsymbol{q}_\parallel}\delta_{\boldsymbol{k}_3,\boldsymbol{k}_2+\boldsymbol{q}_\parallel}\left(\frac{g_{\boldsymbol{k}_1}g^*_{\boldsymbol{k}_1-\boldsymbol{q}_\parallel}}{\left|g_{\boldsymbol{k}_1}g_{\boldsymbol{k}_1-\boldsymbol{q}_\parallel}\right|}\pm 1\right)\left(\frac{g_{\boldsymbol{k}_2}g^*_{\boldsymbol{k}_2+\boldsymbol{q}_\parallel}}{\left|g_{\boldsymbol{k}_2}g_{\boldsymbol{k}_2+\boldsymbol{q}_\parallel}\right|}\pm 1\right) \times \underbrace{\sum_{q_z} V^{3D}_{\boldsymbol{q}}|G(\boldsymbol{q})|^2}_{\equiv W(\boldsymbol{q}_\parallel)}$$

where '+' in the first parenthesis is chosen when $\lambda_1 = \lambda_4$, and '−' when $\lambda_1 \neq \lambda_4$, and correspondingly for λ_2 and λ_3 in the second parenthesis. The Coulomb matrix element has three parts: momentum conservation in the plane expressed by the delta functions, graphene lattice geometry contained in the $g_{\boldsymbol{k}}$ functions (1.6) and the function $W(\boldsymbol{q}_\parallel)$ which acts as a weight for the exchanged momentum. It can be noted that $W(\boldsymbol{q}_\parallel)$ is independent of the lattice geometry, and contains only the shape of the carbon orbitals.

2.2 Tight-binding Coulomb matrix elements

Inserting the Coulomb matrix element V_{1234} derived above in the Coulomb Hamiltonian (2.1), one of the momentum sums can be performed due to momentum conservation. Grouping the terms by the types of band transitions involved, the Coulomb Hamiltonian acquires the form

$$\begin{aligned}
\hat{H}_{\text{coul}} = \frac{1}{2}\sum_{\boldsymbol{k}\boldsymbol{p}\boldsymbol{q}} V^{+}_{\boldsymbol{k}\boldsymbol{p}\boldsymbol{q}} \Big[&\hat{a}^\dagger_{\mathrm{c}\boldsymbol{k}}\hat{a}^\dagger_{\mathrm{c}\boldsymbol{p}}\hat{a}_{\mathrm{c}\boldsymbol{p}+\boldsymbol{q}}\hat{a}_{\mathrm{c}\boldsymbol{k}-\boldsymbol{q}} + \hat{a}^\dagger_{\mathrm{v}\boldsymbol{k}}\hat{a}^\dagger_{\mathrm{v}\boldsymbol{p}}\hat{a}_{\mathrm{v}\boldsymbol{p}+\boldsymbol{q}}\hat{a}_{\mathrm{v}\boldsymbol{k}-\boldsymbol{q}} \\
&+ \hat{a}^\dagger_{\mathrm{c}\boldsymbol{k}}\hat{a}^\dagger_{\mathrm{v}\boldsymbol{p}}\hat{a}_{\mathrm{v}\boldsymbol{p}+\boldsymbol{q}}\hat{a}_{\mathrm{c}\boldsymbol{k}-\boldsymbol{q}} + \hat{a}^\dagger_{\mathrm{v}\boldsymbol{k}}\hat{a}^\dagger_{\mathrm{c}\boldsymbol{p}}\hat{a}_{\mathrm{c}\boldsymbol{p}+\boldsymbol{q}}\hat{a}_{\mathrm{v}\boldsymbol{k}-\boldsymbol{q}}\Big] \\
+\frac{1}{2}\sum_{\boldsymbol{k}\boldsymbol{p}\boldsymbol{q}} V^{-}_{\boldsymbol{k}\boldsymbol{p}\boldsymbol{q}} \Big[&\hat{a}^\dagger_{\mathrm{c}\boldsymbol{k}}\hat{a}^\dagger_{\mathrm{c}\boldsymbol{p}}\hat{a}_{\mathrm{v}\boldsymbol{p}+\boldsymbol{q}}\hat{a}_{\mathrm{v}\boldsymbol{k}-\boldsymbol{q}} + \hat{a}^\dagger_{\mathrm{v}\boldsymbol{k}}\hat{a}^\dagger_{\mathrm{v}\boldsymbol{p}}\hat{a}_{\mathrm{c}\boldsymbol{p}+\boldsymbol{q}}\hat{a}_{\mathrm{c}\boldsymbol{k}-\boldsymbol{q}} \\
&+ \hat{a}^\dagger_{\mathrm{c}\boldsymbol{k}}\hat{a}^\dagger_{\mathrm{v}\boldsymbol{p}}\hat{a}_{\mathrm{c}\boldsymbol{p}+\boldsymbol{q}}\hat{a}_{\mathrm{v}\boldsymbol{k}-\boldsymbol{q}} + \hat{a}^\dagger_{\mathrm{v}\boldsymbol{k}}\hat{a}^\dagger_{\mathrm{c}\boldsymbol{p}}\hat{a}_{\mathrm{v}\boldsymbol{p}+\boldsymbol{q}}\hat{a}_{\mathrm{c}\boldsymbol{k}-\boldsymbol{q}}\Big] \\
+\sum_{\boldsymbol{k}\boldsymbol{p}\boldsymbol{q}} V^{\mathrm{A}}_{\boldsymbol{k}\boldsymbol{p}\boldsymbol{q}} \Big[&\hat{a}^\dagger_{\mathrm{c}\boldsymbol{k}}\hat{a}^\dagger_{\mathrm{c}\boldsymbol{p}}\hat{a}_{\mathrm{v}\boldsymbol{p}+\boldsymbol{q}}\hat{a}_{\mathrm{c}\boldsymbol{k}-\boldsymbol{q}} + \hat{a}^\dagger_{\mathrm{v}\boldsymbol{k}}\hat{a}^\dagger_{\mathrm{v}\boldsymbol{p}}\hat{a}_{\mathrm{c}\boldsymbol{p}+\boldsymbol{q}}\hat{a}_{\mathrm{v}\boldsymbol{k}-\boldsymbol{q}} \\
&+ \hat{a}^\dagger_{\mathrm{c}\boldsymbol{k}}\hat{a}^\dagger_{\mathrm{v}\boldsymbol{p}}\hat{a}_{\mathrm{c}\boldsymbol{p}+\boldsymbol{q}}\hat{a}_{\mathrm{c}\boldsymbol{k}-\boldsymbol{q}} + \hat{a}^\dagger_{\mathrm{v}\boldsymbol{k}}\hat{a}^\dagger_{\mathrm{c}\boldsymbol{p}}\hat{a}_{\mathrm{v}\boldsymbol{p}+\boldsymbol{q}}\hat{a}_{\mathrm{v}\boldsymbol{k}-\boldsymbol{q}}\Big]
\end{aligned} \tag{2.4}$$

where the matrix elements now are expressed as

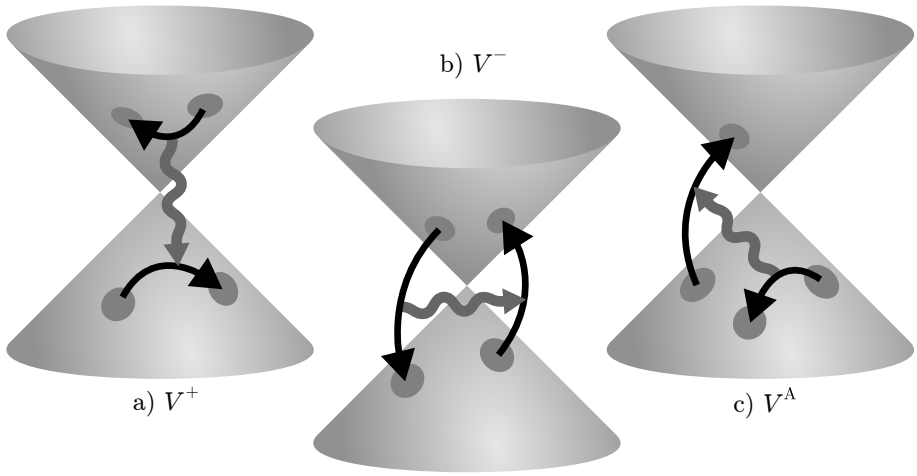

Figure 2.2 The processes governed by the different terms in (2.4). In a) the electrons stay in their respective bands, in b) both electrons change bands, and in c) an Auger process.

$$
\begin{aligned}
V^{+}_{\boldsymbol{kpq}} &\equiv \frac{1}{4}W(\boldsymbol{q})\left(\frac{g_{\boldsymbol{k}}g^{*}_{\boldsymbol{k}-\boldsymbol{q}}}{|g_{\boldsymbol{k}}g_{\boldsymbol{k}-\boldsymbol{q}}|}+1\right)\left(\frac{g_{\boldsymbol{p}}g^{*}_{\boldsymbol{p}+\boldsymbol{q}}}{|g_{\boldsymbol{p}}g_{\boldsymbol{p}+\boldsymbol{q}}|}+1\right)\\
V^{-}_{\boldsymbol{kpq}} &\equiv \frac{1}{4}W(\boldsymbol{q})\left(\frac{g_{\boldsymbol{k}}g^{*}_{\boldsymbol{k}-\boldsymbol{q}}}{|g_{\boldsymbol{k}}g_{\boldsymbol{k}-\boldsymbol{q}}|}-1\right)\left(\frac{g_{\boldsymbol{p}}g^{*}_{\boldsymbol{p}+\boldsymbol{q}}}{|g_{\boldsymbol{p}}g_{\boldsymbol{p}+\boldsymbol{q}}|}-1\right)\\
V^{\mathrm{A}}_{\boldsymbol{kpq}} &\equiv \frac{1}{4}W(\boldsymbol{q})\left(\frac{g_{\boldsymbol{k}}g^{*}_{\boldsymbol{k}-\boldsymbol{q}}}{|g_{\boldsymbol{k}}g_{\boldsymbol{k}-\boldsymbol{q}}|}+1\right)\left(\frac{g_{\boldsymbol{p}}g^{*}_{\boldsymbol{p}+\boldsymbol{q}}}{|g_{\boldsymbol{p}}g_{\boldsymbol{p}+\boldsymbol{q}}|}-1\right)
\end{aligned}
\tag{2.5}
$$

with the radially symmetric part, the function $W(\boldsymbol{q})$ defined in section 2.3. The matrix elements for these processes are denoted V^+ and V^- for the signs in the expressions in (2.5) and V^{A} for Auger processes.

We see that the Coulomb Hamiltonian in graphene has three different types of terms, which account for whether the interacting electrons stay in their original bands or not. These different types have different Coulomb matrix elements. The terms with V^+ describe processes where both electrons stay in their original bands, in the V^- terms both electrons change band, and in the V^{A} terms, one electron changes band while the other one stays. This third process does not conserve the number of particles in a band — this is called an Auger process. These three types of processes are illustrated in figure 2.2.

2.3 Consequences of the finite sheet thickness

The Coulomb interaction takes place in three dimensions, while we have two coordinates in the graphene plane. The electrons in the material are confined

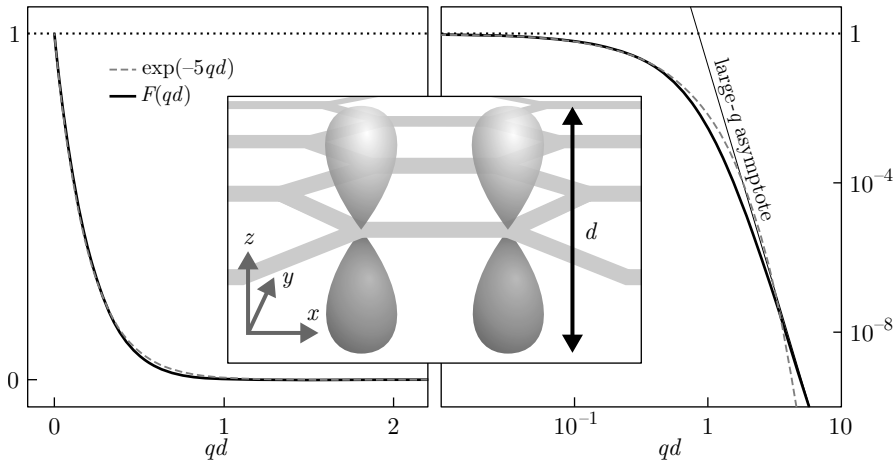

Figure 2.3 The form function $F(qd)$ (2.7) plotted as a thick solid line. On the right, the form function and its asymptotes are plotted in a double-logarithmic scale, in which power laws show up as straight lines.

to the orbitals of figure 1.2, which have a certain extension out of the plane, in the z direction. With the function $W(\boldsymbol{q})$ in (2.5) we have created an effectively two-dimensional Coulomb interaction, which accounts for how the electrons are localized in their orbitals.

The extension of the orbitals is accounted for by averaging the interaction over the direction perpendicular to the graphene sheet. The weight function in the Coulomb matrix elements (2.5) appears as a modification of a pure three-dimensional Coulomb potential, $e^2/\epsilon\epsilon_0\mathcal{L}\mathcal{A}|\boldsymbol{q}|^2$. The three-dimensional potential is averaged in the z direction, weighted with a Fourier transform of two p_z orbitals,

$$W(\boldsymbol{q}_\parallel) = \frac{e^2}{\epsilon\epsilon_0\mathcal{L}\mathcal{A}} \sum_{q_z} \frac{1}{|\boldsymbol{q}|^2} \left| \int \mathrm{d}\boldsymbol{x} e^{i\boldsymbol{q}\boldsymbol{x}} |\phi(\boldsymbol{x})|^2 \right|^2 .$$

In the expression above, the momentum $\boldsymbol{q}$ is three-dimensional, and $\boldsymbol{q}_\parallel$ is the in-plane momentum. The integral over $\boldsymbol{x}$ can be calculated analytically, using Fourier transforms of hydrogen orbitals [11]. It is then possible to perform the q_z-integration using Mathematica [12, 13] to arrive at expression (2.6).

Our quasi-2D potential can be conveniently expressed as a modification of a strict 2D potential,

$$W(\boldsymbol{q}) = \frac{e^2}{2\epsilon\epsilon_0\mathcal{A}} \frac{F(qd)}{|\boldsymbol{q}|} \tag{2.6}$$

where the modification is the form function $F(qd)$. The form function has the expression

$$F(X) = \left(1 + 6X^2\right)^2 - \frac{X\,\Xi(X)}{512\sqrt{1+X^2}^{\,11}} \tag{2.7}$$

with

$$\Xi(X) = 2475 + 25410\,X^2 + 112728\,X^4 + 261360\,X^6 + 344960\,X^8 + 262400\,X^{10} + 107520\,X^{12} + 18432\,X^{14}, \tag{2.8}$$

shown in figure 2.3.

$F(qd)$ is smaller than one, except at $q = 0$. The length parameter d can be seen as an effective thickness of the graphene sheet. The Coulomb interaction between electrons in the p_z orbitals is much weaker than it would be between electrons strictly confined to the plane, since the electrons in the orbitals are further apart. At very large in-plane distances (corresponding to $q = 0$) however, the extension of the orbitals is negligible, and the Coulomb interaction looks like the one for a strictly two-dimensional case, which is reflected in $F(qd = 0) = 1$.

For numerical calculations, it can be noted that for large q values, the function can be difficult to evaluate; the two terms of (2.7) both have large positive values, which cancel to a small positive number.

For large values of q, the form function decays as a power law of q,

$$F(qd) \sim \frac{1155}{8192}\,\frac{1}{(qd)^{12}} \qquad q \text{ large.}$$

For small values of q, $F(qd) \sim 1$, and the Coulomb potential behaves like the potential for an infinitely thin, strictly two-dimensional quantum well,

$$W(q) \sim \frac{e^2}{2\epsilon\epsilon_0 \mathcal{A}}\,\frac{1}{q} \qquad q \text{ small.}$$

In the right panel if figure 2.3, the large-q asymptote is a thin solid line, and the small-q asymptote is the dotted line at 1.

The decay of the form function can be approximated reasonably well with an exponential drop-off $\exp(-5qd)$ plotted as a grey dashed line in figure 2.3. A potential of this type is known as an Ohno potential, and is commonly used to describe an effectively two- or one-dimensional situation. The Ohno potential is the momentum-space version of a real-space potential between two charges which cannot get arbitrarily close to each other, $V(\boldsymbol{x}) \propto [x^2 + y^2 + (5d)^2]^{-1/2}$.

2.4 The coupling strength

By scaling the Hamiltonian into a unitless form, one observes some important consequences of the linear dispersion. Suppressing the band index and other details for a moment, the Hamiltonian for the electrons is

$$\hat{H} = \sum_{\boldsymbol{k}} \underbrace{E_k}_{\hbar v_F k} \hat{a}^\dagger_{\boldsymbol{k}} \hat{a}_{\boldsymbol{k}} + \sum_{\boldsymbol{q}} \underbrace{W(q)}_{\frac{e^2 F(qd)}{2\epsilon\epsilon_0 \mathcal{A} q}} \times (\text{geometry}) \times \hat{a}^\dagger \hat{a}^\dagger \hat{a}\ \hat{a}\ .$$

Judging from the first term, to convert the Hamiltonian into a dimensionless form, we have to divide by $\hbar v_F$ and multiply by a length. Choosing the layer thickness d as the length gives the simplest expression for the form function in the Coulomb term. The inverse of the length will act as a scale for all wavenumbers, and the energy $\hbar v_F/d$ as a scale for all quantities with the dimension of energy. Writing the scaled wavenumbers as X and Y, we get

$$\frac{\hat{H}}{\hbar v_F/d} = \sum_X X \hat{a}^\dagger_X \hat{a}_X + \frac{e^2}{4\pi\epsilon\epsilon_0 \hbar v_F} \frac{2\pi}{\mathcal{A}/d^2} \sum_Y \frac{F(Y)}{Y} \times \ldots \tag{2.9}$$

As a prefactor to the Coulomb term, we are left with a dimensionless quantity, the coupling strength

$$\alpha \equiv \frac{e^2}{4\pi\epsilon\epsilon_0 \hbar v_F} \quad \text{(in SI units)}. \tag{2.10}$$

The coupling strength can be seen as a measure of the Coulomb energy of two electrons on neighboring sites, $e^2/4\pi\epsilon\epsilon_0 b$, versus the hopping energy between two such sites, $\hbar v_F/b$. The appearance of the coupling strength in this form is independent of the choice of d as a length scale. In fact, without the form function, the choice would not show up at all, and the energy scale would be completely arbitrary.

It can be noted at this point that for a quadratic dispersion, $E_k = \hbar^2 k^2/2m$, one would scale the Hamiltonian with $\hbar^2/2ma^2$ (a a yet unchosen length) which would give a prefactor

$$\frac{e^2 m}{\epsilon\epsilon_0 \hbar^2} \frac{1}{q\mathcal{A}/a^2}$$

in the Coulomb term. Choosing the length a as the hydrogen Bohr radius $4\pi\epsilon\epsilon_0\hbar^2/e^2m$ eliminates all natural constants from the Hamiltonian, leaving the quadratic-dispersion system completely scaled and parameter-free.

The strength of all Coulomb phenomena are determined by the coupling strength. For a graphene sheet on its own, in air or in vacuum, the Coulomb interaction is at its maximal strength. If the sheet is placed on some other material, it weakens the electric fields. How much the field is weakened is determined by the permittivity ϵ of the material. The net field weakening experienced by charges in the graphene sheet is usually taken as an average of the permittivities of the materials above and below the graphene sheet, $\epsilon_{\text{graphene}} = (\epsilon_{\text{above}} + \epsilon_{\text{below}})/2$, with the reasoning that most of the three-dimensional electric field passes through either one of the encasing materials.

For electrons and photons in vacuum, the coupling strength is the fine-structure constant $e^2/4\pi\epsilon\epsilon_0\hbar c$. It has a value of approximately $1/137$, which is much smaller that 1. In quantum electrodynamics, the fine-structure constant is used as a small expansion parameter. In graphene, c is replaced by v_F, and the corresponding parameter combination is 300 times larger, approximately 2.4. This creates a great interest in graphene, since this large coupling strength could create very strong quantum electrodynamical effects.

Chapter 3

Interaction between electrons and light

In this chapter, I discuss how the electronic system in graphene interacts with an external electric field. In order to model this interaction process, light–matter terms are included in the Hamiltonian. The light causes transitions between the electronic states, and is typically the source of dynamics in the electronic system. These are the dynamics one wishes to study with the present type of many-body theory, as will be discussed in chapters 4 and 5. Some of the techniques introduced in this chapter will also be of use when looking for the strong-coupling phase in chapter 6.

The processes involved are the following. Light is shone on the graphene sheet, photons are absorbed by the material, and the graphene electrons gain the energy and momentum carried by the photons. The energy gain corresponds to a transition in the material, like those shown in figure 3.1. The electrons can absorb photons by either moving higher in energy within the same band, in an intraband process, or by moving to a higher band, in an interband process.

In a standard semiconductor, where there is a significant band gap, it is usually a reasonable approximation to treat inter- and intraband processes separately, since they are caused by absorbing photons with energies of different orders of magnitude. The interband processes are driven by visible light, and intraband processes by light with terahertz frequencies. In contrast, close to the Dirac point in graphene, the relevant low frequencies will drive both inter- and intraband processes equally strongly.

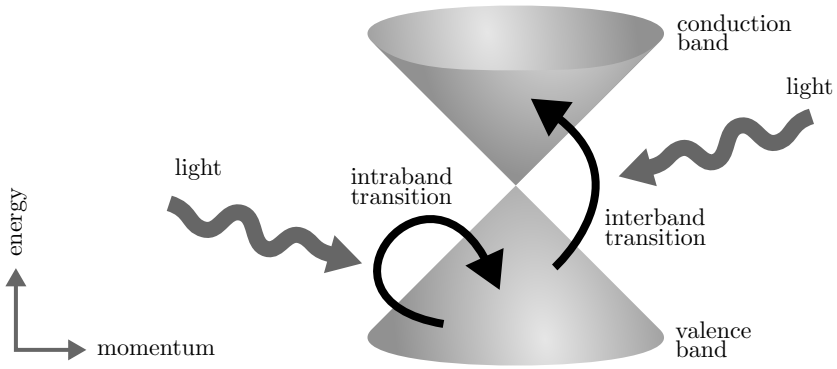

Figure 3.1 Electronic transitions in graphene caused by absorption of photons from an external electric field.

3.1 Derivation of the electron–light interaction Hamiltonian

In the presence of an external field $\boldsymbol{A}$, the kinetic energy of an electron is $(\hat{\boldsymbol{p}} - e\boldsymbol{A})^2/2m$. Expanding the parenthesis, the first term is the kinetic energy of the electron in absence of a field, which gave us the band structure part of the Hamiltonian (1.11). There is also a term linear in the external field, and one term proportional to $\boldsymbol{A}^2$. The expression for the linear term in graphene is treated in this chapter. The field squared term is of relevance for describing the light consistently, as discussed e.g. in Paper IV and [14], but is not considered further in this chapter.

Hence, the relevant electron–light Hamiltonian (in the so-called dipole approximation [4]) is of the form

$$\hat{H}_{\text{e–light}} = \sum_{\lambda\lambda'\boldsymbol{k}\boldsymbol{k}'} \int \mathrm{d}\boldsymbol{x}\ \Psi^*_{\lambda\boldsymbol{k}}(\boldsymbol{x}) \left[-\frac{e}{m}\hat{\boldsymbol{p}}\cdot\boldsymbol{A}(t)\right] \Psi_{\lambda'\boldsymbol{k}'}(\boldsymbol{x})\ \hat{a}^\dagger_{\lambda\boldsymbol{k}}\hat{a}_{\lambda'\boldsymbol{k}'} \tag{3.1}$$

where the sums over bands λ and λ' run over the conduction and valence bands, and the momentum sum is over the first Brillouin zone. The field $\boldsymbol{A}(t)$ causes a transition from band λ' to band λ, with a coupling strength given by the optical matrix element $\boldsymbol{p}_{\boldsymbol{k}}^{\lambda\lambda'}$. The transition will here be assumed to happen at a fixed momentum $\boldsymbol{k}$. This is an approximation, which contains the assumption that the photon momentum is small enough to be neglected. This is equivalent to assuming that the field is spatially constant over the relevant region of space. A situation where this approximation does not hold is studied in Paper I and chapter 5.

With a negligible photon momentum, the Hamiltonian for interaction with light is of the form

$$\hat{H}_{\text{e–light}} = -\frac{e}{m} \sum_{\lambda\lambda' \boldsymbol{k}} \boldsymbol{A}(t) \cdot \boldsymbol{p}_{\boldsymbol{k}}^{\lambda\lambda'} \, \hat{a}_{\lambda \boldsymbol{k}}^{\dagger} \hat{a}_{\lambda' \boldsymbol{k}}. \tag{3.2}$$

To evaluate this Hamiltonian for the case of electrons in graphene, the matrix element $\boldsymbol{p}_{\boldsymbol{k}}^{\lambda\lambda'}$ of the canonical momentum operator $\hat{\boldsymbol{p}} = -i\hbar\nabla$ is calculated using the tight-binding expansion (1.3) in a similar way as the Coulomb matrix elements in the previous chapter. The derivation here follows the same outline as in [15].

$$\begin{aligned} \boldsymbol{p}_{\boldsymbol{k}}^{\lambda\lambda'} &\equiv \int \mathrm{d}\boldsymbol{x} \; \Psi_{\lambda \boldsymbol{k}}^{*}(\boldsymbol{x}) \; \hat{\boldsymbol{p}} \; \Psi_{\lambda' \boldsymbol{k}}(\boldsymbol{x}) \\ &\approx C_{\lambda \boldsymbol{k}}^{A*} C_{\lambda' \boldsymbol{k}}^{B} \sum_{\boldsymbol{b}_n} e^{i\boldsymbol{k}\boldsymbol{b}_n} \underbrace{\int \mathrm{d}\boldsymbol{x} \, \phi(\boldsymbol{x}) \hat{\boldsymbol{p}} \, \phi(\boldsymbol{x} - \boldsymbol{b}_n)}_{\equiv -ip\boldsymbol{b}_n/b} + C_{\lambda \boldsymbol{k}}^{B*} C_{\lambda' \boldsymbol{k}}^{A} \sum_{\boldsymbol{b}_n} e^{-i\boldsymbol{k}\boldsymbol{b}_n} ip\boldsymbol{b}_n/b. \end{aligned} \tag{3.3}$$

We obtain a site-based matrix element, $\langle \text{site} | \hat{\boldsymbol{p}} | \text{site}' \rangle$. It can be seen that the same-site terms give zero, so the lowest-order approximation is to use only the nearest-neighbor transitions, $\langle \text{site} | \hat{\boldsymbol{p}} | \text{site} + \boldsymbol{b}_n \rangle$, $\boldsymbol{b}_n$ being the neighbor vectors (1.2). The integral here, the nearest-neighbor orbital matrix element of the operator $\hat{\boldsymbol{p}}$, can by symmetry be shown to lie along the neighbor vector $\boldsymbol{b}_n$. We write it as proportional to the positive constant $p \equiv \hbar \int \phi(\boldsymbol{x}) \frac{\mathrm{d}}{\mathrm{d}x} \phi(\boldsymbol{x} - b\hat{\boldsymbol{e}}_x) \mathrm{d}\boldsymbol{x}$. The remaining sums are identified as gradients of $g_{\boldsymbol{k}}$ (1.6). Inserting the expressions for the C functions (1.9) we arrive at

$$\begin{aligned} \boldsymbol{p}_{\boldsymbol{k}}^{\text{cc}} &= -\boldsymbol{p}_{\boldsymbol{k}}^{\text{vv}} = -\frac{p}{b} \operatorname{Re}\Big[\frac{g_{\boldsymbol{k}}^{*} \nabla g_{\boldsymbol{k}}}{|g_{\boldsymbol{k}}|}\Big] \\ \boldsymbol{p}_{\boldsymbol{k}}^{\text{cv}} &= -\boldsymbol{p}_{\boldsymbol{k}}^{\text{vc}} = -i\frac{p}{b} \operatorname{Im}\Big[\frac{g_{\boldsymbol{k}}^{*} \nabla g_{\boldsymbol{k}}}{|g_{\boldsymbol{k}}|}\Big] . \end{aligned} \tag{3.4}$$

The real and imaginary parts, and x and y components of the function $g^{*}\nabla g/|g|$ are plotted in figure 3.2. The matrix elements contain the gradient of the neighbor vector phase sum $g_{\boldsymbol{k}}$ (1.6) which is non-varying in the vicinity of the Γ points, so the optical matrix element is zero in that region.

Close to the Dirac points, the optical matrix elements can be approximated as

$$\begin{aligned} \boldsymbol{p}^{\text{cc}}(\boldsymbol{k}) &\approx \; -p\big[\cos\theta_k \, \hat{\boldsymbol{e}}_x + \sin\theta_k \, \hat{\boldsymbol{e}}_y\big] \\ \boldsymbol{p}^{\text{cv}}(\boldsymbol{k}) &\approx \pm ip\big[\sin\theta_k \, \hat{\boldsymbol{e}}_x - \cos\theta_k \, \hat{\boldsymbol{e}}_y\big] \end{aligned} \tag{3.5}$$

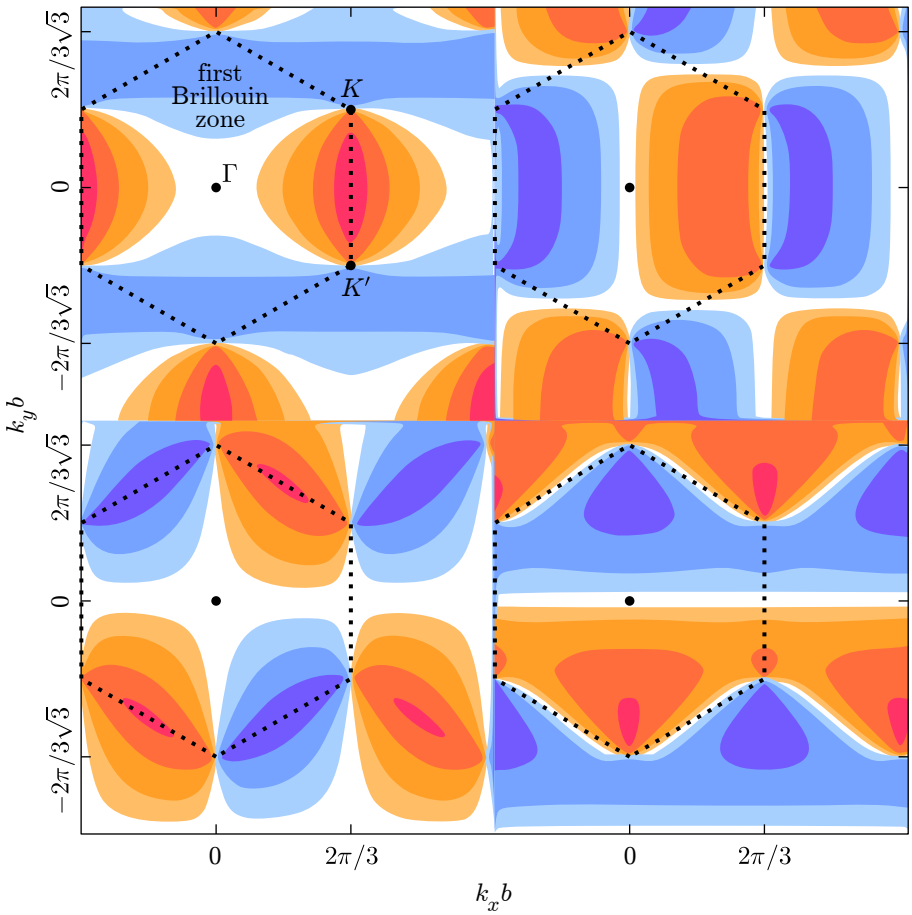

Figure 3.2 Optical matrix elements (3.4) in the band basis. Yellow and red represents positive values, white zero, and blue negative values.

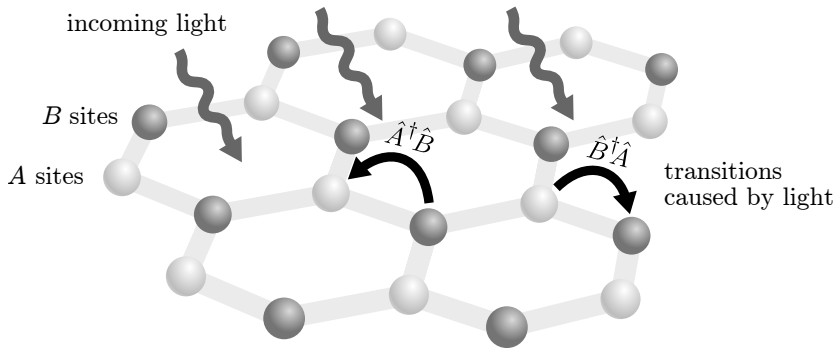

Figure 3.3 Incoming photons absorbed by electrons, causing the electrons to hop between nearest-neighbor sites, as described by the Hamiltonian (3.6).

where the $\pm$ signs correspond to the K^+ and K^- points. It is worth noting that all of these matrix elements are a sine or a cosine of the coordinate angle, that is, they all have a p-like symmetry. Since the bands (1.8) are isotropic (s-like) close to the Dirac points, the light will create p-like excitation in the bands.

3.2 Light–matter interaction in the sublattice basis

Some interesting properties of the light–matter interaction in graphene can be seen more clearly by switching to the sublattice basis (1.10).

$$\hat{H}_{\text{e–light}} = \frac{ep}{m} \sum_{\boldsymbol{k}} \boldsymbol{A}(t) \cdot \left(\nabla g_{\boldsymbol{k}} \; \hat{A}^\dagger_{\boldsymbol{k}} \hat{B}_{\boldsymbol{k}} + \nabla g^*_{\boldsymbol{k}} \; \hat{B}^\dagger_{\boldsymbol{k}} \hat{A}_{\boldsymbol{k}} \right) \tag{3.6}$$

The components of the optical matrix element in the sublattice basis are plotted in figure 3.4. Interestingly, the light interaction is completely off-diagonal in this basis, which means that the light causes electronic transitions only from one sublattice to the other, as shown in figure 3.3. This was also seen in the derivation of the light–matter matrix element (3.3); same-site terms were zero, and the largest contributions were from nearest-neighbor overlaps.

Another interesting point is that circularly polarized light causes transitions from sublattice A to sublattice B at one Dirac point, and back at the other. This is a consequence of the chirality of the optical matrix element $\nabla g_{\boldsymbol{k}}$. A circularly polarized light beam, traveling perpendicularly to the graphene sheet, can be written as $\boldsymbol{A}(t) = (\hat{\boldsymbol{e}}_x \pm i\hat{\boldsymbol{e}}_y)\exp(i\omega t)$ with the $\pm$ signs referring to either circularly polarized direction, at the position of the sheet. The position dependence of the optical matrix element, close to the Dirac points, can be approximated as $(\hat{\boldsymbol{e}}_x \pm i\hat{\boldsymbol{e}}_y)$, see (1.12), where the $\pm$ signs refer to either Dirac

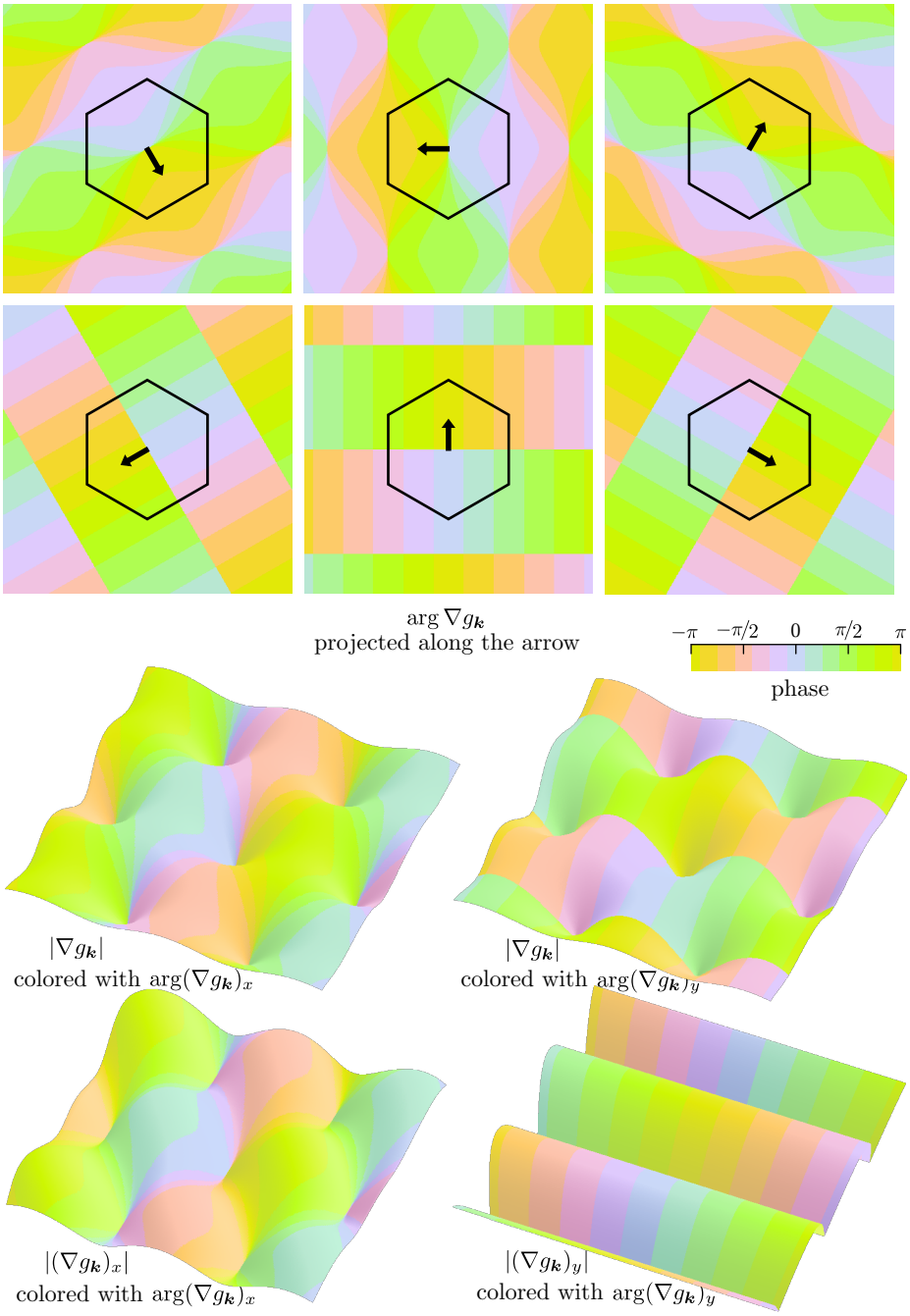

Figure 3.4 Optical matrix element $\nabla g_{\boldsymbol{k}}$ in the sublattice basis (3.6). Upper panels, phase of matrix element projected along vector indicated in figure. Lower panels, phase shown as color on surface given by magnitude of different components of the matrix element.

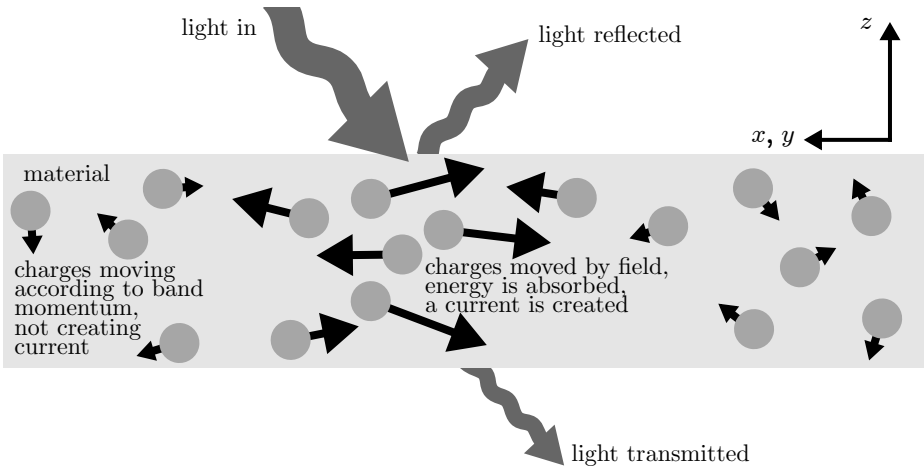

Figure 3.5 Incoming light causing a current in the material.

point. As a consequence, since $(\hat{\boldsymbol{e}}_x + i\hat{\boldsymbol{e}}_y)\cdot(\hat{\boldsymbol{e}}_x - i\hat{\boldsymbol{e}}_y) = 0$, either the first or the second term of the light–matter Hamiltonian (3.6) is always zero at a particular Dirac point, and hence only one type of transition occurs there.

3.3 Calculating the absorption

One of the advantages of using our semiconductor-type many-body theory is the possibility to calculate the response to an external electric field, and obtain estimates for experimentally observable optical features of the system using only low-order approximations.

When light enters the material, it causes the charges in the material to move around. The moving charges constitute a current. If the electric field is weak, the strength of the current is approximately proportional to the strength of the field. The current influences the electric field that is transmitted out of the material, which can be observed. These processes are illustrated in figure 3.5.

Our system is assumed to be in its ground state, and is then excited by a pulse of light $\boldsymbol{A}(t)$. We follow the time development of the excitation until the system has returned to its ground state. In the simplest approximation, the light pulse is considered short and weak. We can consequently use the amplitude of the light as an expansion parameter, and discard all terms which contain high powers of the field amplitude.

The absorption spectrum in graphene can be calculated with an approach similar to that of semiconductor theory, but has to be treated with care, as

large-gap approximations are not valid. The first order of excited current under these weak-light circumstances, i.e. the linear current, is given by

$$\boldsymbol{j} = \left\langle \frac{\delta \hat{H}_{\text{e–light}}}{\delta \boldsymbol{A}} \right\rangle = \frac{e}{m} \sum_{\lambda\lambda' \boldsymbol{k}} \boldsymbol{p}_{\boldsymbol{k}}^{\lambda\lambda'} \langle \hat{a}^\dagger_{\lambda \boldsymbol{k}} \hat{a}_{\lambda' \boldsymbol{k}} \rangle. \tag{3·7}$$

In this model, the current is calculated by solving the dynamics of the expectation values $\langle \hat{a}^\dagger_{\lambda \boldsymbol{k}} \hat{a}_{\lambda' \boldsymbol{k}} \rangle$ under the influence of the electric field. These dynamics will be discussed further in chapter 4. The time evolution of the current is calculated, Fourier transformed to obtain the frequency information, and divided by the incoming electric field. This gives the absorption coefficient

$$\frac{2}{\omega} \frac{\operatorname{Im}\big[\boldsymbol{j}(\omega) \cdot \hat{\boldsymbol{e}}_A\big]}{|\boldsymbol{A}(\omega)|},$$

which relates the outgoing and the incoming electric fields. The quantity we plot is the linear susceptibility $\operatorname{Im}\big[j(\omega)/\omega A(\omega)\big]$.

Any system in its ground state can only absorb energy from the incoming light, and the transmitted light is always weaker than the incident light. The absorption spectrum for such a case is positive. If the system was in an excited state to begin with, however, the incoming light might pick up some energy from the system. The transmitted light would then be stronger, and the absorption spectrum negative for the frequencies involved. This will be relevant in chapter 6, where we discuss the consequences of a strong Coulomb interaction in the gapless band structure.

In a standard semiconductor with a band gap, the linear spectrum typically shows a more or less featureless nonzero absorption above the band edge. If Coulomb interaction is included, the spectrum also shows several strong and sharp excitonic absorption peaks below the band gap. Graphene, being gapless, was an interesting system to apply this technique to — how and where in the spectrum would excitons show up?

Chapter 4

Equations of motion

In the previous two chapters, the single-particle and interaction parts of the electronic system Hamiltonian in graphene were determined. In this chapter, the many-body theory will be put to use for determining the dynamics of the electronic system. Once the Hamiltonian is known, we can in principle find out anything about our system. I will start by defining the basic microscopic quantities, which describe the detailed electronic state of the system. The many-body Hamiltonian is then used to derive equations for the time evolution of these microscopic quantities. In later chapters, these so-called equations of motion will be solved numerically.

The type of approach described here has been used successfully for a great number of applications in the field of semiconductor theory [4, 16]. In semiconductors, the ground state consists of a full valence band and an empty conduction band. An external perturbation, for example light, excites a small and controllable number of electrons to the conduction band. In semiconductor theory, it is therefore useful to define the small conduction band electron population as the dynamical quantity of interest.

In a metal, the same approach is of less use, since any low-temperature ground state is continuously excited by arbitrarily weak perturbations; no band can be said to have a small, or controllable, population. Graphene, in the non-interacting picture of chapter 1, is a gapless system, but would behave mostly like a semiconductor in this respect, since the bands touch only at isolated points in momentum space.

The equations used for semiconductors, however, contain the assumption of a large band gap, which allows certain simplifications to be made. In gapless systems, the absence of these simplifications give the graphene equations of motion some additional structure, as I will discuss in this chapter. A semiconductor

theory-like approach to graphene, similar to the one described here, can be found e.g. in [17].

4.1 Quantities

In the present approach, the main quantities of interest are the single-particle expectation values in the band picture. These quantities are the distribution of electrons in the conduction band $\langle \hat{a}^\dagger_{\mathrm{c}\boldsymbol{k}} \hat{a}_{\mathrm{c}\boldsymbol{k}} \rangle$, the distribution of holes in the valence band $1 - \langle \hat{a}^\dagger_{\mathrm{v}\boldsymbol{k}} \hat{a}_{\mathrm{v}\boldsymbol{k}} \rangle$, and the microscopic interband polarization

$$P_{\boldsymbol{k}} \equiv \langle \hat{a}^\dagger_{\mathrm{v}\boldsymbol{k}} \hat{a}_{\mathrm{c}\boldsymbol{k}} \rangle. \tag{4.1}$$

The excitations we will be considering will always create electrons and holes at the same k values. As a consequence, the distribution of electrons in the conduction band is always equal to the distribution of holes in the valence band. I use the symbol $f_{\boldsymbol{k}}$ to denote this joint electron-and-hole distribution, and I will refer to it simply as the population.

$$f_{\boldsymbol{k}} \equiv \langle \hat{a}^\dagger_{\mathrm{c}\boldsymbol{k}} \hat{a}_{\mathrm{c}\boldsymbol{k}} \rangle = 1 - \langle \hat{a}^\dagger_{\mathrm{v}\boldsymbol{k}} \hat{a}_{\mathrm{v}\boldsymbol{k}} \rangle \tag{4.2}$$

The population $f_{\boldsymbol{k}}$ is a real-valued number between one and zero, measuring the band filling in the material.

4.2 Time evolution from the Hamiltonian

In the Heisenberg picture, the time dependence of any observable is given by the Heisenberg equation of motion

$$i\hbar \frac{\mathrm{d}}{\mathrm{d}t} \hat{O} = \big[\hat{O}, \hat{H}\big].$$

The time evolution of our quantities is obtained by commutating the electron operators through the system Hamiltonian,

$$i\hbar \frac{\mathrm{d}}{\mathrm{d}t} \langle \hat{a}^\dagger_{\boldsymbol{k}} \hat{a}_{\boldsymbol{k}} \rangle = \langle \big[\hat{a}^\dagger_{\boldsymbol{k}} \hat{a}_{\boldsymbol{k}}, \hat{H}\big] \rangle \,.$$

Our quantities are the population (4.2) and the polarization (4.1), and the system Hamiltonian consists of the light–matter Hamiltonian (3.2) and the Coulomb Hamiltonian (2.4). One can expand commutators containing several operators according to the pattern

$$\begin{aligned}\big[\hat{a}^\dagger_{\boldsymbol{k}}\hat{a}_{\boldsymbol{k}}, \hat{a}^\dagger_{\boldsymbol{p}}\hat{a}_{\boldsymbol{p}'}\big] &= \hat{a}^\dagger_{\boldsymbol{k}}\big[\hat{a}_{\boldsymbol{k}}, \hat{a}^\dagger_{\boldsymbol{p}}\hat{a}_{\boldsymbol{p}'}\big] + \big[\hat{a}^\dagger_{\boldsymbol{k}}, \hat{a}^\dagger_{\boldsymbol{p}}\hat{a}_{\boldsymbol{p}'}\big]\hat{a}_{\boldsymbol{k}} \\ &= \hat{a}^\dagger_{\boldsymbol{k}}\big\{\hat{a}_{\boldsymbol{k}}, \hat{a}^\dagger_{\boldsymbol{p}}\big\}\hat{a}_{\boldsymbol{p}'} - \hat{a}^\dagger_{\boldsymbol{p}}\big\{\hat{a}_{\boldsymbol{k}}, \hat{a}^\dagger_{\boldsymbol{p}'}\big\}\hat{a}_{\boldsymbol{k}}\end{aligned}$$

reducing them to anti-commutators containing only one pair of fermion operators. The anti-commutators can be evaluated with the standard fermion anti-commutation rules. Commutating a four-operator Coulomb Hamiltonian with the two-operator expectation values is known to lead to an infinite hierarchy of equations [18]. In the present studies, we will always truncate this hierarchy at the Hartree–Fock, or mean-field level,

$$\langle \hat{a}^\dagger_1 \hat{a}^\dagger_2 \hat{a}_3 \hat{a}_4 \rangle \approx \langle \hat{a}^\dagger_1 \hat{a}_4 \rangle \langle \hat{a}^\dagger_2 \hat{a}_3 \rangle - \langle \hat{a}^\dagger_1 \hat{a}_3 \rangle \langle \hat{a}^\dagger_2 \hat{a}_4 \rangle \,. \tag{4.3}$$

4.3 Hartree–Fock equations of motion for the population and the polarization

Evaluating the commutations and performing the truncation leads to equations of motion for the population $f_{\boldsymbol{k}}$ and the polarization $P_{\boldsymbol{k}}$,

$$\begin{aligned}\hbar\frac{\mathrm{d}}{\mathrm{d}t} f_{\boldsymbol{k}} &= -2\,\mathrm{Im}\big[P^*_{\boldsymbol{k}}\Omega_{\boldsymbol{k}}\big] \\ i\hbar\frac{\mathrm{d}}{\mathrm{d}t} P_{\boldsymbol{k}} &= 2\Sigma_{\boldsymbol{k}} P_{\boldsymbol{k}} - \big(1 - 2f_{\boldsymbol{k}}\big)\Omega_{\boldsymbol{k}}.\end{aligned} \tag{4.4}$$

In the expressions above, we have used an internal field $\Omega_{\boldsymbol{k}}$ and a renormalized energy $\Sigma_{\boldsymbol{k}}$ defined as

$$\begin{aligned}\Sigma_{\boldsymbol{k}} &\equiv E_{\boldsymbol{k}} - \sum_{\boldsymbol{k}'}\big[(V^+_{\boldsymbol{k}\boldsymbol{k}'} - V^-_{\boldsymbol{k}\boldsymbol{k}'})f_{\boldsymbol{k}'} + V^A_{\boldsymbol{k}\boldsymbol{k}'}(P_{\boldsymbol{k}'} - P^*_{\boldsymbol{k}'})\big] - \frac{e}{m}\boldsymbol{A}\cdot\boldsymbol{p}^{\mathrm{cc}}_{\boldsymbol{k}} \\ \Omega_{\boldsymbol{k}} &\equiv \sum_{\boldsymbol{k}'}\big[V^+_{\boldsymbol{k}\boldsymbol{k}'}P_{\boldsymbol{k}'} + V^-_{\boldsymbol{k}\boldsymbol{k}'}P^*_{\boldsymbol{k}'} + 2V^A_{\boldsymbol{k}\boldsymbol{k}'}f_{\boldsymbol{k}'}\big] + \frac{e}{m}\boldsymbol{A}\cdot\boldsymbol{p}^{\mathrm{cv}}_{\boldsymbol{k}}.\end{aligned} \tag{4.5}$$

Here we have used the dispersion $E_{\boldsymbol{k}}$ (1.8) the optical matrix elements $\boldsymbol{p}_{\boldsymbol{k}}$ (3.4) and the Coulomb matrix elements (2.5) in the linear approxiamtion. The renormalized energy $\Sigma_{\boldsymbol{k}}$ is a real-valued quantity, since the Auger Coulomb matrix element $V^A_{\boldsymbol{k}\boldsymbol{k}'}$ is purely imaginary. The internal field $\Omega_{\boldsymbol{k}}$ is complex-valued.

The equations have the same outward form as the familiar Semiconductor Bloch Equations (SBEs) for a standard semiconductor [4, 16], but with several important differences. Most notably, the internal field $\Omega_{\boldsymbol{k}}$ depends not only on the polarization $P_{\boldsymbol{k}}$ (as is the case for semiconductors) but also on its conjugate $P^*_{\boldsymbol{k}}$, as well as on the population $f_{\boldsymbol{k}}$. The presence of the populations in the internal field is due to the Auger parts V^A of the Coulomb interaction.

The Auger terms are in principle present also in the SBEs, but they are commonly neglected since they are strongly off-resonant and therefore weak in a gapped system. In graphene with its zero-gap band structure, the Auger terms are as resonant as the common terms. The internal field $\Omega_{\boldsymbol{k}}$ additionally contains a contribution from the external electric field $\boldsymbol{A}$. This term is due to the interband part of the light–matter interaction, which is present also in the SBEs.

The renormalized energy $\Sigma_{\boldsymbol{k}}$ is generalized in a similar fashion. It has familiar contributions, proportional to the population $f_{\boldsymbol{k}}$, as well as Auger terms. The Auger terms in $\Sigma_{\boldsymbol{k}}$ are proportional to $P_{\boldsymbol{k}}$ and its conjugate, and again, they are not present in $\Sigma_{\boldsymbol{k}}$ in the SBEs.

The renormalized energy $\Sigma_{\boldsymbol{k}}$ contains a contribution from the external field $\boldsymbol{A}$ as well; this in its turn comes from the intraband part of the light–matter interaction. This intraband term in $\Sigma_{\boldsymbol{k}}$ is sometimes included in the SBEs, provided that the exciting light is in a frequency range low enough to make these contributions resonant. In graphene, inter- and intraband contributions are equally important, due again to the zero band gap.

4.4 Renormalization in the equations of motion

When deriving the equation of motion for $P_{\boldsymbol{k}}$, terms appear that group together with the definition of $\Sigma_{\boldsymbol{k}}$, and are non-vanishing even when the valence band is full and the conduction band is empty, $f_{\boldsymbol{k}} = P_{\boldsymbol{k}} = 0$. This is the so-called static renormalization of the bands, which arises due to Coulomb interactions from the valence band electrons.

$$\Sigma_{\boldsymbol{k}} = \underbrace{E^0_{\boldsymbol{k}} - \sum_{\boldsymbol{k}'} (V^+_{\boldsymbol{k}\boldsymbol{k}'} - V^-_{\boldsymbol{k}\boldsymbol{k}'})/2}_{\equiv E_{\boldsymbol{k}}} + \ldots f_{\boldsymbol{k}'} + \ldots P_{\boldsymbol{k}'} \tag{4.6}$$

The static renormalization is taken as being included in the dispersion $E_{\boldsymbol{k}}$, modifying an unknown "bare" dispersion $E^0_{\boldsymbol{k}}$. Close to the Dirac points, the static renormalization is a linear function of $\boldsymbol{k}$. As the dispersion $E_{\boldsymbol{k}}$ is also linear, it is reasonable to take the renormalization as a modifier to a bare Fermi velocity. From an experimental point of view, the bare Fermi velocity is not observable. If the dispersion is measured in an experiment, all renormalization effects are included. The study of renormalization and its effects on parameters and natural constants, in graphene and otherwise, is a wide theoretical field in itself [19–24].

4.5 The coupling strength in the Coulomb sums

As shown in chapter 2, the strength of the Coulomb interaction in graphene is determined by a coupling constant α, which emerges when writing the Hamiltonian in terms of unitless variables. This coupling strength appears in a similar fashion in the equations of motion as well.

The equations of motion (4.4) have the dimension of energy, as that is the dimension of $\Sigma_{\boldsymbol{k}}$ and $\Omega_{\boldsymbol{k}}$. To cast the equations of motion into a dimensionless form, we divide them by the energy parameter $\hbar v_F/d$. Inserting the expression for the Coulomb potential (2.6) and taking the limit of an infinite system in real space $\sum_{\boldsymbol{k}} \to \mathcal{A}\int \mathrm{d}\boldsymbol{k}/4\pi^2$, the Coulomb terms in the equations of motion acquire the following form:

$$\begin{aligned}\frac{\sum_{\boldsymbol{k}'} W(\boldsymbol{k}-\boldsymbol{k}')[\cdots]}{\hbar v_F/d} &= \frac{e^2 d}{8\pi^2\epsilon\epsilon_0\hbar v_F}\int \mathrm{d}\boldsymbol{k}' \frac{F(|\boldsymbol{k}-\boldsymbol{k}'|d)[\cdots]}{|\boldsymbol{k}-\boldsymbol{k}'|} \\ &= \frac{\alpha}{2\pi}\int \mathrm{d}\boldsymbol{\eta}' \frac{F(|\boldsymbol{\eta}-\boldsymbol{\eta}'|)[\cdots]}{|\boldsymbol{\eta}-\boldsymbol{\eta}'|} \quad \text{with } \boldsymbol{\eta} = \boldsymbol{k}d \end{aligned} \tag{4.7}$$

and the only parameter left in the equations of motion is the coupling strength α. As will be shown in later chapters, the behavior of the equations of motion depends critically on the value of the coupling strength.

4.6 Electronic screening and the coupling strength

Truncating the hierarchy of expectation values when deriving the equations of motion entails neglecting certain effects. One of those is electronic screening, which is expected to play an important role in graphene [24–31]. Screening is the phenomenon in which an electron cloud reacts to an electric field, by reconfiguring itself to weaken the field. This includes the fields created by the electrons themselves. In effect, the screening makes the Coulomb interaction weaker.

In an electronic system with a band gap, there is no screening in the ground state, since the electrons in a full band cannot move in response to an electric field. The reason for having any screening at all in an unexcited graphene system is that the electrons in the valence band, close to the Dirac points, can move to the conduction band while spending an infinitesimal amount of energy, and so screening occurs somewhat like in a metal.

Screening is a complicated many-body effect, involving all orders of the hierarchy of expectation values in the equations of motion. There are, however, ways to approximate these effects, and to include the screening as a calculable

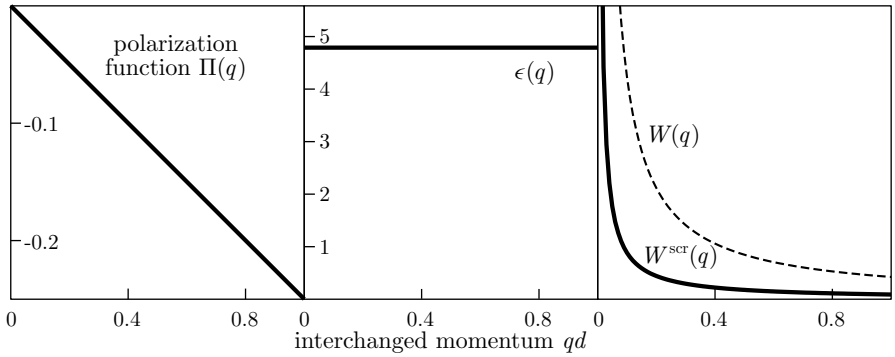

Figure 4.1 The quantities relevant for the screening in the unpopulated tight-binding ground state in graphene. A linear polarization function (4.10) gives an approximately constant dielectric function (4.9) which weakens the Coulomb interaction (4.8) by a constant factor.

weakening of the Coulomb potential in the truncated equations of motion. The screening effects are taken into account by using a screened Coulomb potential

$$W^{\mathrm{scr}}(q) = \frac{W(\boldsymbol{q})}{\epsilon(\boldsymbol{q})} \tag{4.8}$$

which is related to the unscreened potential $W(\boldsymbol{q})$ (2.6) through a dielectric screening function $\epsilon(\boldsymbol{q}) \geq 1$, weakening the effective Coulomb potential. The dielectric screening function can be stated in terms of a polarization function $\Pi(\boldsymbol{q})$ related to the dielectric screening via

$$\epsilon(\boldsymbol{q}) = 1 - W(\boldsymbol{q})\Pi(\boldsymbol{q}). \tag{4.9}$$

For an unpopulated state (the tight-binding ground state with $f_{\boldsymbol{k}} = P_{\boldsymbol{k}} = 0$) close to the Dirac points where the dispersion is linear, the polarization function is evaluated as

$$\Pi(\boldsymbol{q}) = -4 \sum_{\boldsymbol{k}} \frac{1 - \cos(\theta_{\boldsymbol{k}} - \theta_{\boldsymbol{k}-\boldsymbol{q}})}{E_{\boldsymbol{k}-\boldsymbol{q}} + E_{\boldsymbol{k}}} \,. \tag{4.10}$$

With the linear dispersion $E_{\boldsymbol{k}}$, this ground state polarization function is isotropic and proportional to q, as plotted on the left in figure 4.1. With a linear polarization function, the dielectric function (4.9) is approximately a constant, since the q dependence of the bare Coulomb potential is $F(qd)/q$, and the form function gives only a slow additional drop-off for q.

A constant dielectric screening function can be incorporated in the background dielectric constant, which in turn forms a part of the coupling strength α. These standard screening results give an effective background dielectric constant of approximately 4.8 for the unexcited system. For the coupling strength α, this gives a value of approximately 0.5, significantly lower than the unscreened value of 2.4. A full treatment of the screening is deferred to chapter 10. Until then, the coupling strength is taken simply as an input parameter.

Chapter 5

Inhomogeneous excitation and wavepacket dynamics

In the previous chapters, the electric field was assumed to be constant over the whole material. For example, the equations of motion of chapter 4 contain the assumption that the distribution of electrons is uniform in the material. In this chapter, I discuss a situation where the light intensity varies in space, and hence excites an electron distribution which also varies in space. One can follow the spatial movement of these electrons by solving a set of generalized equations of motion.

Analyzing the movement of the electrons gives information about the state the electrons are in. A localized packet of electrons, for example, moves according to the momentum contents of that particular wavepacket. In particular, electrons and holes in a bound state, called an exciton, move differently from unbound electrons and holes. These two types of excitation (bound and unbound pairs) move in manners that can be clearly distinguished by solving the inhomogeneous equations of motion.

Equations of motion for such locally excited electrons have been set up and solved for semiconductors in [32]. In Paper I, we set up similar equations of motion for electrons in a carbon nanotube, using the graphene many-body theory outlined in the first three chapters of this thesis.

In Paper I, the carbon nanotube is first exposed to a light pulse. The light is chosen to have an unequal strength at different positions along the tube, in order to make the motion of the created excitations visible. After the light pulse is turned off, the motion of the excitations is studied, by numerically solving our spatially inhomogeneous graphene equations of motion.

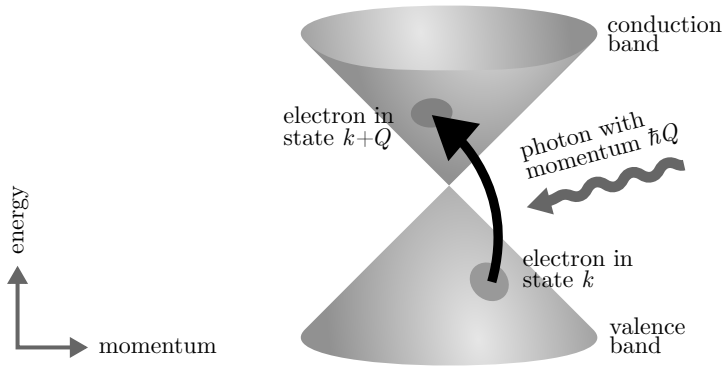

Figure 5.1 Light causing an electronic transition in graphene.

5.1 Using a spatially varying light field

To derive spatially inhomogeneous equations of motion, we need a spatially inhomogeneous model of the light, in the form of a Hamiltonian. The graphene light–matter Hamiltonian in chapter 3 was derived under the assumption that the light field vector potential $\boldsymbol{A}(t)$ is independent of the spatial coordinate in the graphene plane. In this chapter, we will instead be using a light field $\boldsymbol{A}(\boldsymbol{x}, t)$ that varies slowly over the material, on a length scale of at least several unit cells.

To include the spatial dependence of the light field in the light–matter Hamiltonian, one needs to account for it when performing the integration over space, at the stage of (3.1). Using the assumption of a field varying only on the scale of several unit cells of the material, basically setting $\boldsymbol{A}(\boldsymbol{x}, t) \approx \boldsymbol{A}(\boldsymbol{R}, t)$, one is able to separate the length scales involved in the spatial integration into a sum over unit cells and an integral over a single unit cell.

Performing a derivation similar to the one in chapter 3, except for maintaining the slow spatial variance in $\boldsymbol{A}(\boldsymbol{x}, t)$, we arrive at the Hamiltonian for electrons interacting with an inhomogeneous light,

$$\hat{H}_{\text{e–light}} = -\frac{e}{m} \sum_{\lambda\lambda' \boldsymbol{k}\boldsymbol{k}'} \boldsymbol{p}^{\lambda\lambda'}_{\boldsymbol{k}\boldsymbol{k}'} \cdot \boldsymbol{A}(\boldsymbol{k} - \boldsymbol{k}', t)\, \hat{a}^\dagger_{\lambda \boldsymbol{k}} \hat{a}_{\lambda' \boldsymbol{k}'} \tag{5.1}$$

with the momentum matrix elements

$$\begin{aligned} \boldsymbol{p}^{\text{cv}}_{\boldsymbol{k}\boldsymbol{k}'} &= \frac{p}{2b} \left(\frac{g_{\boldsymbol{k}} \nabla g^*_{\boldsymbol{k}}}{|g_{\boldsymbol{k}}|} - \frac{g^*_{\boldsymbol{k}'} \nabla g_{\boldsymbol{k}'}}{|g_{\boldsymbol{k}'}|} \right) \\ \boldsymbol{p}^{\text{cc}}_{\boldsymbol{k}\boldsymbol{k}'} &= -\frac{p}{2b} \left(\frac{g_{\boldsymbol{k}} \nabla g^*_{\boldsymbol{k}}}{|g_{\boldsymbol{k}}|} + \frac{g^*_{\boldsymbol{k}'} \nabla g_{\boldsymbol{k}'}}{|g_{\boldsymbol{k}'}|} \right) . \end{aligned}$$

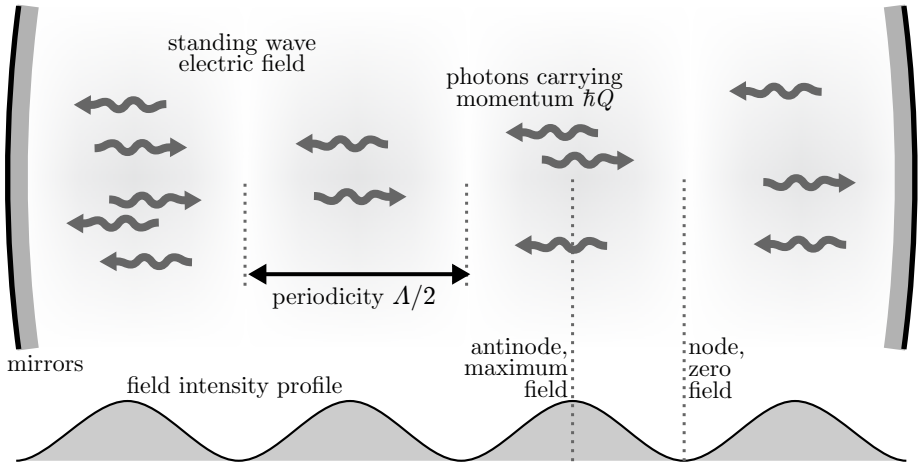

Figure 5.2 A standing wave, as an example of an inhomogeneous light field.

In this Hamiltonian, like before, $\lambda\lambda'$ are indices for the conduction and valence bands, and $\boldsymbol{k}$ is the in-plane momentum of the electrons in the bands. The light field $\boldsymbol{A}(\boldsymbol{k}-\boldsymbol{k}',t)$ appears in a Fourier transformed form, with $\boldsymbol{A}(\boldsymbol{k},t) = \sum_{\boldsymbol{R}} e^{i\boldsymbol{k}\boldsymbol{R}}\boldsymbol{A}(\boldsymbol{R},t)$. The field profile in momentum space represents the photon momentum contents of the light field. The electron created and the electron annihilated by the light Hamiltonian differ in momenta by $\boldsymbol{k}-\boldsymbol{k}'$. This difference is the momentum $\boldsymbol{Q}$ of the photon absorbed (or created) in the process, as shown in figure 5.1. The electron absorbs a photon, and the photon energy and momentum is transferred to the electron. In a spatially homogeneous situation, the photon momentum is usually without consequence and hence neglected.

A simple example of a spatially varying field is a one-dimensional standing wave, shown in figure 5.2. This is the field we are using in Paper I to create a spatially varying distribution of electrons along a carbon nanotube. A standing wave is formed when a simple single-frequency cosine wave is reflected and re-reflected between two mirrors,

$$\boldsymbol{A}(\boldsymbol{x},t) = \boldsymbol{A}_0(e^{iQx} + e^{-iQx})e^{i\omega t} + \text{c.c.}$$

The photons all have the same frequency and since they travel in both directions between the mirrors, they have the momenta $\hbar Q$ and $-\hbar Q$ along the standing wave. The light intensity profile is a simple periodic function $\cos^2(Qx)$ with a periodicity of π/Q, half the photon wavelength.

5.2 Inhomogeneous excitation

When the system is excited with a light with a spatial profile, the excitations created in the material are also position-dependent. Initially, the excitation has the same spatial profile as the field that created it. To solve the dynamics from that point on, one needs equations of motion for position-dependent electron densities. What we are interested in is the real-space density of electrons, which is given by the expectation value $\langle \hat{\psi}^\dagger(\boldsymbol{x})\, \hat{\psi}(\boldsymbol{x})\rangle$. In order to apply our graphene many-body theory, we need to relate this real-space expectation value to momentum space quantities. To that end, the field operators $\hat{\psi}(\boldsymbol{x})$ are expanded in a momentum basis, using the graphene tight-binding expansion (1.3). Further, we will assume that the spatial variance of the electronic density is slow, on the scale of several unit cells of the material. The same assumption was made with the slowly-varying light profile in the previous section. The real-space electronic density becomes

$$\langle \hat{\psi}(\boldsymbol{x})^\dagger \hat{\psi}(\boldsymbol{x})\rangle = \underbrace{\frac{1}{N}\sum_{\boldsymbol{R}} |\phi(\boldsymbol{x}-\boldsymbol{R})|^2}_{\text{density within unit cell}} \underbrace{\sum_{\lambda\lambda' \boldsymbol{k}\boldsymbol{k}'} e^{-i(\boldsymbol{k}-\boldsymbol{k}')\boldsymbol{R}} \langle \hat{a}^\dagger_{\lambda\boldsymbol{k}} \hat{a}_{\lambda'\boldsymbol{k}'}\rangle}_{\text{envelope } \rho(\boldsymbol{R}) \approx \rho(\boldsymbol{x}_\parallel)} . \tag{5.2}$$

One finds the familiar separation of length scales; the total electron density is a product of the three-dimensional density of electrons within a unit cell, and a two-dimensional envelope density $\rho(\boldsymbol{x}_\parallel)$. The unit cell density is a simple repeating function over the lattice, and the envelope part depends only on the large-scale in-plane position $\boldsymbol{x}_\parallel$. In this chapter, we will be using the envelope part only.

In the sums over bands in (5.2) filled bands do not contribute, as the filled-band terms add up to zero under their $\boldsymbol{k}$ sums. Hence the envelope density contains only contributions from non-filled bands, in our case the excited electron and hole densities in the conduction and valence bands. These populations in non-filled bands are the only ones free to move and have the possibility of forming a spatially varying envelope.

For the length-scale separated density (5.2) one can see that in order to have non-constant envelope function $\rho(\boldsymbol{x}_\parallel)$, one needs a two-indexed form of the microscopic quantities $\langle \hat{a}^\dagger_{\boldsymbol{k}} \hat{a}_{\boldsymbol{k}'}\rangle$. For the homogeneous system discussed in the previous chapter, only one momentum index was needed. For our present studies, where one valence and one conduction band are considered, the relevant inhomogeneous quantities are

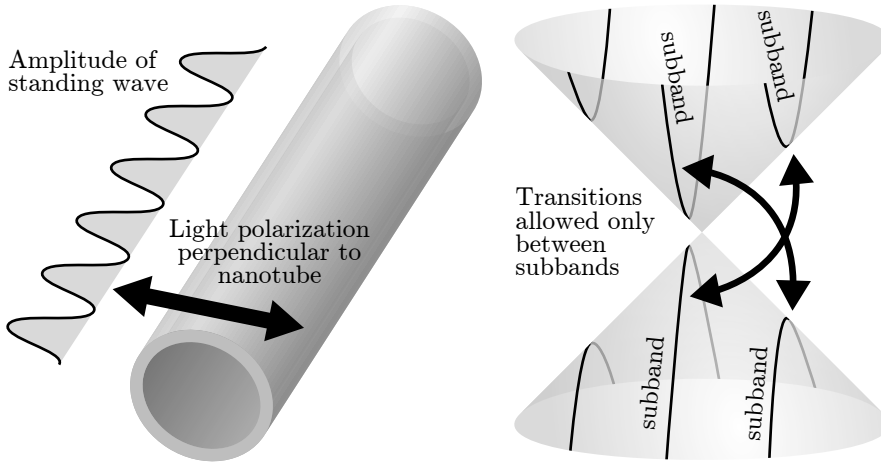

Figure 5.3 A carbon nanotube in a standing wave light field. The tube axis is perpendicular to the light polarization, and as a consequence, the light causes transitions between subbands in momentum space.

$$\begin{aligned} \text{electron population} \quad & f^{\mathrm{e}}_{\boldsymbol{k}\boldsymbol{k}'} \equiv \langle \hat{a}^\dagger_{\mathrm{c}\boldsymbol{k}} \hat{a}_{\mathrm{c}\boldsymbol{k}'} \rangle \,, \\ \text{hole population} \quad & f^{\mathrm{h}}_{\boldsymbol{k}\boldsymbol{k}'} \equiv \delta_{\boldsymbol{k}\boldsymbol{k}'} - \langle \hat{a}^\dagger_{\mathrm{v}\boldsymbol{k}} \hat{a}_{\mathrm{v}\boldsymbol{k}'} \rangle \,, \text{ and} \\ \text{microscopic polarization} \quad & P_{\boldsymbol{k}\boldsymbol{k}'} \equiv \langle \hat{a}^\dagger_{\mathrm{v}\boldsymbol{k}} \hat{a}_{\mathrm{c}\boldsymbol{k}'} \rangle \,. \end{aligned} \tag{5.3}$$

5.3 Inhomogeneous excitation of a semiconducting carbon nanotube

To put our theory for spatially variant excitation to use in graphene, it is convenient to use a lower dimensional system, as the additional momentum variable adds a degree of freedom. A carbon nanotube is therefore a useful application.

Unlike flat graphene with its semimetal characteristics, certain types of carbon nanotubes have large band gaps, making them semiconductors, as was discussed in section 1.7. If the excitation with light is chosen to activate transitions near the band gap, only a limited number of subbands will be activated. In such situations, carbon nanotubes can be conveniently modeled as one-dimensional semiconductors. Exciting a carbon nanotube with a spatially variant light therefore provides an opportunity use many-body theory of graphene to study movements of excitations.

In Paper I, this spatially inhomogeneous field is a standing wave, as was discussed in section 5.1. We chose to have the standing wave along the tube, in order for the light momentum to interact with the continuous (along-tube) com-

ponent of the electron momentum. As a consequence, the light field is polarized in a direction perpendicular to the carbon nanotube axis. In a situation with a perpendicular polarization, the light-induced transitions are between states with subband indices differing by one, as explained in Paper I.

For an unexcited system, the energetically lowest allowed transition is therefore from the valence subband closest to the K point to the conduction subband second-closest to the K point, in the manner illustrated in figure 5.3. Also, at the same energetical level vice versa; from the valence subband second-closest to the K point to the conduction subband closest to the K point. We label these subbands with μ closest to the K point, and $\mu + 1$ for the second closest. The transitions driven by the light are thereby (v, μ) $\leftrightarrow$ (c, $\mu+1$) and (v, $\mu+1$) $\leftrightarrow$ (c, μ), independently and with equal strength. In the numerical study of Paper I, it was therefore possible to limit to studying the dynamics of these two subbands, μ and $\mu + 1$.

The presence of a band gap in semiconducting carbon nanotubes provides us with a system in which excitons appear, like they do in a standard semiconductor [4]. By using different frequency ranges for the light that provides the initial excitation of the system, we can choose which kind of excitation will be present. When the frequency of the light is above the band gap, the light will excite unbound electrons and holes. On the other hand, if the system is excited with frequencies below the band gap, the light will create bound electron–hole pairs, that is, excitons.

These two types of excitation exist in semiconducting carbon nanotubes, as well as in standard semiconductors. Their dynamics in a semiconductor quantum well system is studied in [32]. Based on that study and on general knowledge of bound systems, the two different types of excitation are expected to show distinctly different types of behavior as the system evolves in time. We use our approach, with a spatially varying light, to create a setup where the dynamics of both types of excitation can be observed.

5.4 Equations of motion for inhomogeneous electron densities

In order to calculate the dynamics of our spatially resolved system, we need spatially resolved equations of motion. To this end, we set up equations of motion for the inhomogeneous quantities (5.3). The equations of motion are derived in the same way as in chapter 4, apart from the quantities now having two independent momentum indices, $\boldsymbol{k}$ and $\boldsymbol{k}'$.

The time derivative of each quantity is obtained through commutation with the system Hamiltonian. Like in (4.3) we then factorize the four-operator expectation values into the possible combinations of two-operator expectation values, which closes our set of equations. The factorization of four-operator expectation values is valid only under the assumption that the excitation is small, which is true for cases where the light pulse is weak and short enough. This kind of inhomogeneous time dynamics is also set up and discussed in [32] and [33] for a typical semiconductor system.

As Hamiltonian we use the tight-binding single-particle Hamiltonian $\hat{H}_0$ (1.11) and the Coulomb interaction Hamiltonian $\hat{H}_{\text{coul}}$ (2.4). For the interaction with light, we use the spatially resolved $\hat{H}_{\text{e–light}}$ (5.1). We are writing the quantities in a matrix form, with $^{\mathsf{H}}$ denoting a Hermitian conjugate of the matrix, $P^{\mathsf{H}}(\boldsymbol{k},\boldsymbol{k}') \equiv P^*_{\boldsymbol{k}',\boldsymbol{k}}$. The equations of motion for the inhomogeneous quantities (5.3) can be written as

$$\begin{aligned}
i\hbar\frac{\mathrm{d}}{\mathrm{d}t}f^{\mathrm{e}} &= f^{\mathrm{e}}\Sigma^{\mathrm{e}\mathsf{H}} - \Sigma^{\mathrm{e}}f^{\mathrm{e}} + \Omega^{\mathsf{H}}P - P^{\mathsf{H}}\Omega \\
i\hbar\frac{\mathrm{d}}{\mathrm{d}t}f^{\mathrm{h}} &= \Sigma^{\mathrm{v}}f^{\mathrm{h}} - f^{\mathrm{h}}\Sigma^{\mathrm{v}\mathsf{H}} + P\Omega^{\mathsf{H}} - \Omega P^{\mathsf{H}} \\
i\hbar\frac{\mathrm{d}}{\mathrm{d}t}P &= \Sigma^{\mathrm{v}}P - P\Sigma^{\mathrm{e}\mathsf{H}} - (\mathbb{1}-f^{\mathrm{h}})\Omega + \Omega f^{\mathrm{e}}\,.
\end{aligned} \tag{5.4}$$

We are here also using the two-indexed generalizations of the renormalized energy $\Sigma_{\boldsymbol{k}}$ and internal field $\Omega_{\boldsymbol{k}}$ (4.5). The matrix nature of the dynamic quantities (5.3) modifies the equations of motion, compared to the spatially homogeneous equations of motion. Specifically, there is one more sum in each Coulomb term. Every such sum here takes the form of a matrix multiplication.

In anticipation of the band gap in a semiconducting carbon nanotube, we will be using the standard large-gap approximations discussed in section 4.3. Hence, we will here include only the terms which contribute significantly in that situation, and not the full graphene contributions. It is possible to extend these definitions to be valid for graphene in general, too, by lifting the assumption of a large band gap, and consequently including the V^A and V^- type terms in the Coulomb interaction as well as the intraband terms in the light–matter interaction. Under these assumptions, the expressions for the renormalized energy and the internal field are

$$\Sigma^{\mathrm{c}}_{\boldsymbol{k}\boldsymbol{k}'} \equiv E_{\mathrm{c}\boldsymbol{k}}\delta_{\boldsymbol{k}\boldsymbol{k}'} - \sum_{\boldsymbol{q}\neq 0} V^{+}_{\boldsymbol{k}+\boldsymbol{q},\boldsymbol{k}';\boldsymbol{q}}\; f^{\mathrm{e}}_{\boldsymbol{k}+\boldsymbol{q},\boldsymbol{k}'+\boldsymbol{q}} \tag{5.5}$$

$$\Sigma^{\mathrm{v}}_{\boldsymbol{k}\boldsymbol{k}'} \equiv \tilde{E}_{\mathrm{v}\boldsymbol{k}}\delta_{\boldsymbol{k}\boldsymbol{k}'} + \sum_{\boldsymbol{q}\neq 0} V^{+}_{\boldsymbol{k}+\boldsymbol{q},\boldsymbol{k}',\boldsymbol{q}}\ f^{\mathrm{h}}_{\boldsymbol{k}+\boldsymbol{q},\boldsymbol{k}'+\boldsymbol{q}}\,;\ \tilde{E}_{\mathrm{v}\boldsymbol{k}} = E_{\mathrm{v}\boldsymbol{k}} - \sum_{\boldsymbol{q}\neq 0} V^{+}_{\boldsymbol{k}+\boldsymbol{q},\boldsymbol{k},\boldsymbol{q}} \quad (5.6)$$

$$\Omega_{\boldsymbol{k}\boldsymbol{k}'} \equiv \frac{e}{m}\boldsymbol{p}^{\mathrm{cv}}_{\boldsymbol{k}'\boldsymbol{k}}\cdot\boldsymbol{A}(\boldsymbol{k}'-\boldsymbol{k},t) + \sum_{\boldsymbol{q}\neq 0} V^{+}_{\boldsymbol{k}+\boldsymbol{q},\boldsymbol{k}',\boldsymbol{q}}\ P_{\boldsymbol{k}+\boldsymbol{q},\boldsymbol{k}'+\boldsymbol{q}}\,. \quad (5.7)$$

In the renormalized energy for the valence band $\Sigma^{\mathrm{v}}_{\boldsymbol{k}\boldsymbol{k}'}$ (5.6) we are using a renormalization for the single particle band $\tilde{E}^{\mathrm{v}}_{\boldsymbol{k}}$. Nominally, this Coulomb correction is due the influence of the electrons in the full valence band. As explained in Paper I, this is a somewhat simplistic way of dealing with the binding energy of the exciton exceeding the band gap. For the present task of studying the excitation dynamics, however, using this simple approach makes no qualitative difference. As will be seen in the next chapter, the situation gets more complicated in case one wants a more accurate description of the Coulomb effects on the band structure.

5.5 Wavepacket dynamics in a semiconducting carbon nanotube

To solve the equations of motion, we set the system to an initial state and use time-stepping algorithms to obtain numerical solutions of the time evolution of the system. The initial state is the unexcited ground state of the system, that is, the valence band is full and the conduction band is empty. In terms of our quantities, this is to say that $f^{\mathrm{e}}_{\boldsymbol{k}\boldsymbol{k}'}$ $f^{\mathrm{h}}_{\boldsymbol{k}\boldsymbol{k}'}$ and $P_{\boldsymbol{k}\boldsymbol{k}'}$ start at zero.

The system is then excited with light, and electrons start transitioning from the valence band to the conduction band. Under the influence of the light, the polarization P becomes nonzero due to the source term in (5.4) which in turn creates nonzero f^{e} and f^{h}. The light pulse is kept short enough not to start filling the bands (which would invalidate our approximations) but long enough to have a narrow enough frequency profile. The narrow frequency range is useful for creating excitation at specific transition energies, which gives us the possibility to study how the dynamics depend on the excitation energy.

In the numerical analysis in Paper I, a carbon nanotube is exposed to a light field in the form of a standing wave. The standing wave creates excitation at its antinodes, so the three quantities are initially nonzero at periodic intervals over the length of the carbon nanotube. When the light is turned off, no more excitation is created, and the wavepackets at the antinodes are allowed to spread out in space.

The excitation in the carbon nanotube consists of (valence band) electrons and (conduction band) holes. This excitation can be of two different types; unbound electron–hole pairs, and electron–hole pairs forming bound states (excitons).

When the excitation is of the first type, unbound electrons and holes, the wavepackets will move linearly away from the point in space where they were created. They move with a velocity corresponding to the momentum k at which they were created, and with a mass given by the band curvature at that point. One can witness the phenomenon shown in Paper I; each initial wavepacket splitting up in two parts, and criss-crossing with packets from other parts of the nanotube before slowly dissipating away.

An exciton, on the other hand, moves with the center-of-mass momentum of the created electron–hole pair. Hence, their center-of-mass momentum is the photon momentum Q, which is typically much smaller than the band momenta of the electron and the hole. Consequently, the exciton moves much slower than the unbound electron and hole.

It is also possible to turn off the boundness of the electron–hole pairs by killing the polarization matrix P with a dephasing term in its equation of motion. When the polarization dies away, the electron and hole are freed, and the initially almost immobile excitonic wavepacket spreads out as it gradually is converted to free particles. In the figures presented in Paper I, the excitonic and free-electron movement can be clearly distinguished. From the data, it is clear that excitonic wavepackets exist in gapped graphene systems, as well as in standard semiconductors, and that they behave in fundamentally the same way.

Chapter 6

The Wannier equation and the onset of a strong-coupling phase

In chapter 1, the tight-binding band structure in graphene was introduced. The tight-binding derivation is done without accounting for the Coulomb interaction between the electrons themselves. Close to the Dirac points, however, this assumption becomes somewhat hazy.

Starting from the tight-binding ground state of the system, an electron in the valence band could transition to the conduction band. This transition would require a very small amount of energy, if the electron is close to the Dirac point. This electron could form a bound state with the hole it leaves behind. If the binding energy of this electron–hole pair is larger than the energy that was required to induce the transition, the state with an electron–hole pair has in fact a lower energy than the state we started with. This in turn would imply that the tight-binding ground state is not the same as the true many-body ground state of the electronic system.

A systematic way for testing under which conditions this pair-forming occurs is the subject of Paper II. In this chapter, I present an overview of the techniques used there and the results obtained. The main idea is to set up an equation describing the binding energy of an electron–hole pair in the tight-binding bands. This equation is the Wannier equation, familiar from semiconductor theory [4]. Using various other methods, the criticality of the two-body problem in graphene has been studied extensively in the literature [34–43].

6.1 The Wannier equation in graphene

Physically, an exciton is an electrically bound electron–hole pair. Mathematically, an exciton appears as an eigenstate of the microscopic polarization $P_{\boldsymbol{k}}$

(4.1). In order to look for eigenstates of the polarization, one takes a Fourier transform from time to frequency of the equation of motion for $P_{\boldsymbol{k}}$ (4.4) and arrives at a linear eigenvalue problem. This is the Wannier equation. In our present case, we set the populations $f_{\boldsymbol{k}}$ to zero, since the topic is the potential instability of the system in its ground state, without electron or hole populations. The external field is also set to zero. These assumptions give the Wannier equation in the form

$$2\hbar v_F|\boldsymbol{k}|\,\phi_\lambda(\boldsymbol{k}) - \sum_{\boldsymbol{p}} W(\boldsymbol{k}\text{–}\boldsymbol{p})\,\phi_\lambda(\boldsymbol{p}) = E_\lambda\,\phi_\lambda(\boldsymbol{k}) \tag{6.1}$$

with the Coulomb potential $W(q)$ (2.6). The index λ enumerates the set of solutions to the eigenvalue problem, and $\phi_\lambda(\boldsymbol{k})$ is the eigenfunction for the exciton.

Since we are interested in studying the onset of excitonic solutions, some simplifications have been done before arriving at the equation above. If the pair-forming is considered likely only in regions close to the Dirac points, the linear approximation can be used for the dispersion and the Coulomb matrix elements. This simplifies the problem by making the system rotationally symmetric. For isotropic systems, the lowest-lying states are also isotropic. Hence, we will only look for s-like electron–hole wavefunctions. The angle dependencies in the two-dimensional momentum can be integrated out, giving a one-dimensional problem to solve.

An electron–hole pair has two momentum variables, which can be taken as the center-of-mass and the relative momentum. The Schrödinger equation for the exciton contains both of these momenta. With a quadratic dispersion, the Schrödinger equation separates into two independent equations, one for each degree of freedom. With a linear dispersion, however, the two degrees of freedom do not separate [38]. To study the full two-body problem in graphene, one would consequently have to solve for the two degrees of freedom simultaneously. This could be done by solving inhomogeneous equations of motion like those in chapter 5. In the present situation, however, we can limit our investigations to stationary excitons, and we can therefore eliminate the center-of-mass degree of freedom.

6.2 Interpretation of bound states in a gapless system

In standard semiconductor models, with parabolic bands and nonzero band gaps, the Wannier equation is a hydrogen-like Schrödinger equation. The binding en-

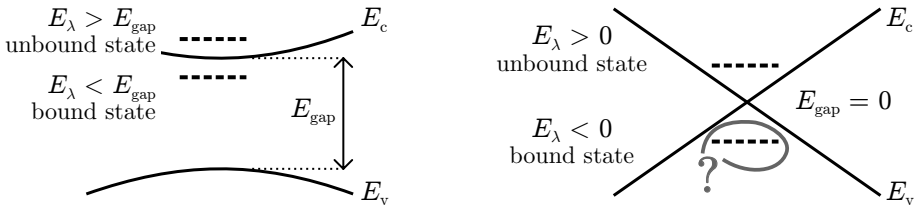

FIGURE 6.1 Bound and unbound states with and without band gaps.

ergy of the lowest-lying excitons are a few meVs, which is a small fraction of a typical eV band gap.

For bound states in gapped systems, the eigenenergy of the Wannier equation E_λ is the band gap E_{gap} minus the binding energy of the electron–hole pair E_b. As E_b is much smaller than E_{gap}, the state energy is a positive quantity. This situation is illustrated in the first panel of figure 6.1. Typically, the energy of the bound state is significantly above the energy of the ground state, which is zero. Hence, bound-state Wannier solutions in a gapped system have a natural interpretation as excited states of the system.

In case there is a solution where the binding energy is larger than the band gap, this interpretation breaks down. We were assuming that the empty conduction and filled valence band, i.e., the system empty of electron and hole populations, was the ground state of the system. However, since the exciton has an energy below the energy of the state empty of populations, this assumption was false. In such a situation, an exciton-like solution to the Wannier equation is a sign that the unpopulated electron and hole bands are not the true ground state.

In graphene, the ground state is assumed to be the unpopulated tight-binding electron and hole bands. Since the band gap is zero, any bound-state Wannier solution, if it exists, has an energy below that assumed ground state. The Wannier equation can therefore be used to look for where the tight-binding ground state assumption breaks down.

To study the onset of bound states, we compare the kinetic energy and Coulomb energy of the Wannier eigenstates. These two energies can be calculated by multiplying the Wannier equation by the wavefunction $\phi_\lambda(\boldsymbol{k})^*$ and integrating over momentum space, giving

$$2\hbar v_F \int \sum_{\boldsymbol{k}} |\boldsymbol{k}| \phi_\lambda(\boldsymbol{k})^2 - \sum_{\boldsymbol{pk}} W(\boldsymbol{k}-\boldsymbol{p}) \phi_\lambda(\boldsymbol{p}) \phi_\lambda(\boldsymbol{k}) = E_\lambda \,. \tag{6.2}$$

When the Coulomb energy (the second term) is larger than the kinetic energy (the first term) the state energy E_λ is negative and the electron–hole pair is in a bound state.

6.3 The coupling strength in the Wannier equation

In order to study the intrinsic properties of the Wannier equation, we rewrite (6.1) in a dimensionless form. Using the layer thickness d as a length scale, and the energy $E_0 = \hbar v_F/d$ as an energy scale gives us unitless versions of the momentum $\boldsymbol{\eta} = \boldsymbol{k}d$ and the energy E_λ/E_0, respectively. The wavefunction is also rescaled, since it should be normalized under the condition $\int \mathrm{d}\boldsymbol{k}|\phi(\boldsymbol{k})|^2 = \int \mathrm{d}\boldsymbol{\eta}|\psi(\boldsymbol{\eta})|^2 = 1$. This gives the scaled wavefunction $\psi(\boldsymbol{\eta}) = \phi(\boldsymbol{k})/d$. The dimensionless form of the Wannier equation is

$$2|\boldsymbol{\eta}|\psi_\lambda(\boldsymbol{\eta}) - \frac{\alpha}{2\pi}\int \mathrm{d}\boldsymbol{\eta}' \, \frac{F(|\boldsymbol{\eta}-\boldsymbol{\eta}'|)}{|\boldsymbol{\eta}-\boldsymbol{\eta}'|}\psi_\lambda(\boldsymbol{\eta}') = \frac{E_\lambda}{E_0}\,\psi_\lambda(\boldsymbol{\eta})\,. \tag{6.3}$$

The function $F(\boldsymbol{\eta})$ is the geometrical modulation of the Coulomb interaction, described in section 2.3. As all the quantities now are dimensionless, the only free parameter is the coupling strength

$$\alpha = \frac{e^2}{4\pi\epsilon\epsilon_0\hbar v_F}\,.$$

The coupling strength α determines the relative strength of the Coulomb interaction, and thereby the behavior of the Wannier equation in graphene. This was also the case for the system Hamiltonian in scaled units (2.9) and for the equations of motion in scaled units (4.7).

6.4 Solving the Wannier equation for different coupling strengths

We are using the existence of bound-state solutions of the Wannier equation as a criterion for the onset of a strong-coupling phase in graphene. The clearest indication of a bound state is the solution with the largest binding energy. Of the range of eigenfunctions λ, the 1s solution is the strongest bound, and is therefore the clearest indication of a possible bound state. We can therefore limit our investigation to s-like solutions of the Wannier equation, that is, solutions where the wavefunction is independent of the momentum angle. This reduces the two-dimensional problem to a one-dimensional one. Linear eigenvalue problems

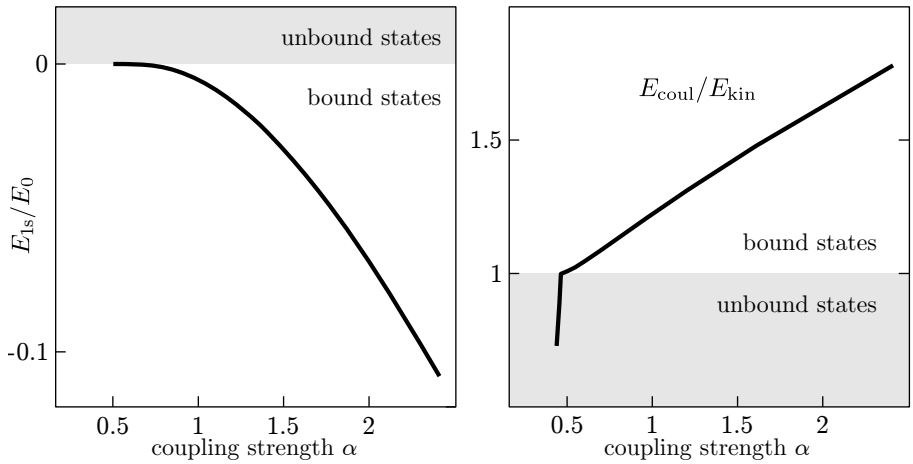

FIGURE 6.2 The eigenenergy E_λ of the strongest bound ($\lambda = 1s$) solution of the Wannier equation, as a function of the coupling strength.

such as this zero-population Wannier equation can be solved numerically, by discretizing momentum space into N intervals or points. Discretizing momentum turns the Coulomb integral into a sum, and the left-hand side can be written as a matrix $\boldsymbol{M}$ times an eigenvector $\boldsymbol{\psi}_\lambda$. The Wannier equation turns into a matrix eigenvalue problem, of the form

$$\boldsymbol{M}\boldsymbol{\psi}_\lambda = E_\lambda \boldsymbol{\psi}_\lambda \,.$$

The N by N matrix $\boldsymbol{M}$ has N eigenvalues. Solving the eigenproblem numerically gives us N values for the eigenenergy E_λ, as well as N eigenfunctions $\boldsymbol{\psi}_\lambda$. Of the eigenvalues, some may have a negative value for the energy, and the rest positive values. The negative energies correspond to bound states and positive ones to unbound states, where the electron and hole are at some position in the band, above the band gap, and not bound to each other by Coulomb interaction.

Significantly for the numerics, the wavefunctions for bound states have a nonzero width in momentum space. For a reliable estimate for the energy of a given bound state, one needs enough momentum grid points to resolve the wavefunction of that particular state. The 1s state, having the strongest Coulomb binding, has the widest wavefunction and is therefore the easiest to resolve — provided that it exists. Depending on how fine we make the momentum grid, we can resolve more and more bound states in addition to the 1s state.

To study the onset of bound-state solutions, we solve the Wannier equation numerically for a range of different values of the coupling strength α. The 1s en-

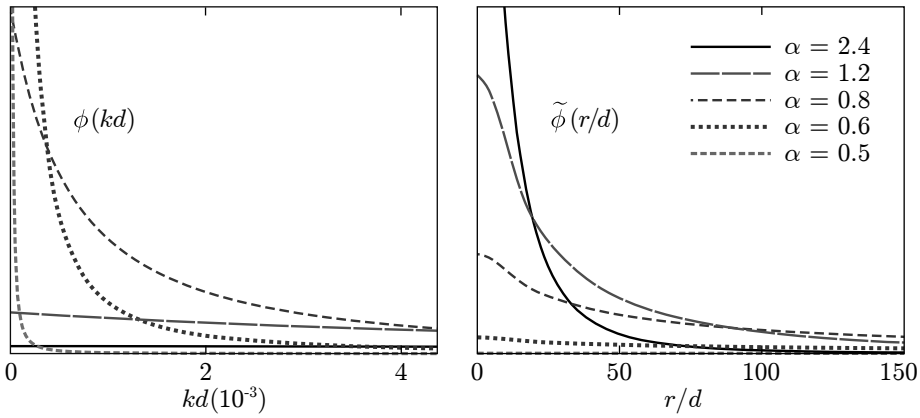

Figure 6.3 The wavefunctions of the strongest bound solutions of the Wannier equation, for different values of the coupling strength α. Left panel in k space and right panel in real space.

ergy is shown in figure 6.2 as a function of coupling strength. For larger coupling strengths, there are bound state solutions; the larger the coupling strength, the larger the binding energy. Significantly, there are no bound states at all for coupling strengths below approximately 0.46. Coupling strengths larger than this critical value puts the system in the strong-coupling phase, where the unpopulated tight-binding bands are no longer the ground state of the system.

In figure 6.3 are shown wavefunctions for a selection of α values. Solutions for large coupling strengths have wavefunctions that are nonzero over a large area in momentum space. Conversely, their wavefunction in real space is localized to a small area, as that pair has a large Coulomb attraction and a relatively small kinetic energy. Solutions for lower coupling strengths are narrower in momentum space, and increasingly delocalized in real space.

As the wavefunction becomes narrower near the switch point, the bound state solutions are increasingly challenging to resolve numerically. To see the switch more clearly, we calculate the ratio of Coulomb to kinetic energy for the solutions, shown in the second panel of figure 6.2. These are the first and second term of (6.2). As long as the ratio is above one, the solution is a bound state. This behavior of the Wannier equation shows that the tight-binding description of the ground state is not valid when α is above the switching point. We can see that the energy ratio in figure 6.2 forms an approximately linear function of α. There is also a clear 'kink' at the switch point where the ratio crosses one, indicating the transition between the tight-binding phase and strong-coupling phase.

Chapter 7

Finding the ground state — the gap equations

In the previous chapter, we established that the tight-binding description of the ground state of graphene is inadequate in the presence of a strong enough Coulomb interaction between the electrons. In this chapter, we proceed to find a more suitable ground state description. This is also the topic of section 3 of Paper III and section 2 of Paper IV.

We find the ground state by minimizing the energy of the electronic state, in terms of our dynamical quantities from chapter 4; the population and the polarization. The external field is zero in this chapter, as we are studying the inherent properties of the unexcited system.

As it turns out, the new ground state has an energy gap in the band structure. The size of the gap depends on the strength of the Coulomb interaction, similarly to the binding energy of the Wannier exciton from the previous chapter. The band gap in our study opens because of Coulomb interaction, but the effect is in other ways similar to the band gap opening in superconductivity [44, 45] with pairing of the electrons and transformation of the quasiparticles.

7.1 Band gaps in graphene

The tight-binding band structure is a consequence of the hexagonal symmetry of the atomic lattice. The linear energy cone at the Dirac point exists only as long as the hexagonal symmetry is preserved. Any kind of deviation from the perfect lattice breaks the symmetry between the A and B sublattices in the graphene sheet, and will give rise to an energy gap at the Dirac point.

What we study in this thesis is a spontaneous opening of a band gap, where the symmetry breaking is due to interaction among the electrons. A band gap

can also be achieved by other means, such as limiting system size, to form nanoribbons or nanoflakes, or by periodicity, like for carbon nanotubes. A band gap can also be created by introducing impurities or disorder in or around the lattice. Since a band gap is crucial for using graphene as a transistor, large amounts of work has been directed at investigating these kinds of circumstances [46, 47]. The strong-coupling ground state in graphene and its influence on band structure has been studied with various methods for example in [48–52].

7.2 Minimizing the energy of the electronic state

The electronic ground state of the system is the state with the lowest energy expectation value $\langle E\rangle$. We want to find the state that minimizes this energy. At the level of the mean-field approximation, the electronic state of graphene is defined by the polarization $P_{\boldsymbol{k}}$ and by $f_{\boldsymbol{k}}$, which is the population of electrons in the conduction band as well as the population of holes in the valence band. The mean-field level of approximation was the same we used when truncating the equations of motion at the Hartree–Fock level (4.3). The minimum energy can be found by varying the energy with respect to the population and the polarization.

To find the ground state, we first construct an expression for the energy expectation value of a general state, given in terms of the population and the polarization. The expectation value of the energy of a state, $\langle E\rangle$, is calculated as the expectation value of the Hamiltonian, $\langle \hat{H}_0 + \hat{H}_{\text{coul}}\rangle$. The Coulomb energy $\langle \hat{H}_{\text{coul}}\rangle$ of the state contains four-operator expectation values, which we reduce to two-operator expectation values using Hartree–Fock factorization, $\langle \hat{a}_1^\dagger \hat{a}_2^\dagger \hat{a}_3 \hat{a}_4\rangle \approx \langle \hat{a}_1^\dagger \hat{a}_4\rangle\langle \hat{a}_2^\dagger \hat{a}_3\rangle - \langle \hat{a}_1^\dagger \hat{a}_3\rangle\langle \hat{a}_2^\dagger \hat{a}_4\rangle$. This way, we obtain also the Coulomb energy in terms of the population $f_{\boldsymbol{k}}$ and the polarization $P_{\boldsymbol{k}}$, which are the two-operator expectation values;

$$\langle E\rangle = \sum_{\boldsymbol{k}} 2\hbar v_F |\boldsymbol{k}| f_{\boldsymbol{k}} - \sum_{\boldsymbol{k}\boldsymbol{k}'} W(\boldsymbol{k}\text{–}\boldsymbol{k}') \Big[\cos(\theta_{\boldsymbol{k}}\text{–}\theta_{\boldsymbol{k}'})\, f_{\boldsymbol{k}} f_{\boldsymbol{k}'} + P_{\boldsymbol{k}} P_{\boldsymbol{k}'}\Big]. \tag{7.1}$$

The first term is the kinetic energy, and the second term is the Coulomb energy of the state. We have assumed that $f_{\boldsymbol{k}}$ and $P_{\boldsymbol{k}}$ depend only on $|\boldsymbol{k}|$ and not on the momentum angle, and that $P_{\boldsymbol{k}}$ is real.

To proceed, we minimize the energy of the state with respect to the functions $f_{\boldsymbol{k}}$ and $P_{\boldsymbol{k}}$. In Paper III, we perform the steps of the functional variation. During the calculations, the quantities $\Sigma_{\boldsymbol{k}}$ and $\Omega_{\boldsymbol{k}}$ appear in the equations. Like in the equations of motion, they are related to $f_{\boldsymbol{k}}$ and $P_{\boldsymbol{k}}$ through

$$\Sigma_{\boldsymbol{k}} = \hbar v_{\scriptscriptstyle F}|\boldsymbol{k}| - \sum_{\boldsymbol{k}'} W(\boldsymbol{k}{-}\boldsymbol{k}')\cos(\theta_{\boldsymbol{k}}{-}\theta_{\boldsymbol{k}'})f_{\boldsymbol{k}'} \text{ and } \Omega_{\boldsymbol{k}} = \sum_{\boldsymbol{k}'} W(\boldsymbol{k}{-}\boldsymbol{k}')P_{\boldsymbol{k}'}. \quad (7.2)$$

Minimizing the state energy gives the following conditions,

$$2\bar{P}_{\boldsymbol{k}} = \frac{\bar{\Omega}_{\boldsymbol{k}}}{\sqrt{\bar{\Sigma}_{\boldsymbol{k}}^2 + \bar{\Omega}_{\boldsymbol{k}}^2}} \qquad \text{and} \qquad 1 - 2\bar{f}_{\boldsymbol{k}} = \frac{\bar{\Sigma}_{\boldsymbol{k}}}{\sqrt{\bar{\Sigma}_{\boldsymbol{k}}^2 + \bar{\Omega}_{\boldsymbol{k}}^2}}\,. \quad (7.3)$$

The state that fulfills the minimizing conditions (7.3) is the ground state of the system. We denote the ground state quantities with a bar,

$$\bar{f}_{\boldsymbol{k}}, \bar{P}_{\boldsymbol{k}}, \bar{\Sigma}_{\boldsymbol{k}}, \text{ and } \bar{\Omega}_{\boldsymbol{k}}.$$

We could now use equations (7.2) and (7.3) to eliminate either $f_{\boldsymbol{k}}$ and $P_{\boldsymbol{k}}$, or $\Sigma_{\boldsymbol{k}}$ and $\Omega_{\boldsymbol{k}}$ from the calculations. It is convenient to state the minimizing conditions (7.3) completely in terms of $\Sigma_{\boldsymbol{k}}$ and $\Omega_{\boldsymbol{k}}$, eliminating $f_{\boldsymbol{k}}$ and $P_{\boldsymbol{k}}$; as the quantities $\Sigma_{\boldsymbol{k}}$ and $\Omega_{\boldsymbol{k}}$ have a more direct connection to the quasiparticle transformation discussed in section 7.4.

7.3 The gap equations

Minimizing the energy of the state (7.1) and eliminating $\bar{f}_{\boldsymbol{k}}$ and $\bar{P}_{\boldsymbol{k}}$ using (7.3) leaves us with integral equations for $\bar{\Sigma}_{\boldsymbol{k}}$ and $\bar{\Omega}_{\boldsymbol{k}}$,

$$\bar{\Sigma}_{\boldsymbol{k}} = \hbar v_{\scriptscriptstyle F}|\boldsymbol{k}| - \sum_{\boldsymbol{k}'} W(\boldsymbol{k}{-}\boldsymbol{k}')\cos(\theta{-}\theta')\,\frac{1}{2}\left(1 - \frac{\bar{\Sigma}_{\boldsymbol{k}'}}{\sqrt{\bar{\Sigma}_{\boldsymbol{k}'}^2 + \bar{\Omega}_{\boldsymbol{k}'}^2}}\right) \quad (7.4)$$

$$\bar{\Omega}_{\boldsymbol{k}} = \sum_{\boldsymbol{k}'} W(\boldsymbol{k}{-}\boldsymbol{k}')\frac{1}{2}\frac{\bar{\Omega}_{\boldsymbol{k}'}}{\sqrt{\bar{\Sigma}_{\boldsymbol{k}'}^2 + \bar{\Omega}_{\boldsymbol{k}'}^2}}\,. \quad (7.5)$$

These equations we refer to as the gap equations. Solving the gap equations gives us the energies $\bar{\Sigma}_{\boldsymbol{k}}$ and $\bar{\Omega}_{\boldsymbol{k}}$, which define the electronic ground state of the system. Additionally, we can use relation (7.3) to calculate the populations $\bar{f}_{\boldsymbol{k}}$ and $\bar{P}_{\boldsymbol{k}}$ of the ground state.

The gap equations (7.4) and (7.5) are integral equations, which can be solved by iteration. We start with some approximations for $\bar{\Sigma}_{\boldsymbol{k}}$ and $\bar{\Omega}_{\boldsymbol{k}}$, and input the approximations on the right-hand side. Performing the integration over $\boldsymbol{k}$ on the right-hand side gives a new approximation for $\bar{\Sigma}_{\boldsymbol{k}}$ and $\bar{\Omega}_{\boldsymbol{k}}$. This new approximation is used as the next input on the right-hand side, and so on. If the equations are well-behaved, as they are in the present case, the successive

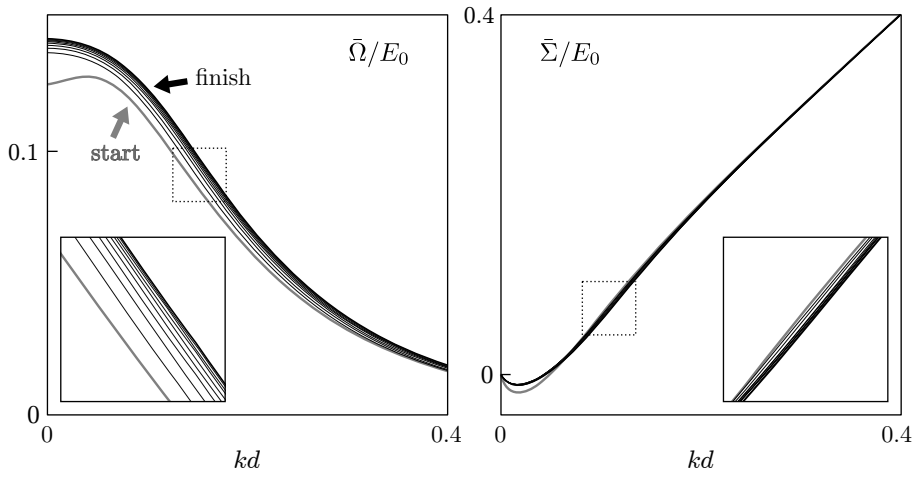

Figure 7.1 The iterative process of solving the gap equations.

approximations converge towards a stable solution of the equations. An example of the steps of the iteration process are shown in figure 7.1. The thick gray line is the starting approximation, and the thick black line is the solution after ten iterations, shown as thinner lines. The iteration procedure, in this case, converges well.

In figure 7.2 is shown a gap equation solution for $\bar{\Sigma}_{\boldsymbol{k}}$ and $\bar{\Omega}_{\boldsymbol{k}}$. The resulting strong-coupling dispersion E_k^{MF} (7.8) is shown for comparison. There is a clear region around $k = 0$ where the gap equation solution is non-trivial, in other words, where $\bar{\Omega}_{\boldsymbol{k}} > 0$, and $\bar{\Sigma}_{\boldsymbol{k}}$ is below the linear dispersion $\hbar v_{\scriptscriptstyle F}|\boldsymbol{k}|$. Also shown in figure 7.2 are the corresponding populations $\bar{f}_{\boldsymbol{k}}$ and $\bar{P}_{\boldsymbol{k}}$, which are given by (7.3). In the region in k where the gap equation solution is non-trivial, $\bar{f}_{\boldsymbol{k}}$ and $\bar{P}_{\boldsymbol{k}}$ are larger than zero. Both $\bar{f}_{\boldsymbol{k}}$ and $\bar{P}_{\boldsymbol{k}}$ are $1/2$ at $k = 0$.

The gap equations always have the trivial solution where the Coulomb sums are zero; $\bar{\Sigma}_{\boldsymbol{k}} = \hbar v_{\scriptscriptstyle F}|\boldsymbol{k}|$ and $\bar{\Omega}_{\boldsymbol{k}} = 0$. The trivial solution corresponds to $\bar{f}_{\boldsymbol{k}} = \bar{P}_{\boldsymbol{k}} = 0$, which is the tight-binding ground state. In the present context, we are interested in circumstances under which the gap equations have non-trivial solutions, which would correspond to a strong-coupling ground state of the system.

To write the gap equations in scaled units, we follow the same procedure as for the equations of motion, and as for the Wannier equation: by scaling the energies with $E_0 = \hbar v_{\scriptscriptstyle F}/d$, and the momentum as kd. Performing these steps in (7.4) and (7.5), the only free parameter left is the coupling strength $\alpha = e^2/4\pi\epsilon\epsilon_0\hbar v_{\scriptscriptstyle F}$, as a factor determining the strength of the Coulomb interaction. This is the role α played in the previous contexts, as well.

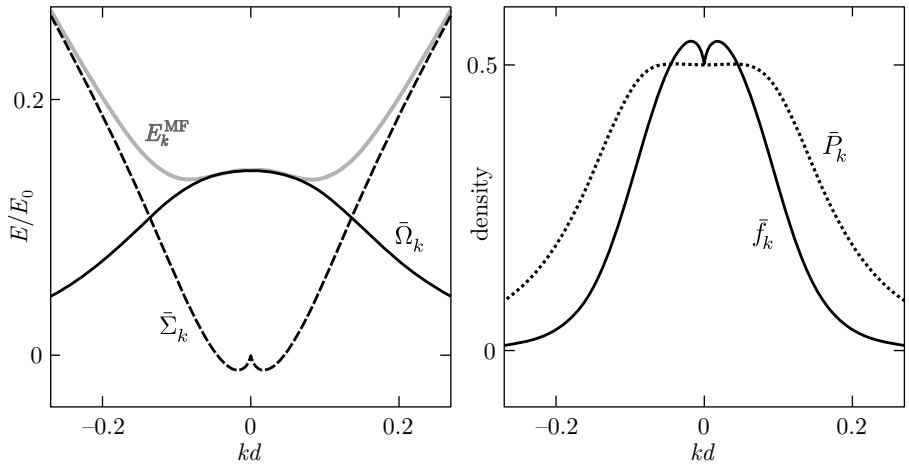

Figure 7.2 The solution of the gap equations for graphene in vacuum, $\alpha = 2.4$.

Solving the gap equations for different coupling strengths, we find results which support the conclusions obtained from solving the Wannier equation in the previous chapter. That is to say, the gap equations have a non-trivial solution whenever the coupling constant α is large enough — in the strong-coupling regime, $\alpha > 0.46$. The strong-coupling regime coincides with the α range where the Wannier equation has bound-state solutions.

The results for a few different values of α are show in figure 7.3. For higher values of α, the solution for the internal field $\bar{\Omega}_k$ has a higher maximum, and is nonzero over a larger region around $k = 0$. For the single-particle energy $\bar{\Sigma}_k$, the behavior is dominated by the static linear part, still a higher α creates a stronger deviation from the linear dependence.

For the corresponding population $\bar{f}_k$ and polarization $\bar{P}_k$, shown in the lower pane of figure 7.3, a higher α creates a larger k area where the solution is nonzero, like it does for $\bar{\Omega}_k$. In contrast to $\bar{\Omega}_k$ though, both the population and the polarization stay at 0.5 at the Dirac point for all values of α in the strong-coupling regime. For α below the critical value, all strong-coupling solutions disappear, and only the trivial solution remains.

7.4 The strong-coupling ground state and band structure

When the Coulomb coupling α is large enough, the ground state is no longer the unpopulated tight-binding bands derived in chapter 1. Instead, there is a

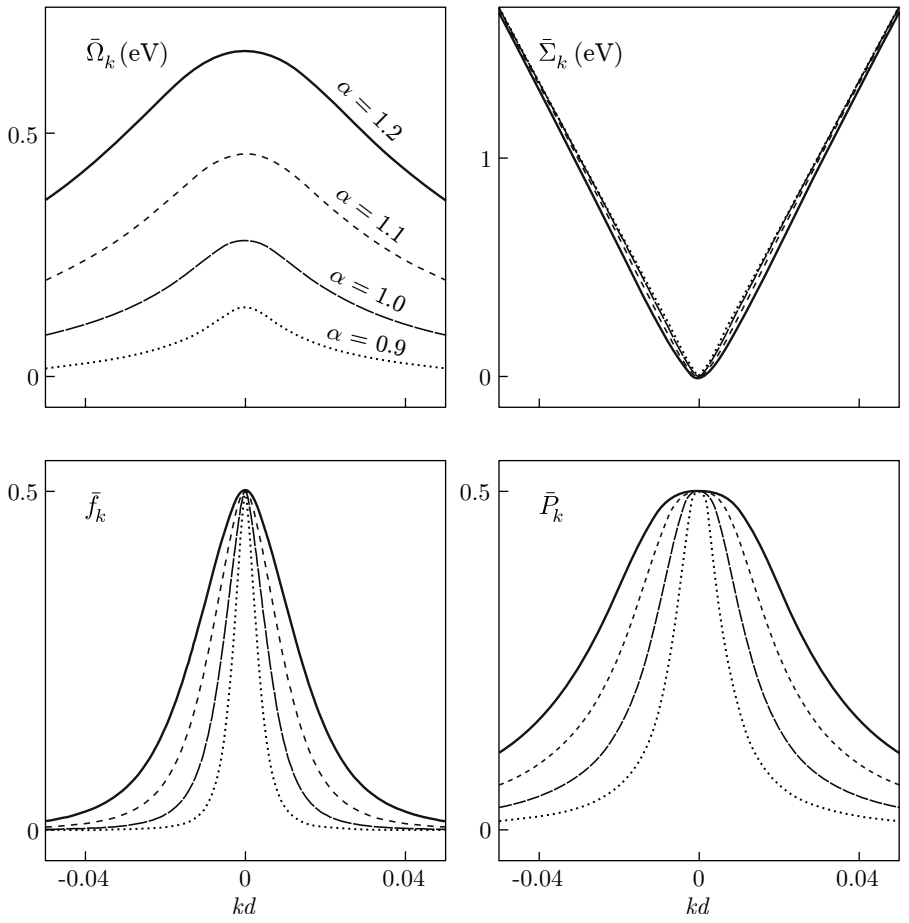

Figure 7.3 Solutions of the gap equations for different values of the coupling strength α.

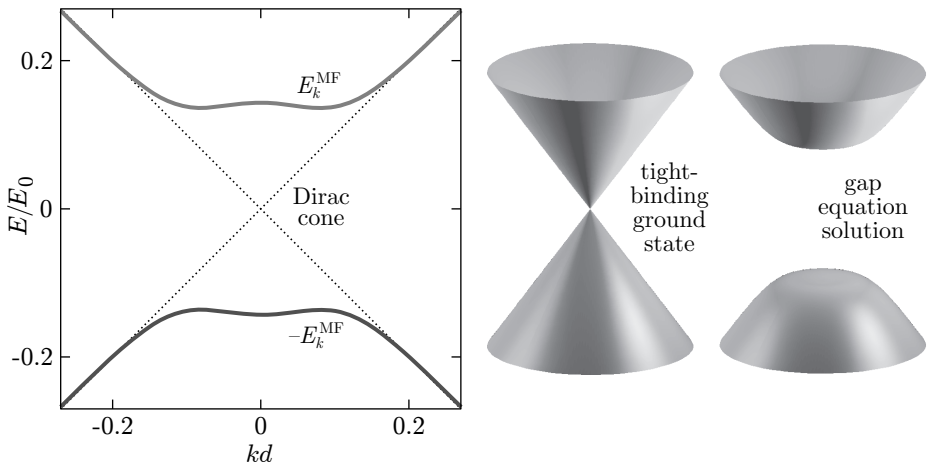

FIGURE 7.4 The strong-coupling band structure $E_{\boldsymbol{k}}^{\mathrm{MF}}$ (7.8).

new strong-coupling ground state with nonzero populations on the tight-binding bands. These populations are the $\bar{f}_{\boldsymbol{k}}$ and $\bar{P}_{\boldsymbol{k}}$ that we found as solutions of the gap equations. The populated strong-coupling ground state can also be expressed as an unpopulated state, by forming a new quasiparticle basis, i.e. by creating new definitions for the electron and hole. These new quasiparticles are created by forming a linear combination of the old (weak-coupling) electron and hole. We want the new quasiparticles to be defined in such a way that their populations are zero in the ground state, like the weak-coupling quasiparticle populations are zero in the ground state when α is small enough.

Finding the quasiparticles for which the ground state is empty, is equivalent to finding the quasiparticle operators for which the Hamiltonian is diagonal. As we work at the mean-field level, we are interested in diagonalizing the mean-field level Hamiltonian. While we in the previous chapters performed the Hartree-Fock factorization in the equations of motion, we here need to do it one step earlier, in the Hamiltonian. For the Hamiltonian we use (1.11) and (2.4), $\hat{H}_0 + \hat{H}_{\mathrm{coul}}$. In $\hat{H}_{\mathrm{coul}}$, we perform a factorization in the four-operator terms,

$$\sum_{\boldsymbol{kpq}} V_{\boldsymbol{kpq}} \hat{a}_{\boldsymbol{k}}^\dagger \hat{a}_{\boldsymbol{p}}^\dagger \hat{a}_{\boldsymbol{p}+\boldsymbol{q}} \hat{a}_{\boldsymbol{k}-\boldsymbol{q}} \approx -\sum_{\boldsymbol{kp}} V_{\boldsymbol{k},\boldsymbol{p},\boldsymbol{k}-\boldsymbol{p}} (\langle \hat{a}_{\boldsymbol{p}}^\dagger \hat{a}_{\boldsymbol{p}} \rangle \hat{a}_{\boldsymbol{k}}^\dagger \hat{a}_{\boldsymbol{k}} + \langle \hat{a}_{\boldsymbol{k}}^\dagger \hat{a}_{\boldsymbol{k}} \rangle \hat{a}_{\boldsymbol{p}}^\dagger \hat{a}_{\boldsymbol{p}}) \,.$$

This gives the mean-field Hamiltonian $\hat{H}_{\mathrm{MF}}$. Analyzing the sums in $\hat{H}_{\mathrm{MF}}$ it can be seen that the gap equation solutions $\bar{\Sigma}_{\boldsymbol{k}}$ and $\bar{\Omega}_{\boldsymbol{k}}$ reappear.

$$\hat{H}_0 + \hat{H}_{\text{coul}} \approx \hat{H}_{\text{MF}} = \sum_{\boldsymbol{k}} \bar{\Sigma}_{\boldsymbol{k}} (\hat{a}^\dagger_{\text{c}\boldsymbol{k}} \hat{a}_{\text{c}\boldsymbol{k}} - \hat{a}^\dagger_{\text{v}\boldsymbol{k}} \hat{a}_{\text{v}\boldsymbol{k}}) - \bar{\Omega}_{\boldsymbol{k}} (\hat{a}^\dagger_{\text{c}\boldsymbol{k}} \hat{a}_{\text{v}\boldsymbol{k}} + \hat{a}^\dagger_{\text{v}\boldsymbol{k}} \hat{a}_{\text{c}\boldsymbol{k}}) \quad (7.6)$$

Diagonalizing the Hamiltonian $\hat{H}_{\text{MF}}$, we arrive at a representation that features a new band structure $E^{\text{MF}}_{\boldsymbol{k}}$,

$$\hat{H}_{\text{MF}} = \sum_{\boldsymbol{k}} E^{\text{MF}}_{\boldsymbol{k}} \hat{C}^\dagger_{\boldsymbol{k}} \hat{C}_{\boldsymbol{k}} - E^{\text{MF}}_{\boldsymbol{k}} \hat{V}^\dagger_{\boldsymbol{k}} \hat{V}_{\boldsymbol{k}} \,. \quad (7.7)$$

The new strong-coupling band structure is a combination of the gap equation solutions,

$$E^{\text{MF}}_{\boldsymbol{k}} = \sqrt{\bar{\Sigma}^2_{\boldsymbol{k}} + \bar{\Omega}^2_{\boldsymbol{k}}} \,. \quad (7.8)$$

These new bands are shown in figure 7.4 for graphene in vacuum, $\alpha = 2.4$. The original tight-binding band structure is indicated by dotted lines.

The diagonal Hamiltonian (7.7) also features the new quasiparticle operators $\hat{C}_{\boldsymbol{k}}$ $\hat{C}^\dagger_{\boldsymbol{k}}$ $\hat{V}_{\boldsymbol{k}}$ $\hat{V}^\dagger_{\boldsymbol{k}}$, which annihilate or create an electron in the new bands $E^{\text{MF}}_{\boldsymbol{k}}$. The strong-coupling ground state has a filled valence band and an empty conduction band in terms of these new quasiparticles; that is to say, it is empty of electron and hole populations. The new quasiparticle operators are linear combinations of the old tight-binding quasiparticle operators, given by the diagonalization transformation of $\hat{H}_{\text{MF}}$,

$$\begin{pmatrix} \hat{C}_{\boldsymbol{k}} \\ \hat{V}_{\boldsymbol{k}} \end{pmatrix} = \frac{1}{\sqrt{2E^{\text{MF}}_{\boldsymbol{k}}}} \begin{pmatrix} \sqrt{E^{\text{MF}}_{\boldsymbol{k}} + \bar{\Sigma}_{\boldsymbol{k}}} & \sqrt{E^{\text{MF}}_{\boldsymbol{k}} - \bar{\Sigma}_{\boldsymbol{k}}} \\ -\sqrt{E^{\text{MF}}_{\boldsymbol{k}} - \bar{\Sigma}_{\boldsymbol{k}}} & \sqrt{E^{\text{MF}}_{\boldsymbol{k}} + \bar{\Sigma}_{\boldsymbol{k}}} \end{pmatrix} \begin{pmatrix} \hat{a}_{\text{c}\boldsymbol{k}} \\ \hat{a}_{\text{v}\boldsymbol{k}} \end{pmatrix} . \quad (7.9)$$

The strong-coupling band structure is shown in figure 7.5, for a few values of the coupling strength α. As can be seen, there is a gap between the valence and conduction band opening up for large enough values of α. The band gap E_{gap} (the distance in energy between the lowest point of the conduction band and the highest point of the valence band) is shown as a function of α in the left panel of figure 7.5. The band gap grows rapidly with increasing α.

The bands corresponding to the highlighted values of α are shown in the right panel of the figure. They follow the same patterns as the gap equation solutions of figure 7.3, as can be expected, given relation (7.8). For larger coupling strengths, the deviation from the tight-binding bands is more evident. Close to the Dirac point $k = 0$, the $\bar{\Omega}$ part of the band (7.8) is dominant, as $\bar{\Sigma}$ tends to zero. For

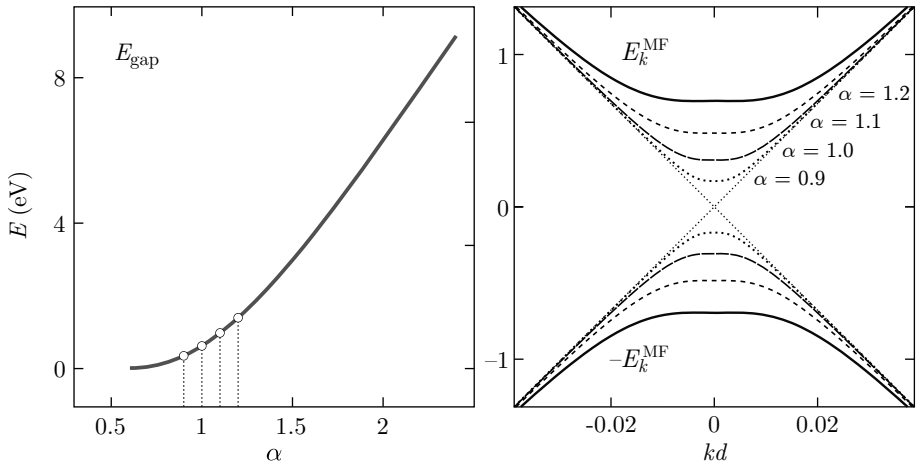

FIGURE 7.5 Band gap and band structure $E_{\boldsymbol{k}}^{\rm MF}$ of the strong-coupling ground state as function of the coupling strength α.

larger values of k, $\bar{\Omega}$ goes to zero, and the weak-coupling, linear part of $\bar{\Sigma}$ in (7.4) takes over.

Chapter 8

Exciting the strong-coupling ground state

Once we have established the strong-coupling ground state of graphene, we wish to see how our system behaves when it is taken out of this ground state. We achieve this by exciting the system with an external electric field — by applying a source of light. This is the topic of section 4 of Paper III and section 3 of Paper IV.

In this chapter, we modify the equations of motion from chapter 4 to explicitly account for the properties of the strong-coupling ground state from the previous chapter. Based on the equations of motion, we calculate spectra for the absorption of light of different frequencies in the system. The absorption spectra show signatures of a semiconductor-like system, with a band gap and excitonic resonances.

8.1 The ground state as initial condition

The time development of the system is obtained by solving the equations of motion. As initial state we use the strong-coupling ground state calculated in chapter 7.

There are two equivalent ways to account for the strong-coupling ground state. One possibility is to transform the quasiparticle operators to the new strong-coupling basis (7.9). In this case, the bands are the strong-coupling ones (7.8) with a gap in the band structure. The system would start off in the ground state, which in this basis is empty of electrons and holes. An applied external light would create electron and hole populations, which would be time-dependent.

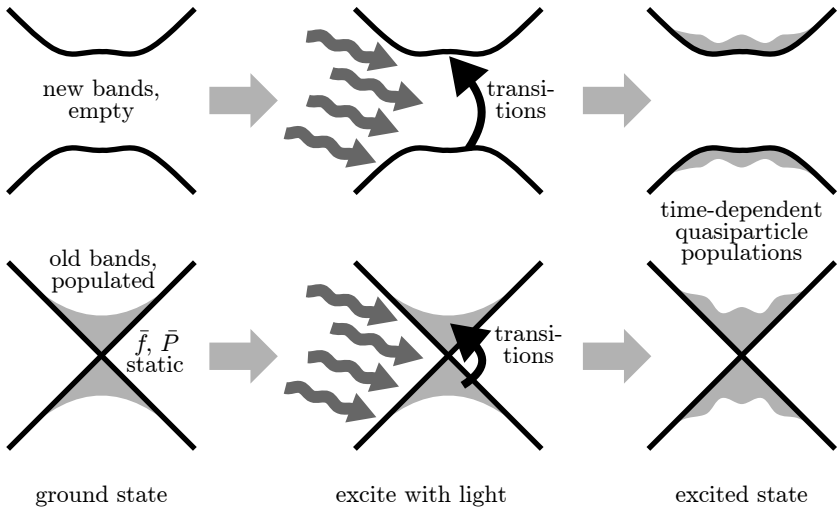

Figure 8.1 Two equivalent approaches for accounting for the strong-coupling ground state.

The other possibility is to stay in the tight-binding quasiparticle basis, and consequently, to keep the tight-binding bands (1.13). The initial condition of the system is the tight-binding bands, with electron and hole populations given by the gap equation solutions. The applied light would create modifications to the ground state populations, and these modifications would be time-dependent. These two options are illustrated in figure 8.1, with the strong-coupling bands as well as tight-binding bands, and the respective electron and hole populations shown as shaded areas.

In this study, we choose the second option, to stay in the tight-binding basis. Doing so allows us to keep using the same Hamiltonian operators and the matrix elements we already derived for the interaction with light and the interaction between electrons. If we were to use the strong-coupling basis, we would have a basis dependent on the Coulomb strength.

In the following, we will split the populations $f_{\boldsymbol{k}}$ and $P_{\boldsymbol{k}}$ into a ground state part which is static and an excited part which is time-dependent. This separation simplifies the equations of motion as the static part obeys the gap equations, which leads to cancellations of terms in the equations. Splitting the quantities also allows for clearer analysis of the geometry of the time dynamics, as the static part is isotropic and the dynamic part can have, in principle, any angular dependence. Additionally, we will later want to simplify the dynamics by assuming that the excited populations are small; for this purpose the separation

is necessary. We write the splitting as

$$\begin{aligned} f_{\boldsymbol{k}}(t) &= \bar{f}_k + \Delta f_{\boldsymbol{k}}(t) \\ P_{\boldsymbol{k}}(t) &= \bar{P}_k + \Delta P_{\boldsymbol{k}}(t). \end{aligned} \tag{8.1}$$

The barred quantities are the time-independent distributions in the ground state, which we obtained in the previous chapter by solving the gap equations. The Δ parts of $f_{\boldsymbol{k}}$ and $P_{\boldsymbol{k}}$ are the excited, time-dependent parts, which are created by the external light. With this splitting of $f_{\boldsymbol{k}}$ and $P_{\boldsymbol{k}}$, the internal field $\Omega_{\boldsymbol{k}}$ and the renormalized energy $\Sigma_{\boldsymbol{k}}$ will also split into a ground state part and an excited part, $\Omega_{\boldsymbol{k}}(t) = \bar{\Omega}_k + \Delta\Omega_{\boldsymbol{k}}(t)$ and $\Sigma_{\boldsymbol{k}}(t) = \bar{\Sigma}_k + \Delta\Sigma_{\boldsymbol{k}}(t)$. The static parts contain the ground state populations, and the dynamical parts contain the excited populations. As we will see, the dynamical parts of $\Omega_{\boldsymbol{k}}$ and $\Sigma_{\boldsymbol{k}}$ also contain the external light field itself.

8.2 Equations of motion

As we are still working in the tight-binding basis, the time evolution of the populations is still described by the equations of motion (4.4) given in chapter 4. We here wish to express the equations in a form that explicitly includes our ground state, in order to discuss the consequences of the strong-coupling phase for the dynamics. We therefore introduce the separation (8.1) into a static and a dynamic part, in the equations of motion (4.4) for the quantities $f_{\boldsymbol{k}}$, $P_{\boldsymbol{k}}$, $\Sigma_{\boldsymbol{k}}$, and $\Omega_{\boldsymbol{k}}$.

The time derivative of the static parts being zero, we need to consider the time evolution only for the dynamic parts of our quantities. The equations of motion for $f_{\boldsymbol{k}}(t)$ and $P_{\boldsymbol{k}}(t)$ become equations of motion for their dynamical parts $\Delta f_{\boldsymbol{k}}(t)$ and $\Delta P_{\boldsymbol{k}}(t)$. The resulting equations are

$$\begin{aligned} \hbar\frac{\mathrm{d}}{\mathrm{d}t}\Delta f_{\boldsymbol{k}} &= -2\,\mathrm{Im}\big[\Delta P^*_{\boldsymbol{k}}\bar{\Omega}_k + \bar{P}_k\Delta\Omega_{\boldsymbol{k}} + \Delta P^*_{\boldsymbol{k}}\Delta\Omega_{\boldsymbol{k}}\big] \\ i\hbar\frac{\mathrm{d}}{\mathrm{d}t}\Delta P_{\boldsymbol{k}} &= 2\bar{\Sigma}_k\Delta P_{\boldsymbol{k}} + 2\Delta\Sigma_{\boldsymbol{k}}\bar{P}_k + 2\Delta\Sigma_{\boldsymbol{k}}\Delta P_{\boldsymbol{k}} \\ &\quad - \big(1-2\bar{f}_k\big)\Delta\Omega_{\boldsymbol{k}} + 2\Delta f_{\boldsymbol{k}}\bar{\Omega}_k + 2\Delta f_{\boldsymbol{k}}\Delta\Omega_{\boldsymbol{k}}, \quad \text{with} \\ \Delta\Sigma_{\boldsymbol{k}}(t) &= -\sum_{\boldsymbol{k}'}\Big[\big(V^+_{\boldsymbol{k}\boldsymbol{k}'} - V^-_{\boldsymbol{k}\boldsymbol{k}'}\big)\Delta f_{\boldsymbol{k}'}(t) + 2i\,V^A_{\boldsymbol{k}\boldsymbol{k}'}\,\mathrm{Im}\Delta P_{\boldsymbol{k}'}(t)\Big] - \frac{e}{m}\boldsymbol{A}(t)\boldsymbol{p}^{\mathrm{cc}}_{\boldsymbol{k}} \\ \Delta\Omega_{\boldsymbol{k}}(t) &= \sum_{\boldsymbol{k}'}\Big[V^+_{\boldsymbol{k}\boldsymbol{k}'}\,\Delta P_{\boldsymbol{k}'}(t) + V^-_{\boldsymbol{k}\boldsymbol{k}'}\,\Delta P^*_{\boldsymbol{k}'}(t) + 2\,V^A_{\boldsymbol{k}\boldsymbol{k}'}\,\Delta f_{\boldsymbol{k}'}(t)\Big] + \frac{e}{m}\boldsymbol{A}(t)\boldsymbol{p}^{\mathrm{cv}}_{\boldsymbol{k}}\,. \end{aligned} \tag{8.2}$$

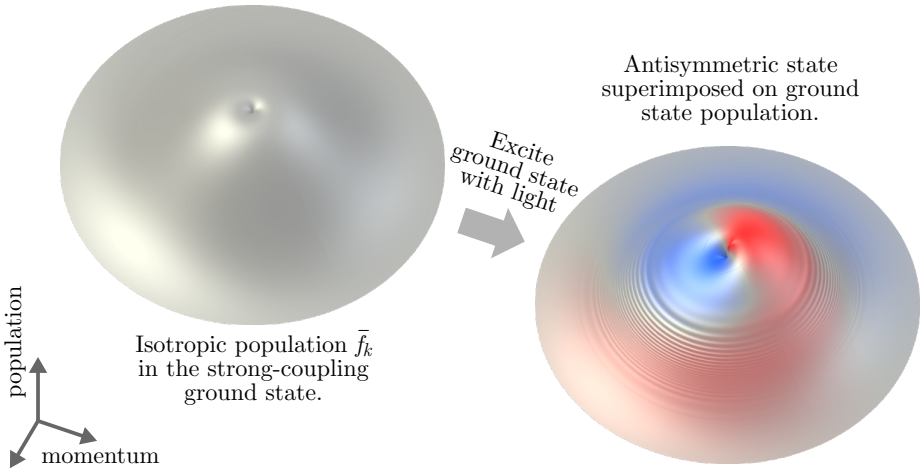

Figure 8.2 The light creates p-like states on the s-like ground state.

In the equation for $\Delta P_{\boldsymbol{k}}$ above, we have used the staticness of the ground state quantities, by canceling terms using the relation $\big(1-2\bar{f}_k\big)\bar{\Omega}_k = 2\bar{\Sigma}_k\bar{P}_k$.

8.3 Influence of light on the dynamics

To study the dynamics of the system in the strong-coupling phase, we need to bring the system out of its ground state. We take our description of the system dynamics, which are the equations of motion (8.2). Excitation is created by applying an external electromagnetic field. In the equations of motion, this is achieved by letting the terms with the external field $\boldsymbol{A}(t)$ be nonzero. The system is then allowed to evolve freely in time, under the influence of the field. Initially, the external field will gradually create more excitation in the system.

Some of the initial dynamics can be understood by inspecting the form of the equations of motion. At the start of the run, all Δ quantities are zero. When the light $\boldsymbol{A}(t)$ is turned on, the quantities $\Delta\Sigma_{\boldsymbol{k}}$ and $\Delta\Omega_{\boldsymbol{k}}$ acquire a nonzero contribution, proportional to $\boldsymbol{A}(t)$. Due to those, the time derivatives of $\Delta f_{\boldsymbol{k}}$ and $\Delta P_{\boldsymbol{k}}$ also have nonzero contributions;

$$\begin{aligned}\hbar\frac{\mathrm{d}}{\mathrm{d}t}\Delta f_{\boldsymbol{k}} &= -2\,\mathrm{Im}\big[\bar{P}_k\Delta\Omega_{\boldsymbol{k}}\big]\\ i\hbar\frac{\mathrm{d}}{\mathrm{d}t}\Delta P_{\boldsymbol{k}} &= 2\Delta\Sigma_{\boldsymbol{k}}\bar{P}_k - \big(1-2\bar{f}_k\big)\Delta\Omega_{\boldsymbol{k}}\,.\end{aligned}$$

Through their nonzero time derivatives, the populations $\Delta f_{\boldsymbol{k}}$ and $\Delta P_{\boldsymbol{k}}$ themselves gradually become nonzero. This in turn leads to more terms in the equa-

tions of motion becoming nonzero, and eventually all of them contribute to the dynamics.

The initial distribution of $f_{\boldsymbol{k}}$ is shown on the left in figure 8.2. This is the radially symmetric ground state population $f_{\boldsymbol{k}} = \bar{f}_k$, as was also shown in figure 7.2, here plotted over a two-dimensional momentum space. On the right in figure 8.2 is shown a snapshot of the dynamical population $f_{\boldsymbol{k}} = \bar{f}_k + \Delta f_{\boldsymbol{k}}$, after exciting the system with a short pulse of light. Areas where $\Delta f_{\boldsymbol{k}}$ is negative are shown in blue, and positive in red.

We can observe that the light has created p-like states, that is, states with a sine or cosine dependence on the angle of the momentum, antisymmetric under half a rotation. This is due to the angular dependence of the optical matrix elements $\boldsymbol{p}_{\boldsymbol{k}}$ (3.5) and the polarization of the field $\boldsymbol{A}(t)$; the light terms in the equations of motion make their "stamp mark" on the dynamical quantities.

8.4 Absorption spectra in the strong-coupling phase

We calculate the absorption of the system the same way as in section 3.3; with the current $\boldsymbol{j}(t)$ from (3.7). In the present case, with the population split into ground state and excited parts, the current is expressed with $\Delta f_{\boldsymbol{k}}(t)$ and $\Delta P_{\boldsymbol{k}}(t)$. The expression for the current takes the form

$$\begin{aligned}\boldsymbol{j}(t) = \frac{ep}{m} \sum_{\boldsymbol{k}} \big[\cos\theta_{\boldsymbol{k}}\, \Delta f_{\boldsymbol{k}}(t) - \sin\theta_{\boldsymbol{k}}\, \mathrm{Im}\Delta P_{\boldsymbol{k}}(t)\big]\, \hat{\boldsymbol{e}}_x \\ + \big[\sin\theta_{\boldsymbol{k}}\, \Delta f_{\boldsymbol{k}}(t) + \cos\theta_{\boldsymbol{k}}\, \mathrm{Im}\Delta P_{\boldsymbol{k}}(t)\big]\, \hat{\boldsymbol{e}}_y\,.\end{aligned} \tag{8.3}$$

The optical matrix elements (3.5) have contributed with a sine or a cosine of the momentum angle in each term of the expression above. Any parts of Δf and ΔP which are an even function of the angle will therefore give zero for the integration $\sum_{\boldsymbol{k}}$ over the angle. Hence, only antisymmetric parts of Δf and ΔP contribute to the current.

First off, we calculate the absorption of the simplest version of the system; the single-particle approximation. We therefore neglect Coulomb interaction between electrons in the equations of motion (8.2). It can be noted that we keep the strong-coupling ground state, and that the Coulomb interaction we neglect is just the one between the strong-coupling quasi-electrons. This is equivalent to neglecting terms containing explicit Coulomb potentials in the equations of motion, i.e. the terms with $V_{\boldsymbol{k}\boldsymbol{k}'}$ in the expressions for $\Delta\Sigma_{\boldsymbol{k}}$ and $\Delta\Omega_{\boldsymbol{k}}$ in (8.2).

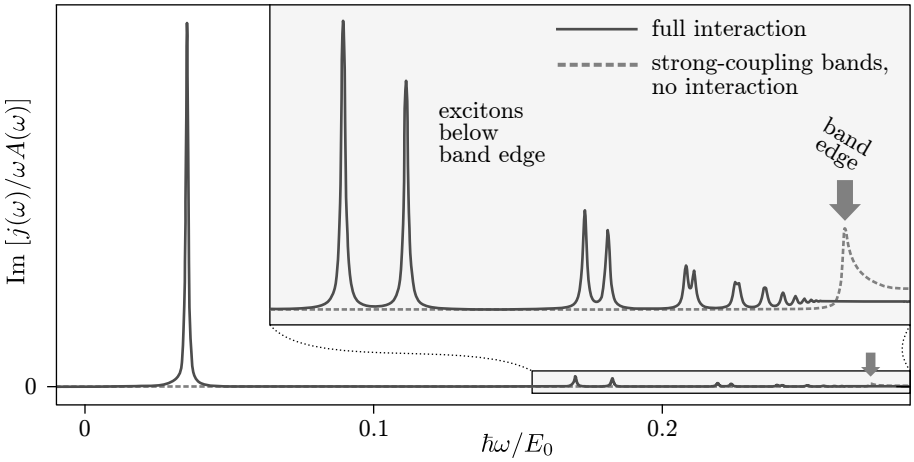

Figure 8.3 Absorption spectrum for graphene in the strong-coupling phase.

The resulting spectrum is shown with a dashed line in figure 8.3. The profile of a gapped band structure can be seen, with a clear band edge, indicated by the arrows in the figure. Above the band edge, we see the shape of the density of states in the strong-coupling bands. Below the band edge, the spectrum shows zero absorption, as expected in a gapped system without electron–electron interaction.

8.5 Coulomb interaction and excitons in the spectra

To show the effect of Coulomb interaction between the electrons in the simplest form, we solve the equations to linear order in the external field. This comes down to discarding the terms which contain products of Δ quantities in the equations of motion (8.2).

The resulting linear absorption spectrum is shown as a solid line in figure 8.3. We can see a series of resonances below the band edge. These resonances show the existence of excitons in the strong-coupling bands. These exciton peaks are situated below the band edge, but above the energy of the strong-coupling ground state, which is zero. These are proper excitonic states of the system in the strong-coupling phase, in contrast to the excitonic-like states with an eigenenergy below the presumed ground state in chapter 6, which were the solutions of the Wannier equation in the tight-binding bands.

The exciton peaks in the spectrum are higher and more separated towards lower energies. Towards the band edge the peaks become lower and closer to-

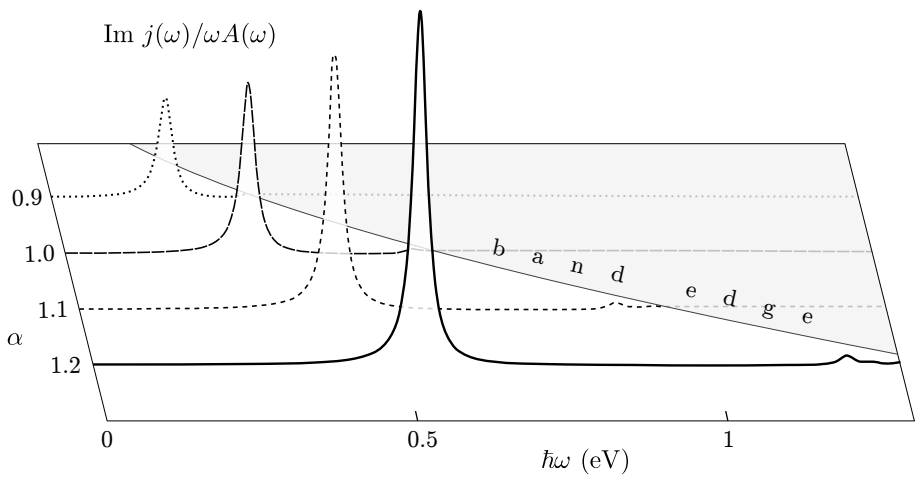

Figure 8.4 Spectra for different values of the Coulomb strength α.

gether, and eventually blend into the continuum of unbound states above the band edge. In the sequence of peaks we can also see a peculiar doubling rhythm. This phenomenon comes from a degeneracy lifting due to Auger terms in the Coulomb interaction, which is studied further in Paper IV. All the bright excitons are p-like — they have sine-type angle dependence. If we were to include higher orders of the external field in our solution, the light would create s and d excitons from the p excitons, and from there on all orders of excitons.

To study the influence of the Coulomb coupling strength α, we perform several runs of the time evolution under a pulse of light, for different values of α above the strong-coupling threshold. The value of α influences the ground state in the form of the populations $\bar{f}_k$ and $\bar{P}_k$. It also influences explicit Coulomb interaction in the form of potentials $V_{\boldsymbol{kk}'}$ in equations of motion (8.2).

The resulting linear spectra are shown in figure 8.4. The spectra shown here are calculated with a higher and more realistic dephasing rate γ than in the previous picture, hence the peaks are more diffuse, and only the most prominent peak is clear in each spectrum. The curve marked 'band edge' is the same as E_{gap} versus α in figure 7.5. The spectra for different α all have qualitatively the same features, at different energies. Essentially, they all have exciton peaks. For higher values of α, the most prominent exciton is relatively more strongly bound, as in distance from the band edge, but is situated at a higher energy in the spectrum, since the band gap is also larger for higher α. The exciton peaks are also higher for higher α. Towards lower α, and the transition to weak coupling at $\alpha \approx 0.46$, the band gap and the exciton peaks scale down evenly.

Chapter 9

Strong Coulomb coupling in bilayer graphene

In addition to carbon nanotubes and single graphene layers, there are other low-dimensional possibilities for arranging the carbon atoms. One arrangement, which turns out to be particularly interesting with respect to the strong-coupling phase is bilayer graphene, specifically in a particular configuration referred to as Bernal stacking [53–55].

The methods we developed for single layer graphene, using many-body equations of motion based on the tight-binding matrix elements, are almost directly applicable also for bilayer graphene. The matrix elements for bilayer graphene are also calculated using the tight-binding approach, accounting for atomic sites in two separate but connected layers.

In this chapter, we calculate the band structure and Coulomb matrix elements of bilayer graphene, as well as set up the equations of motion and gap equations. Applying our methods to bilayer graphene in this way is also part of the contents of Papers V and VI.

We also set up and solve the Wannier equation, in the same way we did for single layer graphene in chapter 6, in order to look for exciton states energetically below the single-particle ground state. Like in the single-layer case, the presence of such states shows that the tight-binding description of the ground state is insufficient. By analyzing the numerical solutions of the bilayer Wannier equation, we find that Bernal-stacked bilayer graphene is always in a strong-coupling phase, independent of the strength of the Coulomb interaction between electrons.

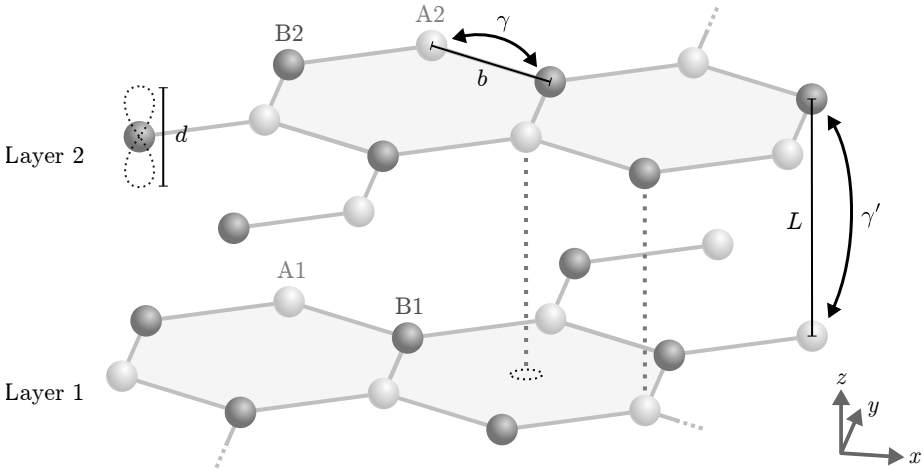

Figure 9.1 Bilayer graphene in the Bernal stacking.

9.1 Atomic configuration of Bernal-stacked bilayer graphene

Bilayer graphene consists of two graphene layers stacked on top of each other, close enough for the electrons in the two sheets to form a coupled many-body system. For our purposes, the most useful configuration is so-called Bernal stacked graphene, which is illustrated in figure 9.1. In this variant of bilayer graphene, the two layers are stacked so that a B atom in the upper sheet is above an A atom in the lower sheet, and an A atom in the upper sheet is above an empty site.

In the combined system, there are four different types of atomic sites. We label them A_1 B_1 A_2 B_2, depending on the layer they are in and if they are in an A or B type position within their individual sheets. The positions of these different sites are given by

$$\begin{aligned} \boldsymbol{R}^{B1} &= \boldsymbol{R}^{A1} + \boldsymbol{b}_n \text{ with } \; n = 1, 2, 3, \text{ as in single layer,} \\ \boldsymbol{R}^{B2} &= \boldsymbol{R}^{A1} + L\hat{\boldsymbol{e}}_z \\ \boldsymbol{R}^{A2} &= \boldsymbol{R}^{B2} - \boldsymbol{b}_n = \boldsymbol{R}^{A1} - \boldsymbol{b}_n + L\hat{\boldsymbol{e}}_z \,. \end{aligned} \tag{9.1}$$

We use L to denote the distance between the two layers of graphene. The overlap integral between two orbitals centered on atomic sites directly above each other, on separate layers, we denote γ',

$$\gamma' \equiv \int \phi(\boldsymbol{x})\, \hat{H}_0\, \phi(\boldsymbol{x} - L\hat{\boldsymbol{e}}_z)\, \mathrm{d}\boldsymbol{x}\,. \tag{9.2}$$

This relation also specifies the relation between L and γ' — a larger interlayer distance leads to a smaller interlayer hopping matrix element.

9.2 Tight-binding for bilayer graphene

We derive a system Hamiltonian for bilayer graphene, using the tight-binding approach in the same way we did for single-layer graphene in section 1.3. We derive a transformation from the sublattice picture to a band picture. At the same time, this gives us expressions for the band dispersions themselves, and for the transformation between electron creation and annihilation operators in the two bases. We present here an outline of the tight-binding derivation, together with the most important results and some details on how to perform the calculations. A more general and comprehensive presentation is given in section 2 and appendix B of Paper V.

We use the same sublattice wavefunction expansion (1.10) as in the single-layer tight-binding derivation, as well as the same p_z orbitals (1.1) for the electrons around the atomic sites. The difference is that there are now four sublattice operators. Accounting for the strongest couplings in the lattice gives a Hamiltonian in the form

$$\hat{H}_0 = \begin{pmatrix} \hat{A}_{1\boldsymbol{k}} \\ \hat{B}_{1\boldsymbol{k}} \\ \hat{A}_{2\boldsymbol{k}} \\ \hat{B}_{2\boldsymbol{k}} \end{pmatrix}^\dagger \begin{pmatrix} 0 & \gamma g_{\boldsymbol{k}}^* & 0 & \gamma' \\ \gamma g_{\boldsymbol{k}} & 0 & 0 & 0 \\ 0 & 0 & 0 & \gamma g_{\boldsymbol{k}}^* \\ \gamma' & 0 & \gamma g_{\boldsymbol{k}} & 0 \end{pmatrix} \begin{pmatrix} \hat{A}_{1\boldsymbol{k}} \\ \hat{B}_{1\boldsymbol{k}} \\ \hat{A}_{2\boldsymbol{k}} \\ \hat{B}_{2\boldsymbol{k}} \end{pmatrix}. \tag{9.3}$$

The sublattice Hamiltonian matrix contains two 2×2 block matrices on the diagonal. These represent the two sheets of graphene individually, by describing hopping between sites A_1 and B_1 and between A_2 and B_2. The intralayer nearest-neighbor hopping is given by $\gamma g_{\boldsymbol{k}}$, as was derived in section 1.3. The coupling between the sheets is the off-diagonal components γ', which describe hopping between sites B_2 and A_1, which in the Bernal stacking are neighbors in the z direction.

Diagonalizing this matrix gives us the Hamiltonian in the band picture, as well as the transformation between the sublattice and the band picture. As we

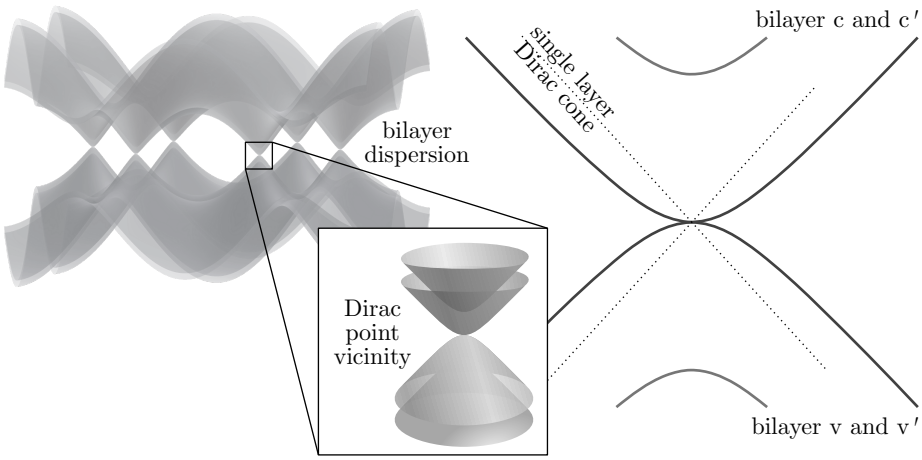

Figure 9.2 The tight-binding band structure of Bernal-stacked bilayer graphene. The valence and conduction band of single-layer graphene have each been split into two bands.

have a 4×4 matrix, diagonalization will give us 4 bands. We label these c, c′, v and v′.

$$\hat{H}_0 = \frac{1}{2} \begin{pmatrix} \hat{c}'_{\boldsymbol{k}} \\ \hat{c}_{\boldsymbol{k}} \\ \hat{v}_{\boldsymbol{k}} \\ \hat{v}'_{\boldsymbol{k}} \end{pmatrix}^{\dagger} \begin{pmatrix} \sqrt{\ } + \gamma' & 0 & 0 & 0 \\ 0 & \sqrt{\ } - \gamma' & 0 & 0 \\ 0 & 0 & -\sqrt{\ } + \gamma' & 0 \\ 0 & 0 & 0 & -\sqrt{\ } - \gamma' \end{pmatrix} \begin{pmatrix} \hat{c}'_{\boldsymbol{k}} \\ \hat{c}_{\boldsymbol{k}} \\ \hat{v}_{\boldsymbol{k}} \\ \hat{v}'_{\boldsymbol{k}} \end{pmatrix} \tag{9.4}$$

with $\sqrt{\ } \equiv \sqrt{4\gamma^2 |g_{\boldsymbol{k}}|^2 + \gamma'^2}$. The expressions on the diagonal are the dispersion of the four bands, shown in figure 9.2.

Each graphene layer, on its own, naturally has the dispersion of single layer graphene. Through the interlayer coupling, these two dispersions are shifted away from each other in energy, as shown in figure 9.2. The combination of two sets of linear dispersion becomes four bands, which at the Dirac point acquire a quadratic component due to mixing of the contributions from the two layers.

Anticipating that our calculations will take place at low energies in the vicinity of the Dirac points, we use only the two energetically lower bands, c and v of figure 9.3, and neglect the c′ and v′ bands. This is a valid approximation for energies smaller than γ'. In the vicinity of the Dirac points, the linear approximation of $g_{\boldsymbol{k}}$ is also valid, with the expressions presented in section 1.6.

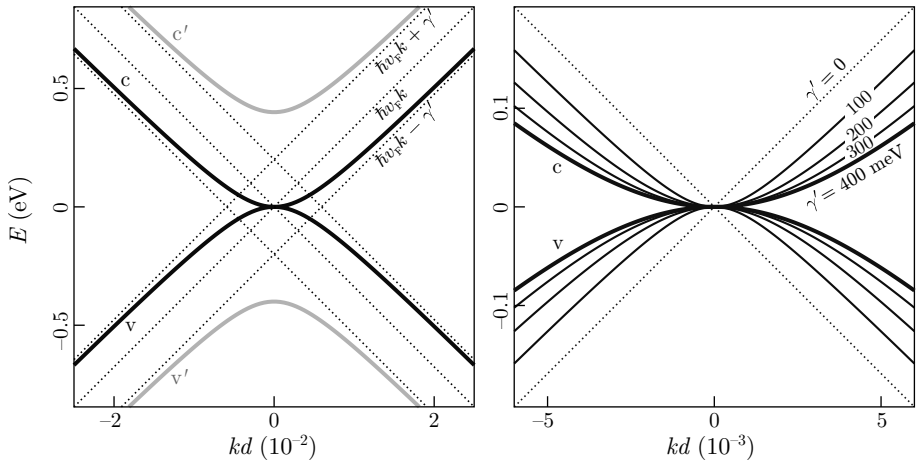

Figure 9.3 In the left pane, the four bands of bilayer graphene near the Dirac point. In the right pane, the influence of the interlayer coupling on c and v.

In the linear approximation, the dispersion of the bands c and v in bilayer graphene is

$$E_{\boldsymbol{k}} = \pm\Big(\sqrt{(\hbar v_F \boldsymbol{k})^2 + \frac{\gamma'^2}{4}} - \frac{\gamma'}{2}\Big). \tag{9.5}$$

As can be seen from the expression and from figure 9.3, the bilayer dispersion has a quadratic dependence on k close to the Dirac point, and goes to the linear $\hbar v_F k$ dependence further away from the Dirac point.

The influence of the interlayer coupling γ' is also shown in figure 9.3. For all values of γ', the bands c and v meet in the middle, with a zero band gap. For larger values of γ', the range of influence for the quadratic-like contribution is larger. For smaller values of γ', the dispersion goes towards that of single layer graphene, the $\gamma' = 0$ case, with a linear dispersion.

The transformation between the sublattice basis and the band basis also comes from the diagonalization of the Hamiltonian (9.3). The transformation matrix is the analogue of the functions $C^{A,B}_{\lambda \boldsymbol{k}}$ which we used in chapter 1, and will be used for calculating matrix elements for the bilayer Coulomb interaction. Close to the Dirac points where $|g_{\boldsymbol{k}}| \ll \gamma'$, the transformation to the c and v bands is given by

$$\begin{pmatrix} \hat{c}_{\boldsymbol{k}} \\ \hat{v}_{\boldsymbol{k}} \end{pmatrix} = \frac{1}{\sqrt{2}} \begin{pmatrix} -|g_{\boldsymbol{k}}| & -\gamma' \dfrac{g_{\boldsymbol{k}}^*}{|g_{\boldsymbol{k}}|} & \gamma' \dfrac{g_{\boldsymbol{k}}}{|g_{\boldsymbol{k}}|} & |g_{\boldsymbol{k}}| \\ |g_{\boldsymbol{k}}| & -\gamma' \dfrac{g_{\boldsymbol{k}}^*}{|g_{\boldsymbol{k}}|} & -\gamma' \dfrac{g_{\boldsymbol{k}}}{|g_{\boldsymbol{k}}|} & |g_{\boldsymbol{k}}| \end{pmatrix} \begin{pmatrix} \hat{A}_{1\boldsymbol{k}} \\ \hat{B}_{1\boldsymbol{k}} \\ \hat{A}_{2\boldsymbol{k}} \\ \hat{B}_{2\boldsymbol{k}} \end{pmatrix}. \tag{9.6}$$

As $|g_{\boldsymbol{k}}|$ is small, we can observe that the leading terms are the middle two columns of the matrix. A more detailed and more general presentation of the transformation is given in appendix B of Paper V.

9.3 Coulomb interaction in bilayer graphene

The tight-binding wavefunctions give us the Hamiltonian for Coulomb interaction between electrons, in the same manner as in chapter 2. We start with a Coulomb Hamiltonian $\hat{H}_{\text{coul}}$ like (2.1), stated in terms of a general Coulomb matrix element V_{1234} like (2.2).

In the corresponding derivation for the single layer case, we derived the matrix element V_{1234} directly in the band basis. For the bilayer case here, in order to keep the expressions simpler, we will start by deriving the expression for V_{1234} in the sublattice basis, and transform to the band basis afterwards. In the sublattice basis, the indices $1 \ldots 4$ in V_{1234} refer to the combination of sublattice index and $\boldsymbol{k}$, and the general electron operators are the sublattice operators, $\hat{a}_i = \left\{ \hat{A}_{1\boldsymbol{k}}\, \hat{B}_{1\boldsymbol{k}}\, \hat{A}_{2\boldsymbol{k}}\, \hat{B}_{2\boldsymbol{k}} \right\}$.

Like we did for single-layer graphene in (2.3), we split the matrix element V_{1234} into two similar integrals, using the Fourier transformed Coulomb potential $V_{\boldsymbol{q}}^{\text{3D}}$. The integrals, denoted $I_{X\boldsymbol{k},X\boldsymbol{k}'}(\boldsymbol{q})$ with X as a sublattice index, are evaluated by inserting the tight-binding (sublattice) wavefunctions (1.10). For a given sublattice, the sums over lattice sites are evaluated as

$$I_{X\boldsymbol{k},X\boldsymbol{k}'}(\boldsymbol{q}) = \underbrace{\frac{1}{N} \sum_{\boldsymbol{R}_X} e^{-i(\boldsymbol{k}-\boldsymbol{k}'-\boldsymbol{q})\boldsymbol{R}_X}}_{= \delta_{\boldsymbol{k}', \boldsymbol{k}-\boldsymbol{q}_\parallel} e^{iLq_z}} \underbrace{\int \mathrm{d}\boldsymbol{x}\, \phi(\boldsymbol{x})^* e^{i\boldsymbol{q}\boldsymbol{x}} \phi(\boldsymbol{x})}_{= G(\boldsymbol{q})} \qquad \text{X in layer 2.}$$

When sublattice X in the integral I is in layer 1, the result is the same as in single-layer graphene. When sublattice X is in layer 2, there is an additional factor e^{iLq_z} from the sum over all lattice sites $\boldsymbol{R}_X$.

For the Coulomb matrix element V_{1234}, the consequence is an additional factor $e^{\pm iLq_z}$ under the sum over q_z whenever sublattices 1 and 2 are on different layers, as the contributions here accounted for are when sublattice $1 = 4$ and $2 = 3$.

$$V_{1234} = \sum_{\boldsymbol{q}_\parallel} \delta_{\boldsymbol{k}_4, \boldsymbol{k}_1 - \boldsymbol{q}_\parallel} \delta_{\boldsymbol{k}_3, \boldsymbol{k}_2 + \boldsymbol{q}_\parallel} \begin{cases} \underbrace{\sum_{q_z} V_{\boldsymbol{q}}^{3D} |G(\boldsymbol{q})|^2}_{= W(|\boldsymbol{q}_\parallel|)} & \text{1, 2 same layer} \\ \underbrace{\sum_{q_z} V_{\boldsymbol{q}}^{3D} e^{\pm iLq_z} |G(\boldsymbol{q})|^2}_{\equiv W'(|\boldsymbol{q}_\parallel|)} & \text{1, 2 different layers.} \end{cases} \tag{9.7}$$

Having dealt with the z direction by means of the sum over q_z, the variable $\boldsymbol{q}$ will from here on refer to the in-plane momentum, and q to its absolute value.

The first factor in V_{1234} expresses momentum conservation in the plane, and the second factor defines a weight for the Coulomb interaction, denoted by $W'(q)$. Like the single layer Coulomb weight $W(q)$, the function $W'(q)$ can be expressed as a product of the bare two-dimensional Coulomb potential $V(q) = e^2/2\epsilon\epsilon_0 \mathcal{A} q$ and a dimensionless form function, which we call $F'(qd)$:

$$W'(q) = F'(q) V(q).$$

The interlayer form function $F'(qd)$ is analogous to the sheet thickness (intralayer) form function $F(qd)$ in section 2.3. The interlayer form function contains the sheet thickness d as well as the layer separation L as parameters. The integral defining $W'(q)$ in (9.7) can be evaluated analytically using Mathematica, giving us an analytic expression for the form function;

$$\begin{aligned} F'(x,y) = {} & \pi e^{-xy}(1+6x^2)^2 - \pi e^{-y\sqrt{1+x^2}} \frac{x}{53760\sqrt{1+x^2}^{11}} \times \\ & \times \Big(3y^7 \sqrt{1+x^2}^7 + 14y^6 \sqrt{1+x^2}^6 (3x^2+4) \\ & + 280y^4 \sqrt{1+x^2}^6 (18x^4 + 33x^2 + 14) + 14y^5 \sqrt{1+x^2}^5 (36x^4 + 75x^2 + 40) \\ & + 35y^3 \sqrt{1+x^2}\, \Xi_1(x) + 210y^2\, \Xi_2(x) + 105y\sqrt{1+x^2}\, \Xi_3(x) + 105\, \Xi(x) \Big) \end{aligned} \tag{9.8}$$

with the polynomials

$$\begin{aligned}
\Xi_1(x) &\equiv 1152x^{10} + 5280x^8 + 9512x^6 + 8368x^4 + 3575x^2 + 591 \\
\Xi_2(x) &\equiv 1152x^{12} + 144x^{10} + 13400x^8 + 15208x^6 + 9399x^4 + 2982x^2 + 383 \\
\Xi_3(x) &\equiv 9216x^{12} + 46848x^{10} + 96640x^8 + 102640x^6 + 58456x^4 + 16706x^2 + 1963
\end{aligned} \tag{9.9}$$

and the polynomial $\Xi(x)$ as in (2.8). In the expression above, the variables are written as $x = qd$ and $y = L/d$ to save some space. The expression (9.8) itself is not particularly practical for manual work. Still, having the expression is valuable for understanding the behavior at small and large parameter values, as well as useful for numerical evaluations, since it eliminates one step of numerical approximations, the accuracy of which would need to be controlled.

Once we have V_{1234} in the sublattice basis (9.7), we can use (9.6) to transform the Coulomb Hamiltonian to the band basis. Collecting all the terms and performing the linear approximation (1.12), we obtain Coulomb matrix elements containing geometric factors in the form of a sine or cosine of the double angle of the momentum $\boldsymbol{k}$.

The Coulomb matrix elements are of the same three types as in the single-layer case, shown in figure 2.2, depending on whether they describe transitions in the bands, between bands, or Auger-type transitions. In bilayer graphene, the matrix elements for these three types have the form

$$\begin{aligned}
V^{\pm}_{\boldsymbol{k}\boldsymbol{k}'} &= \frac{1}{2} V(\boldsymbol{k}-\boldsymbol{k}') \Big[F\big((\boldsymbol{k}-\boldsymbol{k}')d\big) \pm \cos 2(\theta_{\boldsymbol{k}}-\theta_{\boldsymbol{k}'}) F'\big((\boldsymbol{k}-\boldsymbol{k}')d, L/d\big) \Big] \\
V^{\mathrm{A}}_{\boldsymbol{k}\boldsymbol{k}'} &= \frac{i}{2} V(\boldsymbol{k}-\boldsymbol{k}') \sin 2(\theta_{\boldsymbol{k}}-\theta_{\boldsymbol{k}'}) F'\big((\boldsymbol{k}-\boldsymbol{k}')d, L/d\big)
\end{aligned} \tag{9.10}$$

with $V(q) = e^2/2\epsilon\epsilon_0 \mathcal{A} q$. These matrix elements contain both the intralayer form function $F(qd)$ (2.7) and the interlayer form function $F'(qd, L/d)$ (9.8).

Screening of the Coulomb interaction is at this point still treated as a constant, in the form of a background dielectric constant ϵ in the Coulomb potential $V(q)$ in the matrix elements (9.10). The dielectric constant goes into the Coulomb coupling strength $\alpha = e^2/4\pi\epsilon\epsilon_0\hbar v_F$ which plays the same role here as in single layer graphene.

9.4 Quantities, equations of motion, and gap equations

Knowing the dispersion and the Coulomb matrix elements, we have what we need for deriving equations of motion for our microscopic many-body quantities. The quantities $f_{\boldsymbol{k}}$ and $P_{\boldsymbol{k}}$ are defined in the same way as for single-layer graphene,

(4.1) and (4.2). Since the bilayer Hamiltonian has the same terms as the single-layer graphene Hamiltonian, the equations of motion are also the same, (4.4) and (4.5), this time for the bilayer quantities. The difference is in the matrix elements; the dispersion E_k (9.5) and the Coulomb matrix elements $V^{\pm}$ and V^{A} (9.10).

The gap equations also follow in the same way from the equations of motion; in bilayer graphene they have the form

$$\begin{aligned} \Omega_{\boldsymbol{k}} &= \sum_{\boldsymbol{k}'} W(\boldsymbol{k}\text{–}\boldsymbol{k}')\frac{1}{2}\frac{\Omega_{\boldsymbol{k}'}}{\sqrt{\Omega_{\boldsymbol{k}'}^2+\Sigma_{\boldsymbol{k}'}^2}} \\ \Sigma_{\boldsymbol{k}} &= E_{\boldsymbol{k}} - \sum_{\boldsymbol{k}'} V(\boldsymbol{k}\text{–}\boldsymbol{k}')\, F'\big((\boldsymbol{k}\text{–}\boldsymbol{k}')d\big)\, \cos 2(\theta_{\boldsymbol{k}}\text{–}\theta_{\boldsymbol{k}'})\frac{\Sigma_{\boldsymbol{k}'}}{\sqrt{\Omega_{\boldsymbol{k}'}^2+\Sigma_{\boldsymbol{k}'}^2}}\,. \end{aligned} \tag{9.11}$$

9.5 The Wannier equation and the strong-coupling regime

Like in the case of single-layer graphene, since the system has no band gap, the existence of bound-state solutions of the Wannier equation is a marker for a breakdown of the tight-binding description, and the onset of a strong-coupling phase.

The Wannier equation for bilayer graphene can be derived the same way as for the single-layer case. The equation of motion for the polarization $P_{\boldsymbol{k}}(t)$ is Fourier transformed into the frequency domain, and then we look for eigenfunctions $\phi(\boldsymbol{k})$ and their eigenenergies E of that equation. The Wannier equation in bilayer graphene is

$$E_{\boldsymbol{k}}\,\phi(\boldsymbol{k}) + \sum_{\boldsymbol{q}} W(\boldsymbol{q}d)\,\phi(\boldsymbol{k}+\boldsymbol{q}) = E\,\phi(\boldsymbol{k}) \tag{9.12}$$

with the wavefunction $\phi(\boldsymbol{k})$ for the relative momentum coordinate of an electron–hole pair, the weighted two-dimensional Coulomb function $W(\boldsymbol{q}d)$, and the eigenenergy E. This is the same expression we had for the single layer case (6.1) except that the dispersion E_k here is the bilayer dispersion (9.5).

The eigenenergies of the Wannier equation are solved the same way as in the single layer case, by discretizing k space and using numerical linear algebra methods for eigenvalues. When a bound state solution exists, the eigenfunction of that state has a nonzero width around the band minimum. When the k space discretization has a sufficient number of grid points for a description of that

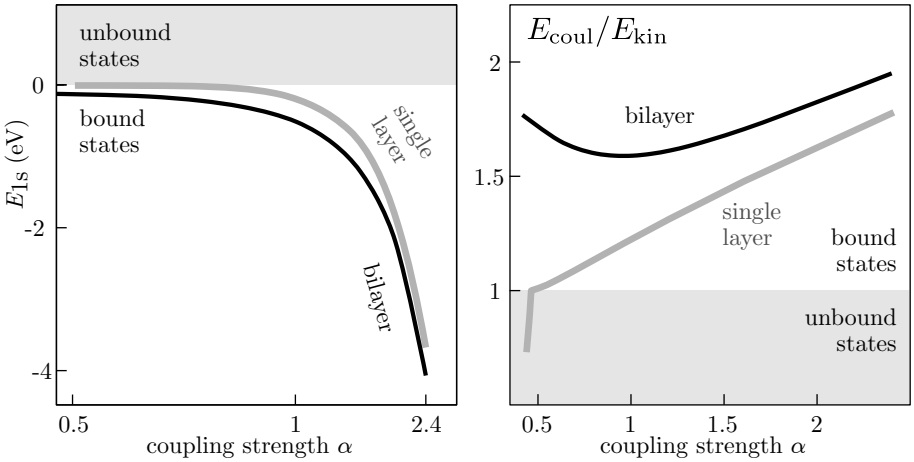

Figure 9.4 Eigenenergies of the bilayer Wannier equation.

eigenfunction, the value of the corresponding eigenenergy E has converged, that is to say, the value of E is unchanging when adding more grid points.

We solve the bilayer Wannier equation for different values of the Coulomb coupling strength α. The results for the lowest eigenenergy E_{1s} are shown in the left pane of figure 9.4, together with corresponding results for the single layer case. The eigenenergy E_{1s} as a function of α shows visually similar behavior for both the single layer and bilayer case — bound states with binding energies in the range of several eV for the nominal vacuum coupling strength $\alpha = 2.4$, and several orders of magnitude smaller for coupling strengths around 0.5.

There is still a clear difference in behavior between the single layer and bilayer Wannier solutions, which becomes more visible by looking at the ratio of Coulomb energy to kinetic energy for the eigenfunction for the energetically lowest state, shown in the right pane of figure 9.4. Since there is no band gap, the Wannier solution is a bound state whenever the Coulomb energy exceeds the kinetic energy, that is, when the ratio is larger than one. For the single-layer Wannier equation solution, the ratio is approximately linear with a clear crossover into the region of a ratio below one at $\alpha \approx 0.46$. The ratio for bilayer graphene behaves similarly for large α, but instead of crossing over, the ratio has a minimum at $\alpha \approx 1$, and then curves away towards larger values again when going towards smaller values of α. This implies that for any nonzero strength of the Coulomb interaction, our bilayer system is always in the strong-coupling regime.

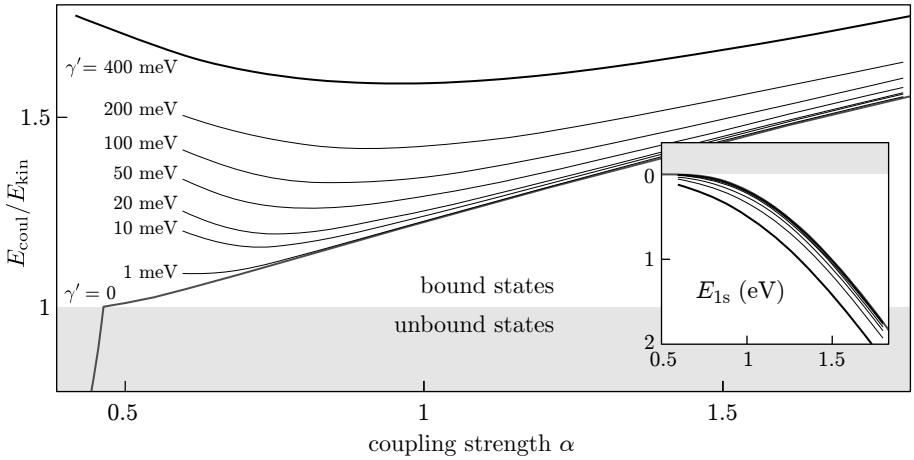

Figure 9.5 Solutions of the Wannier equation (9.12) for a bilayer graphene-like system with a varying interlayer coupling.

The situation can be compared to that in traditional semiconductors, with quadratic bands and a band gap. In those systems, excitonic solutions of the Wannier equation always exist. The exciton binding energy is much smaller than the band gap, though, and the strong-coupling regime would not start until the binding energy is larger than the gap. In bilayer graphene, the bands are also approximately quadratic which would correspond to existence of Wannier exciton solutions, but the band gap being zero means that the existence of those solutions puts the system in the strong-coupling regime.

As a theoretical investigation, we can also study the Wannier equation for a model system where we can vary the coupling between the two layers of graphene. In the dispersion $E_{\boldsymbol{k}}$ (9.5) a weaker interlayer coupling γ' reduces the second term under the square root and the dispersion gradually goes to the linear dispersion of single-layer graphene. The solutions of the Wannier equation for different γ' are shown in figure 9.5. This investigation recovers, as it should, the result for single-layer graphene for $\gamma' = 0$ and the result for bilayer graphene for $\gamma' = 400$ meV.

The solutions for the eigenenergy $E_{1\mathrm{s}}$ for different γ' show a similar behavior as a function of α as the two border cases, $\gamma' = 0$ and $\gamma' = 400$ meV. However, the ratio of Coulomb to kinetic energy numerically obtained in this study shows that all nonzero values of the interlayer coupling γ' makes the system behave qualitatively like the bilayer case; in other words, we see no crossovers to the regime without bound states in any of the cases except for $\gamma' = 0$. Based on

our numerical findings, it appears that for any nonzero interlayer coupling, the system has a bound state solution for all values of α, and is hence always in the strong-coupling regime.

Chapter 10

Solving the screened gap equations

In a realistic model of a material, the strength of the Coulomb interaction between electrons is determined by a phenomenon called screening, where the electric field produced by one electron is attenuated by the cloud of electrons around it. The electron cloud reshapes itself by responding to that electric field, in a way that weakens the effect of the field at larger distances from the electron of origin.

In previous chapters, we have established that when the Coulomb interaction is strong enough, the single-particle, or tight-binding, description of the ground state is no longer sufficient. There is a transition into a strong-coupling state, where the bands are populated in the ground state, or alternatively phrased, there is a new ground state with a band gap in the dispersion. How much population there is in the ground state, depends on the strength of the Coulomb interaction.

The strong-coupling ground state populations, on the other hand, will dramatically influence the screening. At the same time, they are themselves determined by the strength of the Coulomb interaction. For a reasonably realistic estimate for the size of the strong-coupling effects, and ultimately for the band gap, the size of the populations and the strength of the screening should be calculated together, in a way that accounts for the influence they have on each other. Solving the screening self-consistently together with the gap equations, for bilayer graphene specifically, is the topic of Papers V and VI. The interplay of screening and strong Coulomb coupling is also studied for example in [56–58].

10.1 Calculating the screening

In this work, screening, or weakening of the bare Coulomb interaction, has so far been treated only in the form of dielectric screening from the material surrounding the graphene sheet, or the material it is placed on top of. This kind of background dielectric screening is included in the dielectric constant ϵ, which in turn is included in the general Coulomb coupling strength α.

In this chapter, we include screening by calculating how the electron plasma responds to itself. This is done by introducing a polarization function $\Pi(\boldsymbol{q})$ describing the dominant contributions of the response of the plasma to its own Coulomb interaction. The effect can be included in the setup by using a screened Coulomb potential $W^{\mathrm{scr}}(\boldsymbol{q})$. Its relation to the bare potential $W(\boldsymbol{q})$ in terms of the polarization function $\Pi(\boldsymbol{q})$ via the dielectric function $\epsilon(\boldsymbol{q})$, is given by (4.8) and (4.9). For a textbook description, see for example section 12 of [59].

The polarization function can be calculated for a given system with a band structure. In this work, and in Papers V and VI, we follow a procedure similar to the semiconductor derivation in section 8.2 of [4], to calculate the polarization function in graphene. The difference from semiconductors is, once again, that the Coulomb interaction in graphene has more types of terms due to the zero band gap in the tight-binding picture. The main steps in deriving the polarization function are the following; we set up an equation of motion for a so-called density fluctuation $\sum_{\boldsymbol{k}}\langle\hat{a}^\dagger_{\boldsymbol{k}+\boldsymbol{q}}\hat{a}_{\boldsymbol{k}}\rangle$ under an effective Coulomb interaction. The effective Coulomb interaction is taken as the original, unscreened Coulomb interaction times a polarization function $\Pi(\boldsymbol{q})$. The response of the system is given in terms of the polarization function. This yields an expression for the effective Coulomb interaction, and in turn an expression for the polarization function itself.

For practical purposes, in the numerical investigations of this work, the screened Coulomb potential replaces the bare Coulomb potential in all places we have used it so far; in the equations of motion, the Wannier equation, and the gap equations.

10.2 Expressions for the polarization function

In appendix A1 of Paper V, we derive expressions for the polarization function in bilayer graphene. For single layer graphene, the same method can be used, with the appropriate dispersion and matrix elements for the Coulomb interaction. In both these systems, the electronic state is expressed as a solution of the gap equations. The expression for the polarization function is therefore given in

terms of the populations and the rest of the gap equation quantities. This way of calculating the polarization function is commonly referred to as the Lindhard formula [4]. In the following expressions, $\Sigma_{\boldsymbol{k}}$ and $\Omega_{\boldsymbol{k}}$ are the gap equation solutions, $E_{\boldsymbol{k}}^{\mathrm{MF}}$ is the gapped dispersion (7.8) resulting from solving the gap equations in the strong-coupling phase, and $f_{\boldsymbol{k}}$ and $P_{\boldsymbol{k}}$ are the populations. The polarization function for single-layer graphene, in a populated state, is given by

$$\begin{aligned}\Pi(\boldsymbol{q}) = 4\sum_{\boldsymbol{k}} &\big[1+\cos(\theta_{\boldsymbol{k}}-\theta_{\boldsymbol{k}-\boldsymbol{q}})\big]\frac{(\Sigma_{\boldsymbol{k}-\boldsymbol{q}}+\Sigma_{\boldsymbol{k}})(f_{\boldsymbol{k}-\boldsymbol{q}}-f_{\boldsymbol{k}})}{E^2_{\mathrm{MF}\boldsymbol{k}-\boldsymbol{q}}-E^2_{\mathrm{MF}\boldsymbol{k}}}\\ &+\big[1-\cos(\theta_{\boldsymbol{k}}-\theta_{\boldsymbol{k}-\boldsymbol{q}})\big]\frac{(\Sigma_{\boldsymbol{k}-\boldsymbol{q}}-\Sigma_{\boldsymbol{k}})(f_{\boldsymbol{k}-\boldsymbol{q}}+f_{\boldsymbol{k}}-1)}{E^2_{\mathrm{MF}\boldsymbol{k}-\boldsymbol{q}}-E^2_{\mathrm{MF}\boldsymbol{k}}}\\ &-2\frac{(\Omega_{\boldsymbol{k}-\boldsymbol{q}}+\Omega_{\boldsymbol{k}})(P_{\boldsymbol{k}-\boldsymbol{q}}-P_{\boldsymbol{k}})}{E^2_{\mathrm{MF}\boldsymbol{k}-\boldsymbol{q}}-E^2_{\mathrm{MF}\boldsymbol{k}}}\,.\end{aligned} \tag{10.1}$$

For the bilayer case, the polarization function has the form of a two-by-two matrix. The Coulomb strength in either layer is modified, partly by screening in the own layer and partly by screening in the other layer. This can be simplified by an approximation — by treating the graphene sheets as if they were not separated in the z direction. This simplification gives the full screening as a sum over the screening in each sheet;

$$\begin{aligned}\Pi(\boldsymbol{q}) = 4\sum_{\boldsymbol{k}} &\big[1+\cos 2(\theta_{\boldsymbol{k}}-\theta_{\boldsymbol{k}-\boldsymbol{q}})\big]\frac{(\Sigma_{\boldsymbol{k}-\boldsymbol{q}}+\Sigma_{\boldsymbol{k}})(f_{\boldsymbol{k}-\boldsymbol{q}}-f_{\boldsymbol{k}})}{E^2_{\mathrm{MF}\boldsymbol{k}-\boldsymbol{q}}-E^2_{\mathrm{MF}\boldsymbol{k}}}\\ &+\big[1-2\cos(\theta_{\boldsymbol{k}}-\theta_{\boldsymbol{k}-\boldsymbol{q}})\big]\frac{(\Sigma_{\boldsymbol{k}-\boldsymbol{q}}-\Sigma_{\boldsymbol{k}})(f_{\boldsymbol{k}-\boldsymbol{q}}+f_{\boldsymbol{k}}-1)}{E^2_{\mathrm{MF}\boldsymbol{k}-\boldsymbol{q}}-E^2_{\mathrm{MF}\boldsymbol{k}}}\\ &-2\frac{(\Omega_{\boldsymbol{k}-\boldsymbol{q}}+\Omega_{\boldsymbol{k}})(P_{\boldsymbol{k}-\boldsymbol{q}}-P_{\boldsymbol{k}})}{E^2_{\mathrm{MF}\boldsymbol{k}-\boldsymbol{q}}-E^2_{\mathrm{MF}\boldsymbol{k}}}\,.\end{aligned} \tag{10.2}$$

The bilayer expression is in form similar to the single-layer one, apart from factors of two in the geometrical parts, which have their origin in the differences in the Coulomb matrix elements of the two systems.

Although not obvious from the expressions (10.1) and (10.2), a gap in the dispersion will weaken the screening. This is related to the fact that the electrons cannot easily move in the ground state of a system with a band gap, and hence will be less efficient in weakening electric fields. This in turn means that the Coulomb interaction is screened only for smaller distances between the electrons (larger q) and maintains its unscreened strength at larger distances (smaller q).

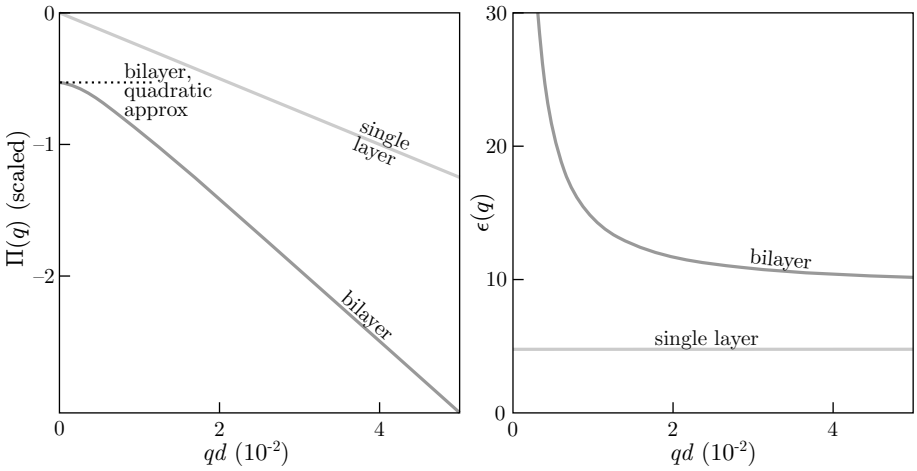

Figure 10.1 The screening in the unpopulated tight-binding ground state in single-layer and bilayer graphene.

10.3 Screening in the tight-binding ground state

When there is no population in the tight-binding bands, the system is in the tight-binding ground state. We obtain the polarization function for the tight-binding ground state by putting $f_{\boldsymbol{k}}$, $P_{\boldsymbol{k}}$ and $\Omega_{\boldsymbol{k}} = 0$, and $\Sigma_{\boldsymbol{k}}$ and $E^{\mathrm{MF}}_{\boldsymbol{k}}$ equal to the tight-binding dispersion $E_{\boldsymbol{k}}$ in the expressions for the polarization function (10.1) and (10.2). In the tight-binding ground state of single-layer graphene, the polarization function (10.1) acquires the form (4.10). For bilayer graphene, the polarization function in the tight-binding ground state is

$$\Pi(\boldsymbol{q}) = -4 \sum_{\boldsymbol{k}} \frac{1 - 2\cos(\theta_{\boldsymbol{k}} - \theta_{\boldsymbol{k}-\boldsymbol{q}})}{E_{\boldsymbol{k}-\boldsymbol{q}} - E_{\boldsymbol{k}}} \,. \tag{10.3}$$

The bilayer polarization function without populations is a constant around $q = 0$, then curves away towards a linear dependence for larger values of q. Screening in the tight-binding ground state in single layer and bilayer graphene (with no populations) is shown in figure 10.1 in the form of the polarization function $\Pi(\boldsymbol{q})$ and the corresponding dielectric function $\epsilon(\boldsymbol{q})$.

In the literature, the dispersion of bilayer graphene is often approximated as a quadratic function of k. With the quadratic approximation for the dispersion, the integration over $\boldsymbol{k}$ in $\Pi(\boldsymbol{q})$ can be performed analytically, with a resulting polarization function that is constant for all q [60]. In figure 10.1, this approximation is shown with a dotted line. As we can see, this is a valid approximation only for small values of q.

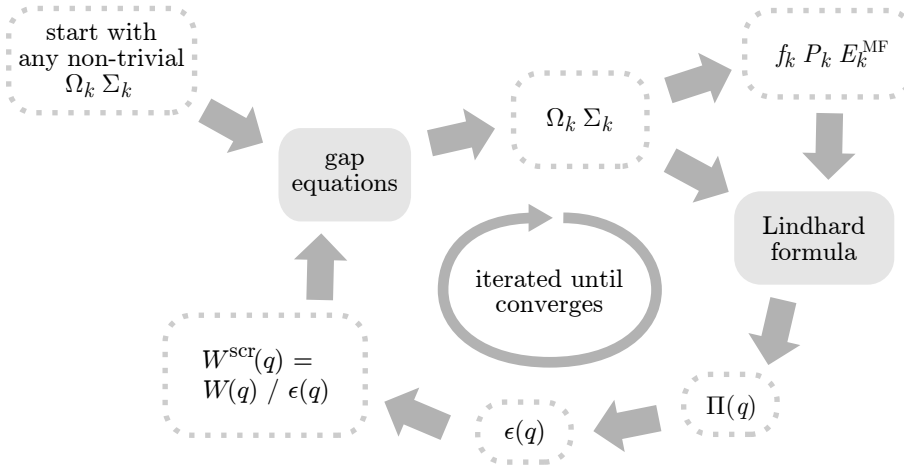

Figure 10.2 Overview of the process of calculating the gap equations and the screening self-consistently.

10.4 Accounting for screening self-consistently

The Coulomb interaction between the electrons is present in the gap equations, giving rise to the strong-coupling effects that are the main reason for solving gap equations. As the Coulomb interaction is influenced by the screening phenomenon, the gap equations are, too. Conversely, the strong-coupling effects arising as a solution the gap equations creates a population of electrons in the tight-binding bands, which in turn affects the screening.

Connecting these two; the gap equations influenced by screening and the screening influenced by the gap equation solutions, we come full circle. The system of equations should be solved self-consistently in order to account for both effects. We provide self-consistency by solving the gap equations and the screening successively, and iterating the steps until both solutions have converged at a stable result. The background-screened gap equations in chapter 7 were solved by iterating candidates for the solution. For the screened gap equations, we include the polarization function (10.1) in the iteration process. The steps and the quantities involved in the iteration are visualized in figure 10.2.

We start in the upper left corner, taking any gap equation quantities $\Sigma_{\boldsymbol{k}}$ and $\Omega_{\boldsymbol{k}}$ with non-trivial values, and insert these in the statically screened gap equations. The gap equations in this setup are iterated, but it is not important to achieve a high accuracy for the convergence at this point, as the overall solution will still influence the gap equation on subsequent rounds of iteration.

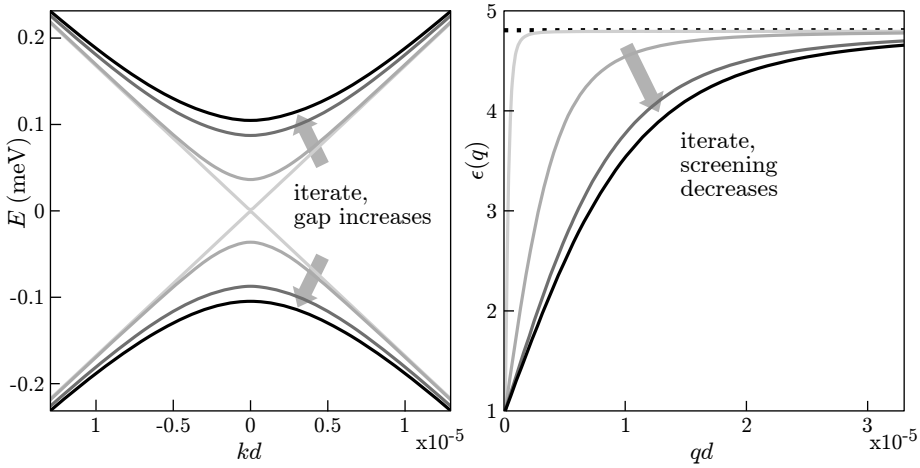

Figure 10.3 Solving the screened gap equations in single layer graphene by iteration.

From the $\Sigma_{\boldsymbol{k}}$ and $\Omega_{\boldsymbol{k}}$ that we get as an intermediate gap equation solution, we calculate a population $f_{\boldsymbol{k}}$ and polarization $P_{\boldsymbol{k}}$. We also calculate a strong-coupling dispersion, $E^{\mathrm{MF}}_{\boldsymbol{k}}$. These $\Sigma_{\boldsymbol{k}}$, $\Omega_{\boldsymbol{k}}$, $f_{\boldsymbol{k}}$, $P_{\boldsymbol{k}}$, and $E^{\mathrm{MF}}_{\boldsymbol{k}}$ are inserted into the Lindhard formula (10.1) to calculate a first approximation for the polarization function $\Pi(\boldsymbol{q})$. The polarization function is used to evaluate an $\epsilon(\boldsymbol{q})$ which is used to modify the Coulomb interaction potential $V(\boldsymbol{q})$. This screened Coulomb interaction is in turn inserted into the gap equations. These can then be solved using the modified Coulomb potential, starting from the previous result for $\Sigma_{\boldsymbol{k}}$ and $\Omega_{\boldsymbol{k}}$.

In this way, the iteration can proceed as many steps as necessary to achieve desired accuracy. For the cases we studied in practice, there were typically a few tens of iterations necessary for convergence. In the figures in the next section, a selection of these iterations are shown. The procedure in this form can be used for both single-layer and bilayer graphene.

10.5 Solving screened gap equations in single layer and bilayer graphene

We solve the self-consistently screened gap equations in single layer graphene, using the procedure described in the previous section; by iterating the gap equations (7.5, 7.4) and the Lindhard formula (10.1) for the screening. At each step of the iteration, we keep track of the strong-coupling dispersion $E^{\mathrm{MF}}_{\boldsymbol{k}}$ as well as

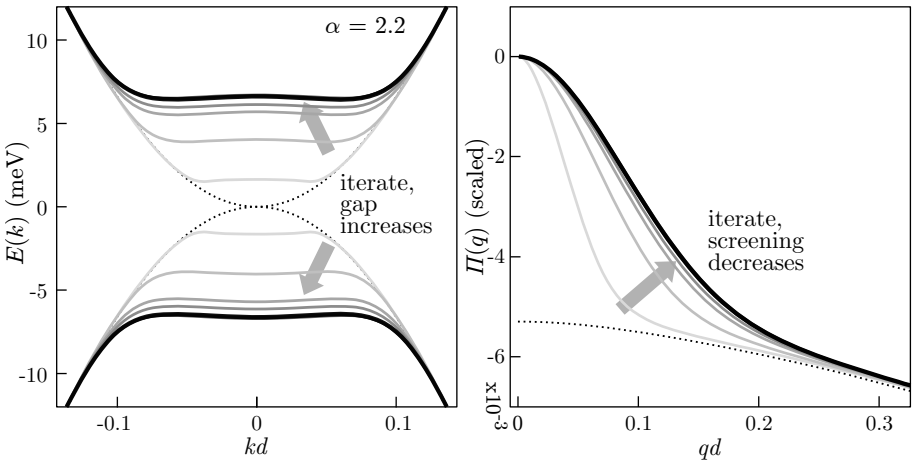

FIGURE 10.4 Solving the screened gap equations in bilayer graphene.

the dielectric function $\epsilon(\boldsymbol{q})$. Results for the dispersion and the dielectric function are shown in figure 10.3.

For the gap equation input, we start from some non-trivial expressions for the gap equation quantities. For the screening, we start from the dielectric function of the tight-binding ground state, shown as a dotted line in the right pane of figure 10.3. The gap equation solution from the initial step is the gapped dispersion shown in a lighter gray. The gapped dispersion leads to the dielectric function going from metal-like to unscreened at $q = 0$. In the next iteration step, this small region of unscreened Coulomb interaction leads to a bigger gap in the strong-coupling dispersion. In turn, this increases the region around $q = 0$ where the dielectric function is small.

The iteration stabilizes after a few tens of steps, after which the functions no longer change in value. As it turns out, however, the iteration process for single-layer graphene stabilizes at a dispersion with a band gap which in experimental terms is negligible, around 0.4 meV. It is also uncertain whether the background coupling strength used, $\alpha = 2.4$, corresponds to a realistic experimental situation. For smaller values of the coupling strength, the resulting values for the band gap would be even smaller. The conclusion we can draw at this point is that, for practical purposes, single-layer graphene is not in a strong-coupling state due to internal screening among the electrons. Hence, the tight-binding description of the ground state is sufficient.

For bilayer graphene, we get more interesting results. Using the same iteration procedure, this time for the bilayer versions of the gap and screening

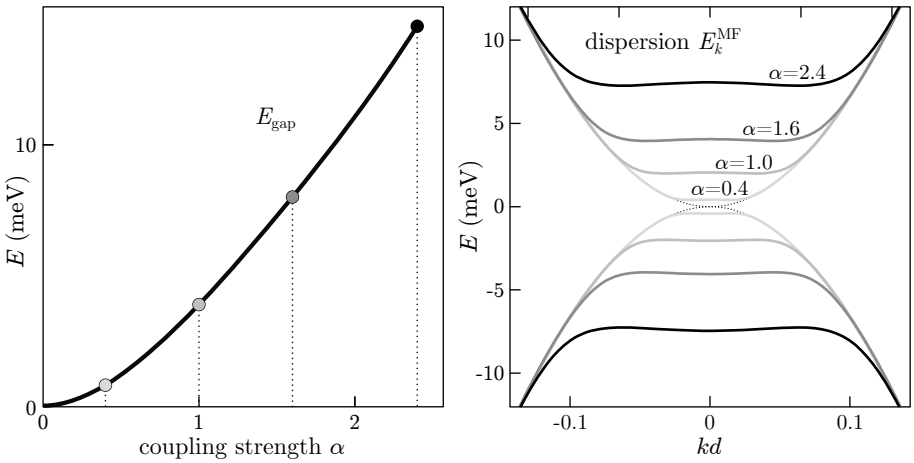

Figure 10.5 Solutions of the self-consistently screened gap equations in bilayer graphene, for different values of the background Coulomb strength α.

equations, gives the iteration steps shown in figure 10.4. In the right pane of figure 10.4, the polarization function $\Pi(\boldsymbol{q})$ is shown instead of the dielectric function.

We observe essentially the same phenomena as in the single-layer case; a band gap reduces the screening, which in turn increases the band gap. Gradually, the two quantities stabilize. For bilayer graphene with a background Coulomb strength $\alpha = 2.4$, we find a band gap of approximately 14 meV, which is large enough to be experimentally observable.

The influence of the background Coulomb strength α is straightforward to calculate with the same numerical setup. The results for the band gap of the resulting dispersion are shown in figure 10.5; the band gap is a smoothly increasing function of α. This shows that Bernal-stacked bilayer graphene is always in a measurable strong-coupling state, to a degree which depends on the dielectric surroundings of the material.

Summary and outlook

In this thesis, we have investigated the possibility of a strong Coulomb coupling state in graphene. This is a state where interaction between active electrons is strong enough to change the electronic ground state. A well-known single-particle description of electrons in the hexagonal lattice gives a linear, cone-like band structure with no band gap, whereas we show that strong interaction effects in a many-body model can open a band gap in the dispersion.

We present a framework for theoretically and numerically studying the electronic and optical properties of graphene, as well as the real-time dynamics of the electronic system through an equations-of-motion approach adapted from semiconductor theory. Also presented is a technique for solving the many-body ground state in the regime of strong Coulomb coupling, as well as the dependence of the resulting strong-coupling ground state on external or internal screening of the Coulomb interaction.

For single-layer graphene our studies show that there most likely is not a strong-coupling ground state; even in vacuum and at zero temperature, due to internal screening among the electrons. For bilayer graphene we find a strong-coupling band gap of around 14 meV in vacuum. This excitonic band gap can be tuned by varying the dielectric environment. The band gap in bilayer graphene is also strongly enhanced in the presence of a bias in the form of an electric field from one layer to the other.

In the studies presented in this thesis, the onset of the strong Coulomb coupling regime initially appears as excitonic solutions of the Wannier equation in graphene in chapter 6; the existence of these solutions sets a limit to the validity of a single-particle picture of the ground state. Going further, the electronic ground state in the strong-coupling regime is solved with so-called gap equations in chapter 7. These equations also provide us with the band structure and the size of the resulting band gap as a function of environmental dielectric properties. Electronic screening can be included in a self-consistent fashion

when solving the ground state, by iterating the gap equations with a generalized Lindhard formula for the screening as is done in chapter 10.

Our methods also provide the opportunity for numerically studying several phenomena familiar from the field of semiconductors, such as calculating the optical spectrum as a frequency dependence of the response of the system to a pulse of light. This is presented for graphene-like systems generally in chapter 3, for graphene in the strong-coupling phase in chapter 8, and for semiconducting carbon nanotubes in chapter 5. Additionally, in chapter 5, the real-space motion of a group of electrons under the evolution of time is simulated. Special cases of graphene-like materials, such as semiconducting carbon nanotubes in chapter 5, and bilayer graphene in chapter 9, can be examined with minor adaptations of the general framework.

Our studies show that the strong Coulomb coupling regime is characterized by a band gap opening up in the dispersion. Apart from being technologically useful in its own right as a switching mechanism, the presence of a band gap gives rise to excitons. The excitonic peaks in the optical spectrum are a convenient way to experimentally determine the presence of the strong-coupling state.

With modifications concerning the geometry of the atomic configuration and adapting hopping parameters, our approach can be applied also to other materials than graphene, such as the new range of two-dimensional crystals with a semiconducting or semimetallic nature. Applying our method would give the possibility to calculate whether the electronic ground state in these new materials is sufficiently characterized by a single-electron picture, and under which circumstances there could instead be a strong-coupling ground state, as well as the effects this would have on the band structure and optical spectrum.

Specifically for transition metal dichalcogenides which are semiconducting and hexagonal, where there are more types of atoms on top of each other in a unit cell, but the arrangement of unit cells is still graphene-like, our method has been used recently for investigating strong Coulomb coupling and the resulting optical spectrum with excitons [61].

Other interesting possibilities for future uses of our methods include two-dimensional systems where the hexagonal lattice is formed by means other than the primary ionic grid, such as twisted bilayer graphene with Moiré pattern hexagons on a significantly larger scale [62, 63] or graphene superlattices formed by growing graphene on other materials [64], as well as a wide range of other artificial two-dimensional hexagonal lattices [65, 66] referred to as graphene analogs or quantum simulators, in which the role of electrons can be played by "optical photons, microwave photons, plasmons, microcavity polaritons or even atoms"

and the hexagonal lattice can be formed by "a photonic crystal, an array of metallic rods, metallic nanoparticles, a lattice of coupled microcavities or an optical lattice" [67].

Svensk resumé

I denna avhandling beskriver jag våra studier av elektroner i materialet grafen, som är ett tvådimensionellt plan av kolatomer. Grafen har blivit enormt populärt inom vetenskap och industri det senaste årtiondet på grund av ett antal uppseendeväckande egenskaper: ett lager grafen är starkt, flexibelt och genomskinligt, och har en mycket hög elektrisk ledningsförmåga.

Våra studier av grafen baserar sig på kvantmekaniska ekvationer för elektronernas rörelse i materialet. Ekvationer av den här typen har tidigare använts i halvledare för att beräkna systemets optiska och elektroniska egenskaper.

Elektroniskt sett är grafen mycket speciellt. Den atomära strukturen kan visas leda till en linjär energirelation; elektronernas energinivåer ligger så att de precis rör varandra i en punkt. Vi studerar under vilka omständigheter växelverkan mellan elektronerna i materialet kunde leda till en förändring i energinivåerna; specifikt, om det är möjligt att växelverkan är så stark att grafen spontant kunde övergå i ett halvledande tillstånd. I ett sådant tillstånd är energinivåerna åskilda av ett bandgap, vilket har dramatiska konsekvenser och skulle vara användbart inom grafenelektronik. Det halvledande tillståndet skulle vara ett s.k. starkt kopplat mångpartikeltillstånd, som påminner om tillståndet i en supraledare.

Vi har utvecklat en metod för att lösa det starkt kopplade tillståndet i grafen med ett ekvationssystem för kvantmekaniska väntevärden. Med hjälp av våra kvantmekaniska metoder kan vi också räkna ut hur elektronerna beter sig i de två olika tillstånden, t.ex. hur det optiska spektret ser ut. Ekvationerna för elektroner i planärt grafen kan också tillämpas för elektroner i andra former av grafen. Jag beskriver också våra undersökningar av elektroner i kolnanorör och i tvålagergrafen. Våra resultat visar att grafen i det starkt kopplade tillståndet skulle ha tydliga excitontoppar i sitt spektrum. Excitontopparna är ett behändigt sätt att experimentellt detektera det starkt kopplade tillståndets eventuella närvaro.

References

[1] K. S. Novoselov, A. K. Geim, S. V. Morozov, D. Jiang, Y. Zhang, S. V. Dubonos, I. V. Grigorieva, and A. A. Firsov, "Electric field effect in atomically thin carbon films," Science **306**, 666 (2004).

[2] K. S. Novoselov, A. K. Geim, S. V. Morozov, D. Jiang, M. I. Katsnelson, I. V. Grigorieva, S. V. Dubonos, and A. A. Firsov, "Two-dimensional gas of massless Dirac fermions in graphene," Nature **438**, 197 (2005).

[3] K. S. Novoselov, A. Mishchenko, A. Carvalho, and A. H. Castro Neto, "2D materials and van der Waals heterostructures," Science **353** (2016).

[4] H. Haug and S. W. Koch, *Quantum theory of the optical and electronic properties of semiconductors* (World Scientific, Singapore, 2009).

[5] D. Jérome, T. M. Rice, and W. Kohn, "Excitonic insulator," Phys. Rev. **158**, 462 (1967).

[6] P. R. Wallace, "The band theory of graphite," Phys. Rev. **71**, 622 (1947).

[7] S. Reich, J. Maultzsch, C. Thomsen, and P. Ordejón, "Tight-binding description of graphene," Phys. Rev. B **66**, 035412 (2002).

[8] A. H. Castro Neto, F. Guinea, N. M. R. Peres, K. S. Novoselov, and A. K. Geim, "The electronic properties of graphene," Rev. Mod. Phys. **81**, 109 (2009).

[9] R. S. Deacon, K.-C. Chuang, R. J. Nicholas, K. S. Novoselov, and A. K. Geim, "Cyclotron resonance study of the electron and hole velocity in graphene monolayers," Phys. Rev. B **76**, 081406 (2007).

[10] J. E. Sipe, personal communication, see footnote 2 of Paper II.

[11] J. C. Straton, "Fourier transform of the multicenter product of 1s hydrogenic orbitals and Coulomb or Yukawa potentials and the analytically reduced form for subsequent integrals that include plane waves," Phys. Rev. A **39**, 5062 (1989).

[12] M. Hirtschulz, F. Milde, E. Malić, S. Butscher, C. Thomsen, S. Reich, and A. Knorr, "Carbon nanotube Bloch equations: A many-body approach to nonlinear and ultrafast optical properties," Phys. Rev. B **77**, 035403 (2008).

[13] M. Hirtschulz, Ph.D. thesis, Technische Universität Berlin (2009).

[14] T. Stroucken, A. Knorr, P. Thomas, and S. W. Koch, "Coherent dynamics of radiatively coupled quantum-well excitons," Phys. Rev. B **53**, 2026 (1996).

[15] A. Grüneis, R. Saito, G. G. Samsonidze, T. Kimura, M. A. Pimenta, A. Jorio, A. G. Souza Filho, G. Dresselhaus, and M. S. Dresselhaus, "Inhomogeneous optical absorption around the K point in graphite and carbon nanotubes," Phys. Rev. B **67**, 165402 (2003).

[16] M. Lindberg and S. W. Koch, "Effective Bloch equations for semiconductors," Phys. Rev. B **38**, 3342 (1988).

[17] E. Malić, T. Winzer, E. Bobkin, and A. Knorr, "Microscopic theory of absorption and ultrafast many-particle kinetics in graphene," Phys. Rev. B **84**, 205406 (2011).

[18] M. Kira and S. W. Koch, "Many-body correlations and excitonic effects in semiconductor spectroscopy," Progress in Quantum Electronics **30**, 155 (2006).

[19] D. A. Siegel, C.-H. Park, C. Hwang, J. Deslippe, A. V. Fedorov, S. G. Louie, and A. Lanzara, "Many-body interactions in quasi-freestanding graphene," **108**, 11365 (2011).

[20] Y. Barlas, T. Pereg-Barnea, M. Polini, R. Asgari, and A. H. MacDonald, "Chirality and correlations in graphene," Phys. Rev. Lett. **98**, 236601 (2007).

[21] O. Vafek and M. J. Case, "Renormalization group approach to two-dimensional Coulomb interacting Dirac fermions with random gauge potential," Phys. Rev. B **77**, 033410 (2008).

[22] D. C. Elias, R. V. Gorbachev, A. S. Mayorov, S. V. Morozov, A. A. Zhukov, P. Blake, L. A. Ponomarenko, I. V. Grigorieva, K. S. Novoselov, F. Guinea, et al., "Dirac cones reshaped by interaction effects in suspended graphene," Nat. Phys. **7**, 701 (2011).

[23] M. A. H. Vozmediano, "Graphene: The running of the constants," Nat. Phys. **7**, 671 (2011).

[24] J. González, F. Guinea, and M. A. H. Vozmediano, "Marginal-Fermi-liquid behavior from two-dimensional Coulomb interaction," Phys. Rev. B **59**, R2474 (1999).

[25] V. N. Kotov, B. Uchoa, V. M. Pereira, F. Guinea, and A. H. Castro Neto, "Electron-electron interactions in graphene: Current status and perspectives," Rev. Mod. Phys. **84**, 1067 (2012).

[26] T. Ando, "Screening effect and impurity scattering in monolayer graphene," J. Phys. Soc. Jpn. **75**, 074716 (2006).

[27] T. O. Wehling, E. Şaşıoğlu, C. Friedrich, A. I. Lichtenstein, M. I. Katsnelson, and S. Blügel, "Strength of effective Coulomb interactions in graphene and graphite," Phys. Rev. Lett. **106**, 236805 (2011).

[28] T. Stauber, "Analytical expressions for the polarizability of the honeycomb lattice," Phys. Rev. B **82**, 201404 (2010).

[29] A. L. Walter, A. Bostwick, K.-J. Jeon, F. Speck, M. Ostler, T. Seyller, L. Moreschini, Y. J. Chang, M. Polini, R. Asgari, et al., "Effective screening and the plasmaron bands in graphene," Phys. Rev. B **84**, 085410 (2011).

[30] J. P. Reed, B. Uchoa, Y. I. Joe, Y. Gan, D. Casa, E. Fradkin, and P. Abbamonte, "The effective fine-structure constant of freestanding graphene measured in graphite," Science **330**, 805 (2010).

[31] E. H. Hwang and S. Das Sarma, "Dielectric function, screening, and plasmons in two-dimensional graphene," Phys. Rev. B **75**, 205418 (2007).

[32] F. Steininger, A. Knorr, T. Stroucken, P. Thomas, and S. W. Koch, "Dynamic evolution of spatiotemporally localized electronic wave packets in semiconductor quantum wells," Phys. Rev. Lett. **77**, 550 (1996).

[33] F. Steininger, A. Knorr, P. Thomas, and S. W. Koch, "The influence of electron-phonon scattering on the spatio-temporal dynamics of electronic wavepackets in semiconductor quantum wells," Zeitschrift für Physik B Condensed Matter **103**, 45 (1997).

[34] V. M. Pereira, J. Nilsson, and A. H. Castro Neto, "Coulomb impurity problem in graphene," Phys. Rev. Lett. **99**, 166802 (2007).

[35] J. Wang, H. A. Fertig, and G. Murthy, "Critical behavior in graphene with Coulomb interactions," Phys. Rev. Lett. **104**, 186401 (2010).

[36] J. Wang, H. A. Fertig, G. Murthy, and L. Brey, "Excitonic effects in two-dimensional massless Dirac fermions," Phys. Rev. B **83**, 035404 (2011).

[37] A. V. Shytov, M. I. Katsnelson, and L. S. Levitov, "Atomic collapse and quasi-Rydberg states in graphene," Phys. Rev. Lett. **99**, 246802 (2007).

[38] J. Sabio, F. Sols, and F. Guinea, "Two-body problem in graphene," Phys. Rev. B **81**, 045428 (2010).

[39] D. E. Sheehy and J. Schmalian, "Quantum critical scaling in graphene," Phys. Rev. Lett. **99**, 226803 (2007).

[40] S. Hands and C. Strouthos, "Quantum critical behavior in a graphenelike model," Phys. Rev. B **78**, 165423 (2008).

[41] I. F. Herbut, V. Juričić, and O. Vafek, "Relativistic Mott criticality in graphene," Phys. Rev. B **80**, 075432 (2009).

[42] O. V. Gamayun, E. V. Gorbar, and V. P. Gusynin, "Supercritical Coulomb center and excitonic instability in graphene," Phys. Rev. B **80**, 165429 (2009).

[43] J. González, "Renormalization group approach to chiral symmetry breaking in graphene," Phys. Rev. B **82**, 155404 (2010).

[44] J. Bardeen, L. N. Cooper, and J. R. Schrieffer, "Theory of superconductivity," Phys. Rev. **108**, 1175 (1957).

[45] J. Bardeen, L. N. Cooper, and J. R. Schrieffer, "Microscopic theory of superconductivity," Phys. Rev. **106**, 162 (1957).

[46] K. S. Novoselov, "Graphene: Mind the gap," Nat. Mater. **6**, 720 (2007).

[47] A. H. Castro Neto, "Pauling's dreams for graphene," Physics **2**, 30 (2009).

[48] G. W. Semenoff, "Chiral symmetry breaking in graphene," Physica Scripta **2012**, 014016 (2012).

[49] O. V. Gamayun, E. V. Gorbar, and V. P. Gusynin, "Gap generation and semimetal–insulator phase transition in graphene," Phys. Rev. B **81**, 075429 (2010).

[50] J. Sabio, F. Sols, and F. Guinea, "Variational approach to the excitonic phase transition in graphene," Phys. Rev. B **82**, 121413 (2010).

[51] W. Armour, S. Hands, and C. Strouthos, "Monte Carlo simulation of the semimetal-insulator phase transition in monolayer graphene," Phys. Rev. B **81**, 125105 (2010).

[52] J.-R. Wang and G.-Z. Liu, "Eliashberg theory of excitonic insulating transition in graphene," J. Phys.: Condens. Matter **23**, 155602 (2011).

[53] J. Nilsson, A. H. Castro Neto, F. Guinea, and N. M. R. Peres, "Electronic properties of bilayer and multilayer graphene," Phys. Rev. B **78**, 045405 (2008).

[54] E. McCann, D. S. Abergel, and V. I. Fal'ko, "Electrons in bilayer graphene," Solid State Communications **143**, 110 (2007).

[55] A. S. Mayorov, D. C. Elias, M. Mucha-Kruczynski, R. V. Gorbachev, T. Tudorovskiy, A. Zhukov, S. V. Morozov, M. I. Katsnelson, A. K. Geim, and K. S. Novoselov, "Interaction-driven spectrum reconstruction in bilayer graphene," Science **333**, 860 (2011).

[56] M. M. Fogler, D. S. Novikov, and B. I. Shklovskii, "Screening of a hypercritical charge in graphene," Phys. Rev. B **76**, 233402 (2007).

[57] A. V. Shytov, M. I. Katsnelson, and L. S. Levitov, "Vacuum polarization and screening of supercritical impurities in graphene," Phys. Rev. Lett. **99**, 236801 (2007).

[58] J. González, "Electron self-energy effects on chiral symmetry breaking in graphene," Phys. Rev. B **85**, 085420 (2012).

[59] A. L. Fetter and J. D. Walecka, *Quantum theory of many-particle systems* (McGraw-Hill, New York, 1971).

[60] E. H. Hwang and S. Das Sarma, "Screening, Kohn anomaly, Friedel oscillation, and RKKY interaction in bilayer graphene," Phys. Rev. Lett. **101**, 156802 (2008).

[61] T. Stroucken and S. W. Koch, "Optically bright p-excitons indicating strong Coulomb coupling in transition-metal dichalcogenides," Journal of Physics: Condensed Matter **27**, 345003 (2015).

[62] Y. Cao, V. Fatemi, A. Demir, S. Fang, S. L. Tomarken, J. Y. Luo, J. D. Sanchez-Yamagishi, K. Watanabe, T. Taniguchi, E. Kaxiras, et al., "Correlated insulator behaviour at half-filling in magic-angle graphene superlattices," Nature **556**, 80 (2018).

[63] Y. Cao, V. Fatemi, S. Fang, K. Watanabe, T. Taniguchi, E. Kaxiras, and P. Jarillo-Herrero, "Unconventional superconductivity in magic-angle graphene superlattices," Nature **556**, 43 (2018).

[64] F. Guinea and T. Low, "Band structure and gaps of triangular graphene superlattices," Phil. Trans. R. Soc. A **368**, 5391 (2010).

[65] M. Polini, F. Guinea, M. Lewenstein, H. C. Manoharan, and V. Pellegrini, "Artificial honeycomb lattices for electrons, atoms and photons," Nature Nanotechnology **8**, 625 (2013).

[66] B. H. Nguyen and V. H. Nguyen, "Two-dimensional hexagonal semiconductors beyond graphene," Advances in Natural Sciences: Nanoscience and Nanotechnology **7**, 043001 (2016).

[67] Wikipedia contributors, "Graphene — Wikipedia, the free encyclopedia,", `https://en.wikipedia.org/w/index.php?title=Graphene&oldid=843563050` (2018), [Online; accessed 30-May-2018].